# Molecular, cellular, and functional aspects of gravity sensing and gravity-oriented tip growth

**Dissertation**

zur

Erlangung des Doktorgrades (Dr. rer. nat.)

der

Mathematisch-Naturwissenschaftlichen Fakultät

der

Rheinischen Friedrich-Wilhelms-Universität Bonn

vorgelegt von

Christoph Limbach

aus

Bonn

Bonn 2006

Angefertigt mit Genehmigung der Mathematisch-Naturwissenschaftlichen Fakultät der Rheinischen Friedrich-Wilhelms-Universität Bonn

1. Referent: Priv.-Doz. Dr. Markus Braun
2. Referent: Prof. Dr. Dieter Volkmann

Tag der Promotion: 22.02.2006

Diese Dissertation ist auf dem Hochschulschriftenserver der ULB Bonn
http://hss.ulb.uni-bonn.de/diss_online elektronisch publiziert.

Erscheinungsjahr: 2006

# Table of Contents

# List of figures

# List of tables

# Abbreviations

| | |
|---|---|
| aa | amino acid |
| acc. no. | gene bank accession number |
| ADF | actin-depolymerizing factor |
| AGP | arabinogalactan-proteoglycan |
| BCECF-AM | 2',7'-bis-(2-carboxyethyl)-5-(and-6)-carboxyfluorescein acetoxymethyl ester |
| BLAST | basic local alignment search tool |
| bp | base pair |
| BSA | bovine serum albumin |
| CCM | *Chara corallina* class XI myosin |
| CCV | clathrin-coated vesicle |
| COP | coat protein |
| CV | coated vesicle |
| CW | cell wall |
| d | day |
| DLR | Deutsches Zentrum für Luft- und Raumfahrt |
| DNA | desoxyribonucleic acid (cDNA = copy …) |
| dNTP | desoxyribonucleoside triphosphate |
| e.g. | example given |
| EGTA | ethylenglycol-bis-(β-amino-ethyl ether)-N,N,N`,N`,-tetraacetic acid) |
| ER | endoplasmic reticulum |
| ESA | European Space Agency |
| Fig. | figure |
| FM 1-43 | N-(3-triethylammoniumpropyl)-4-(4-(dibutylamino)styryl) pyridinium dibromide |
| FM 4-64 | N-(3-triethylammoniumpropyl)-4-(6-(4-(diethylamino)phenyl)hexatrienyl) pyridinium dibromide |
| *g* | gravitational acceleration, 9.81 m $s^{-2}$ (μ*g* = microgravity) |
| GA | glutaraldehyde |
| i.e. | id est |
| IPTG | isopropyl-β-D-thiogalactopyranoside |
| IUB | International Union of Biochemistry |

| | |
|---|---|
| kb | kilobases |
| LB medium | Louria Bertani medium |
| $lN_2$ | liquid nitrogen |
| MAXUS | enlarged version of TEXUS |
| MT | microtubule |
| MV | microvesicle |
| nt | nucleotide |
| PBS | phosphate-buffered saline |
| PCR | polymerase chain reaction |
| PM | plasma membrane |
| RACE | rapid amplification of cDNA ends |
| RNA | ribonucleic acid (mRNA = messenger …) |
| rpm | rounds per minute |
| RT | room temperature |
| SV | secretory vesicle |
| TA | tannic acid |
| TEXUS | technological experiments under reduced gravity |
| TRIS | Tris-(hydroxymethyl)-aminoethan |
| u | unit |
| UA | uranyl acetate |
| UV | ultraviolett |
| X-Gal | 5-bromo-4-chloro-3-indoyl-β-D-galactopyranoside |

# 1 INTRODUCTION

Gravity is one of the most important environmental stimuli that plants use to cope with their environment in a most beneficial way and to optimize exploitation of resources. Gravity always acts constantly at any place on the earth and thereby provides the most reliable external factor for the orientation of the growth direction of plant organs or single cells. The adjustment of the growth orientation relative to the direction of gravity is referred to as gravitropism. This mechanism is essential for all plants because it ensures that roots grow into the soil to take up water and nutrients and to anchor the plant, and that shoots grow towards the light to produce energy-rich metabolites via photosynthesis. Gravitropism is ideally suited for studying the fundamental principles of cellular signaling involved in the perception of environmental stimuli, and in its specific responses. Gravitropic signaling in higher plant organs is very complex (for reviews see Kiss 2000; Boonsirichai et al. 2002; Sievers et al. 2002; Blancaflor and Masson 2003; Morita and Tasaka 2004) because the processes of gravity sensing and of gravitropic responses are accomplished within specific tissues that are locally separated by considerable distances. In addition, the gravity-sensing cells, so-called statocytes, are part of compact tissues and therefore barely accessible for experimental applications investigating the decisive early steps of gravity sensing.

The green alga Chara provides two well established model cell types – rhizoids and protonemata – which are increasingly used to study specific aspects of gravitropism (for reviews see Sievers et al. 1996; Braun 1997; Braun and Limbach 2005a). Interestingly, although rhizoids and protonemata are very similar from the morphological point of view, they exhibit opposite gravitropic growth orientations. Positively gravitropic (downward growing) rhizoids have a root-like function and anchor the algal thallus in the sediment. Negatively gravitropic (upward growing) protonemata are produced by nodal cells in the absence of light, e.g. when the thallus is accidentally buried in the sediment (Hodick 1993). As soon as the cells have penetrated the substrate and reached the light, tip growth terminates, and a complex series of cell divisions is initiated that leads to the regeneration of the green thallus (Braun and Wasteneys 1998a).

Since gravitropic signaling pathways in rhizoids and protonemata are short and cells are easily accessible for experimental approaches, rhizoids and protonemata are particularly well suited to investigate the early processes of gravity sensing which are closely linked to the sedimentation of internal particles, so-called statoliths. Previous studies using rhizoids and

protonemata have contributed greatly to the understanding of the cellular mechanisms of gravitropism in plants (Sievers et al. 1979, 1991a; Hejnowicz and Sievers 1981; Volkmann et al. 1991; Braun and Sievers 1993; Buchen et al. 1993; Hodick 1994; Leitz et al. 1995; Braun 1996a; Cai et al. 1997; Hodick and Sievers 1998; Braun and Richter 1999; Braun 2002; Braun et al. 2002; Limbach et al. 2005). Furthermore, the clarification of the cytoskeleton-dependent processes underlying gravity-oriented tip growth of rhizoids and protonemata (Braun and Sievers 1994; Braun 1996b, 2001; Braun and Wasteneys 1998a, 1998b; Braun et al. 2004) has enhanced the knowledge of principles involved in the establishment of cytoplasmic polarity and in the regulation of polarized growth in plant cells.

## 1.1 Characean rhizoids and protonemata as model systems for studying tip growth

Characean rhizoids and protonemata are tube-like cells with diameters of 30 µm which grow out from the nodes of the green thallus. As a common feature of tip-growing plant cells, e.g. root hairs, pollen tubes, and moss protonemata (Geitmann and Emons 2000; Hepler et al. 2001), the characean cells are characterized by the strong polarity of cytoplasmic organization (Braun 1997; Braun and Wasteneys 1998b). In the basal region, rotational cytoplasmic streaming mediated by two populations of thick actin bundles with opposite polarities is observed to surround the large central vacuole. The nucleus is located at the distal end of the vacuole at the transition to the subapical cell region which extends over a distance of about 300 µm towards the cell apex and contains the majority of cytoplasm and cell organelles, e.g. endoplasmic reticulum (ER), Golgi stacks, mitochondria, plastids, and ribosomes. The cytoplasm of the subapical region is rather static, and no cytoplasmic streaming is observed. The apical region contains the sedimentable, barium-sulfate filled statoliths (Schröter et al. 1975; Wang-Cahill and Kiss 1995) which are densely packed in rhizoids but are more loosely arranged in protonemata (Braun 1997) and accomodates the tip-growth machinery.

As in other tip-growing cell types (Geitmann and Emons 2000; Hepler et al. 2001) growth in rhizoids and protonemata is restricted to the cell apex, and is mediated by the localized exocytosis of secretory vesicles delivering cell wall and membrane material. It is, however, a unique feature of the characean cells that growth mechanisms are coordinated by a prominent Spitzenkoerper complex consisting of an aggregation of ER cisternae and a dense accumulation of vesicles (Bartnik and Sievers 1988; Bartnik et al. 1990). The ER aggregate

contributes to the guidance of secretory vesicles (Bartnik et al. 1990) that are transported towards the tip by myosins interacting with actin microfilaments (Braun 1996a). The position of the Spitzenkoerper defines the center of growth, i.e. the plasma membrane area where the exocytosis rate of vesicles is maximal (Hejnowicz et al. 1977; Sievers et al. 1979; Braun 1996b). An endocytotic mechanism for the recycling of excess membrane material that is delivered to the tip by secretory vesicles is strongly postulated but has so far not been demonstrated.

Microtubules coordinate the polar cytoplasmic organization of rhizoids and protonemata but are absent from the apical region and not directly involved in the cellular mechanisms of growth (Braun and Sievers 1994; Braun and Wasteneys 1998b). In contrast, the actin cytoarchitecture in the apical cell region, which is characterized by a network of fine microfilament bundles that focus in a spherical actin patch in the center of the Spitzenkoerper (Braun and Wasteneys 1998b), plays a crucial role in the organization and regulation of tip growth by mediating vesicle transport and maintaining the structural integrity of the Spitzenkoerper (Braun and Limbach 2005b). A steep tip-high gradient of cytoplasmic free calcium not only dictates the incorporation pattern of secretory vesicles but also spatiotemporally controls the activity of actin-binding proteins (Braun and Richter 1999; Braun et al. 2004) which regulate the various functions and the dynamic nature of the actin cytoskeleton. Spectrin-like epitopes, actin-depolymerizing factor (ADF) and profilin have been shown to accumulate specifically in the center of the Spitzenkoerper (Braun et al. 2004). Spectrin-like proteins most likely participate in the structural integrity of the ER aggregate by forming crosslinks between ER membranes and actin microfilaments (Braun 2001). Furthermore, these proteins may help to create the particular physiological conditions for the mechanisms of tip growth by recruiting specific subsets of membrane proteins and by establishing functional microdomains. The accumulation of the actin-binding proteins ADF and profilin in the center of the Spitzenkoerper indicates high actin turnover rates and an actin-organizing function of this central area (Braun et al. 2004). This conclusion was confirmed by cytochalasin D-induced disruption of the actin cytoskeleton, which causes a complete dissociation of the structural organization of the Spitzenkoerper. After removal of the inhibitor, the reorganization of the actin cytoskeleton starts with the reappearance of a dense actin array in the outermost cell tip (Braun et al. 2004) and is followed by the reorganization of the Spitzenkoerper structure and resumption of tip growth.

These studies provide strong evidence that the complexly coordinated actin architecture in the rapidly extending tip of characean rhizoids and protonemata is functionally related to the fundamental role of the actomyosin system in the regulation of tip growth. The central area of the Spitzenkoerper fulfills the function of a unique apical polymerization site of actin microfilaments (Braun et al. 2004) that has not been found in any other tip-growing cell type (Geitmann and Emons 2000; Hepler et al. 2001; Lovy-Wheeler et al. 2005). In order to clarify the cellular mechanisms mediating tip growth it will be essential to specify the interplay between actin cytoskeleton, ER aggregate, and vesicle trafficking in the apical cytoplasm. A part of the present study aimed at unraveling ultrastructural features of the tip growth machinery and analyzing the distribution of vesicles at high spatial resolution provided by electron tomography.

## 1.2 Rhizoids and protonemata as model systems for research on gravitropism

When studying gravitropism of plant organs or single cells, different phases can be differentiated (Braun and Limbach 2005c): gravity susception describes the initial physical stimulus inside of gravity-sensing cells and is usually mediated by the gravity-oriented sedimentation of statoliths. By activating receptor molecules, statolith sedimentation elicits the gravitropic signaling pathway (gravity perception). In higher plants but not in gravitropic single cells, the physiological signal reflecting the orientation of the organ relative to the direction of gravity is transmitted from the gravity-sensing tissue to the effector cells. The adjustment of the growth orientation according to the direction of gravity (gravitropic response) is mediated by differential growth of organ or cell flanks.

Knowledge about hormone-dependent gravitropic responses in higher plants is rapidly increasing (Blancaflor 2002; Ottenschläger et al. 2003; Aloni et al. 2004; Blilou et al. 2005), whereas the early mechanisms of gravity sensing, i.e. gravity susception and gravity perception, remain unclear. The lack of well-defined results is due to the complexity of gravitropic signals, deriving from several cells of the gravity-sensing tissue and to the difficulties in accessing the statocytes for studying the statolith-dependent mechanisms of gravity sensing. Thanks to the favorable properties of single-celled characean rhizoids and protonemata for various experimental appplications, the interactions between statoliths and the actin cytoskeleton are well understood in these cell types (Hejnowicz and Sievers 1981;

Sievers et al. 1989, 1991a; Volkmann et al. 1991; Buchen et al. 1993; Cai et al. 1997; Hoson et al. 1997; Hodick and Sievers 1998; Braun 2002; Braun et al. 2002; Limbach et al. 2005).

In tip-downward growing rhizoids, statoliths are kept in an area 10 – 35 µm basal to the tip by net-basipetally acting actomyosin forces that prevent statoliths from settling into the tip. In tip-upward growing protonemata, actomyosin prevents statoliths from sedimenting towards the cell base by acting net-acropetally (Hodick et al. 1998; Braun et al. 2002). Inhibitor studies have shown that disrupting the actin cytoskeleton in rhizoids and in protonemata caused statoliths to fall into the tip or towards the nucleus, respectively, following the direction of gravity (Hejnowicz and Sievers 1981; Bartnik and Sievers 1988). Actin disruption resulted in the cessation of growth and in the dislocation of statoliths from their normal resting position which entailed a loss of graviresponsiveness (Braun 2002). After removing the drug, graviresponsiveness was quickly reestablished by the repositioning of statoliths, and tip growth resumed.

Detailed analysis of statolith movements after experimental displacement and under microgravity conditions revealed the surprising complexity of the actomyosin-based transport system that controls statolith positioning (Braun 2002). In the cell regions basal and apical to the statolith region, the vectorial component of the actomyosin transport system pointing towards the statolith region is always the strongest (Sievers et al. 1991a; Braun and Sievers 1993; Braun 2002), which ensures that statoliths are kept in or are retransported to their original position. Statolith transport is mediated by the interaction with mainly axially oriented actin microfilaments that exhibit opposite polarities (Braun and Wasteneys 1998b). When the influence of gravity on statolith positioning was abolished during the microgravity phases of parabolic flights of sounding rockets (Buchen et al. 1993) and during rotation on the three-dimensional and on the fast-rotating clinostat (Hoson et al. 1997; Braun et al. 2002), actomyosin forces generated a displacement of statoliths against the former direction of gravity. These observations justify the conclusion that in normal, vertically-oriented rhizoids and protonemata, the statoliths are kept in a dynamically stable equilibrium position by actomyosin forces which exactly compensate the effect of gravity on the statoliths. Changes in the orientation of the cell with respect to the direction of gravity or changing the amount of the acceleration must inevitably result in a displacement of statoliths.

The actomyosin forces regulating the position of statoliths in rhizoids and protonemata have important implications on how fast and where statoliths sediment, thus pointing up the critical role of actin in the process of gravity susception. Upon a change in the cell´s orientation

relative to the gravity vector, sedimenting statoliths are actively directed to distinct graviperception sites of the plasma membrane (Braun and Limbach 2005a). The graviperception sites which represent the gravisensitive membrane areas where the gravireceptor molecules are exclusively localized were precisely determined in rhizoids and protonemata (Braun 2002). In rhizoids, the graviperception site is confined to a belt-like area of the plasma membrane in the statolith region (10 – 35 µm from the tip). When cells are reoriented by 90°, the sedimenting statoliths mainly follow the gravity vector and settle onto the lower flank of the gravisensitive membrane area. However, when cells are rotated in angles different from 90°, statoliths do not simply follow the gravity vector but are actively redirected against gravity and guided to the graviperception site. In protonemata, the graviperception site is confined to the apical plasma membrane area 5 – 10 µm from the tip. Upon gravistimulation, sedimenting statoliths are transported into the apical dome to the site of gravity perception by actomyosin forces (Braun and Limbach 2005a). It has been shown that statoliths have to be fully sedimented on the membranes in order to trigger graviperception in rhizoids and protonemata (Braun 2002). However, until recently it was unclear how gravireceptor molecules are activated by the sedimented statoliths. Therefore, the functional mechanisms of gravireceptor activation were investigated in the present study under microgravity conditions provided by parabolic plane flights.

In order to unravel the fundamental principles underlying the opposite orientation of growth in rhizoids and protonemata the cellular mechanisms of gravitropic responses in these cell types have been studied in great detail (Hodick 1994; Hodick and Sievers 1998; Braun and Richter 1999; Braun 2001). The results provide evidence that differences in the anchorage of the Spitzenkoerper complex play a crucial role. Immunofluorescence and video microscopy using differential interference contrast indicated that the Spitzenkoerper and, as a consequence, also the center of maximal growth is easily displaced in protonemata by intruding statoliths, which naturally occurs upon gravistimulation (Braun 2001). The displacement of the Spitzenkoerper is followed by the appearance of a bulge at the upper cell flank and by an upward shift of cell growth (´bending by bulging´; Hodick 1994; Braun 1996b). In contrast, no bulge is formed during the smooth downward curvature response of rhizoids (´bending by bowing´). Immunofluorescence labeling of spectrin-like proteins in the center of the Spitzenkoerper was drastically displaced towards the upper flank, the site of future outgrowth, during initiation of the graviresponse in protonemata, clearly before curvature was recognizable (Braun 2001). In contrast, the same labeling in rhizoids remained

symmetrically positioned in the apical dome throughout the graviresponse, confirming that a repositioning of the Spitzenkoerper is involved in the negative graviresponse of protonemata, but not in the positive graviresponse of rhizoids. There is evidence from centrifugation experiments (Braun 1996b; Hodick and Sievers 1998) and from attaching particles to the surface of gravitropically responding rhizoids (Sievers et al. 1979) that the position of the growth center at the cell tip is relatively stable and that the Spitzenkoerper is more tightly anchored by cytoskeletal forces in rhizoids than in protonemata. However, rhizoids can be forced to respond to some extent like protonemata when statoliths are asymmetrically pushed into the apical dome by considerable centrifugal forces or laser tweezers displacement (Braun 1996b; Braun 2002).

Calcium imaging experiments (Braun and Richter 1999) demonstrated a drastic shift of the steep tip-high calcium gradient towards the upper flank during initiation of the graviresponse in protonemata, but not in rhizoids. In addition, dihydropyridine-fluorescence reflecting the distribution of calcium channels was found to be displaced towards the upper flank in graviresponding protonemata, but not in rhizoids. An asymmetric influx of calcium at the upper flank of protonemata is suggested to be responsible for the respositioning of the Spitzenkoerper by differentially regulating the activity of actin-associated proteins along the shifting calcium gradient (Braun and Richter 1999).

The characterization of actomyosin-mediated statolith transport and the elucidation of calcium-dependent response mechanisms in characean rhizoids and protonemata have provided considerable progress in the understanding of the cellular processes that are involved in gravitropism. In none of the other gravity-sensing plant cell types interactions between statoliths and the actin cytoskeleton have been described in more detail. There are indications from experiments in microgravity that statoliths interact with actin in higher plant statocytes as well (Volkmann et al. 1991; Driss-Ecole et al. 2000; Perbal et al. 2004). However, consistent evidence for the role of actin in graviperception is absent. Since susception of gravity by sedimentable statoliths is a common feature of gravity sensing in the plant kingdom, the results obtained from characean rhizoids and protonemata have a crucial impact on the elucidation of the early phases of gravitropism in higher plants.

## 1.3 Objectives of the study

Although previous studies have added considerably to the understanding of the polar cytoplasmic organization and of actin-dependent transport processes in characean rhizoids and protonemata, little is known about mechanisms of gene regulation and about molecular interactions of signaling factors being involved in gravity-oriented tip growth. Due to the limitations of conventional electron microscopic analyses it is also still unclear how these dynamic cellular processes can be fit into the strctural organization of the cells. In the present study, innovative experimental approaches providing a significantly improved resolution level of subcellular research were used to gain new insights into molecular, structural, and functional aspects of gravity sensing and gravity-oriented tip growth in characean rhizoids and protonemata.

### 1.3.1 Analysis of gene expression in gravity-sensing cells

By influencing the abundance of signaling molecules, regulation of gene expression plays an important role for all cellular signaling pathways. However, the mechanisms of gene regulation in plant gravitropism have long been elusive, and it was not until recently that analyses of gene expression patterns provided the first genes that are discussed to be involved in gravitropic signaling in higher plants (Kimbrough et al. 2004; Theisen 2005; R. Hampp, Universität Tübingen, Germany, personal communication; K. Palme, Universität Freiburg, Germany, personal communication). Interpretation of the results is complicated by one major drawback of gene expression analyses in higher plant organs: gravistimulation-dependent changes in the transcription level of genes represent cumulative effects deriving from numerous cells of different tissues and cannot be attributed specifically to the cell types mediating the different processes of gravitropism.

It was therefore tempting to investigate in this study the gene expression patterns of single-celled characean rhizoids and protonemata that are not masked by signals from additional cell types. In the characean cells gravistimulation-dependent changes in the transcription level of genes correlate directly with gravity sensing. For working with characean rhizoids and protonemata basic molecular applications were developed and optimized. In order to identify distinct genes that are up- or down-regulated upon gravistimulation and that are therefore

likely to encode proteins being involved in the gravitropic signaling pathway gene expression patterns were analyzed by differential display technology.

### 1.3.2 Characterization of early gravity-sensing mechanisms

The second part of the study focused on the molecular interactions of some well-known cellular components playing a crucial role for gravity susception and gravity perception in characean rhizoids and protonemata, i.e. statoliths, gravireceptor molecules, and the actin cytoskeleton. In higher plants, little is known about the cellular and molecular mechanisms underlying the decisive early steps of gravity sensing (Kiss 2000; Morita and Tasaka 2004). The starch-statolith theory of gravity sensing in higher plants (Němec 1900; Haberlandt 1900) proposing that gravity susception is mediated by sedimentable starch-filled amyloplasts, which function as statoliths inside of gravity-sensing statocytes has been confirmed by numerous studies using various experimental approaches (Juniper et al. 1966; Fukaki et al. 1996, 1998; Kiss et al. 1996; Kuznetsov and Hasenstein 1996, 1997; Blancaflor et al. 1998; Kuznetsov et al. 1999; MacCleery and Kiss 1999; Tsugeki and Fedoroff 1999; Weise and Kiss 1999; Fujihira et al. 2000; Weise et al. 2000). However, hypotheses trying to explain how the vectorial information of a physical displacement of statoliths is perceived by cellular components and transduced into a physiological signal remain controversial. Several reports implied actin microfilaments in the process of gravity sensing, but their role for gravitropic signalling is still unclear since findings are contradictory (Sievers et al. 1991b; Kiss 2000; Blancaflor 2002; Sievers et al. 2002; Hou et al. 2003, 2004).

In this study, cellular and molecular aspects of early gravity sensing mechanisms were investigated in characean rhizoids under microgravity conditions provided by parabolic flights of sounding rockets and the A300 Zero-G aircraft. The minimum acceleration level required to induce lateral displacement of statoliths in vertically growing cells was determined by lateral centrifugation in microgravity during the MAXUS-5 sounding rocket flight. Analysis of the statolith position at the end of the microgravity phase allowed to calculate the forces of molecular interaction between statoliths and the actin cytoskeleton restricting gravity susception.

The acceleration profile of parabolic flights of the A300 Zero-G aircraft with alternating hyper- and microgravity phases provided good conditions to investigate the functional mechanism of gravireceptor activation in characean rhizoids. In order to test if sedimented

statoliths were capable of activating the gravireceptor molecules even when they were weightless, the maximally achieved curvature angles of gravistimulated cells were compared with in-flight controls that experienced identical conditions but were centrifuged at 1*g* (gravitational acceleration) during the short microgravity phases. In combination with comprehensive ground control experiments, the parabolic flight experiments were intended to clarify whether activation of the gravireceptor in rhizoids depends on mechanical forces that are exerted by the weight of sedimented statoliths or on pressure-independent interactions between statoliths and receptor molecules.

### 1.3.3 The structural basis of gravity-oriented tip growth

The above illustrated molecular and functional characterization of gravity-sensing mechanisms in rhizoids and protonemata was complemented by detailed electron microscopic studies which aimed at fitting the keyplayers of gravitropic signaling and gravity-oriented tip growth into the context of the structural cellular organization. Until recently, samples for electron microscopic studies of rhizoids were mainly prepared by chemical fixation. These studies provided a comprehensive description of the polar cytoplasmic organization and of the major cellular compartments (Sievers 1965, 1967a, 1967b; Bartnik 1984; Noecker 2000). However, artifacts caused by chemical fixation and the use of conventional electron microscopy limited the level of ultrastructural resolution.

In this study, samples of characean rhizoids were prepared for electron microscopy by high-pressure freeze fixation/freeze substitution and were analyzed by 3D dual-axis tomography. Cryofixation is well known to improve the preservation of cellular ultrastructure since it ensures the fast and simultaneous fixation of all cellular components and avoids the formation of artifacts that are observed after chemical fixation (Gilkey and Staehelin 1986; Dahl and Staehelin 1989; Kiss et al. 1990; Staehelin et al. 1990; Studer et al. 1992). Electron tomography (Mastronarde 1997) has recently been shown to significantly improve the resolution level of electron microscopic imaging and to provide new insights into ultrastructural details of cellular organization and dynamic processes in a variety of cell types (Ladinsky et al. 1999; Otegui and Staehelin 2000, 2004; Otegui et al. 2001; Seguí-Simarro et al. 2004; Austin et al. 2005; Kürner et al. 2005; Nicastro et al. 2005; Seguí-Simarro and Staehelin 2005). Using these techniques for high-resolution ultrastructural investigations, the present study was intended to determine the different types of vesicles in the Chara rhizoid

and to analyze their distribution in the apical cytoplasm. The results were expected to elucidate mechanisms of vesicle trafficking which have important implications for the understanding of polarized growth in plant cells. In addition, the present work is one of the first studies providing a high-resolution electron microscopic analysis of the cellular ultrastructure in a gravity-sensing cell type since it proved difficult to prepare decent samples of higher plant statocytes.

In previous studies, chemical fixation not only caused artifacts that impaired ultrastructural investigations but also affected the structure of epitopes and, thereby, hampered the specific binding of antibodies in immunogold labeling experiments. Based upon the excellent preservation of protein conformation by cryofixation, a protocol for the preparation of high-pressure frozen rhizoid samples for immuno-electron microscopy was meant to be developed in this study in order to establish a basis for the functional characterization of cellular compartments and for the reliable subcellular localization of the keyplayers of gravity sensing and tip growth.

# 2 MATERIALS AND METHODS

## 2.1 Chemicals and Reagents

All chemicals and reagents used for the experiments presented in this publication were purchased from Sigma (Munich, Germany) or Merck (Darmstadt, Germany) unless otherwise stated.

## 2.2 Antibodies

Primary antibodies:

- Mouse anti-C4 actin, monoclonal, $IgG_1$ (Qbiogene, Heidelberg, Germany); dilution 1:400
- Mouse anti-clathrin heavy chain, monoclonal, $IgG_1$ (BD Biosciences, Heidelberg, Germany); dilution 1:100

Secondary antibody:

- Goat anti-mouse IgG, 10 nm-gold conjugated (Sigma); dilution 1:100

## 2.3 Primer

The nucleotide sequences of all primers used in this study are listed in Table VI in the appendix. Primers were diluted for use from stock solutions (100 µM) with sterile water or nuclease-free water (for RNA-applications) as indicated for each experiment. Gene-specific amplification primers were designed using the Primer3 software (Rozen and Skaletsky 2000) provided by the Whitehead Institute for Biomedical Research (URL: http://frodo.wi.mit.edu/cgi-bin/primer3/primer3_www.cgi).

## 2.4 Solutions and Media

**Modified Forsberg medium** (Braun 1994, modified after Forsberg 1965)

100× stock solution:

| | | |
|---|---|---|
| 0.8 | g $l^{-1}$ | $Ca(NO_3)_2 \times 4\ H_2O$ |
| 1.0 | g $l^{-1}$ | $MgSO_4 \times 7\ H_2O$ |
| 0.2 | g $l^{-1}$ | $Na_2CO_3$ |
| 0.3 | g $l^{-1}$ | KCl |
| 0.4 | g $l^{-1}$ | $K_2HPO_4 \times 3\ H_2O$ |
| 0.2 | g $l^{-1}$ | NTA |
| 5.0 | g $l^{-1}$ | TRIS |
| | pH | 7.2 |

Micronutrient stock solution:

| | | |
|---|---|---|
| 1.0 | g $l^{-1}$ | $ZnCl_2$ |
| 0.02 | g $l^{-1}$ | $MnCl_2 \times 4\ H_2O$ |
| 0.02 | g $l^{-1}$ | $CoCl_2 \times 6\ H_2O$ |
| 0.04 | g $l^{-1}$ | $CuCl_2 \times 2\ H_2O$ |
| 1.0 | g $l^{-1}$ | $Na_2MoO_4 \times 2\ H_2O$ |
| 4.0 | g $l^{-1}$ | $H_3BO_3$ |

EDTA-Fe stock solution:

| | | |
|---|---|---|
| 1.30 | g | EDTA |
| 1.25 | g | $FeSO_4 \times 7\ H_2O$ |
| 13.5 | ml | KOH |

Distilled water was added to a volume of 200 ml and boiled for 30 min. The solution was the filtered and made up to a final volume of 250 ml.

Forsberg medium was prepared for use by mixing 10 ml 100× stock solution, 10 µl micronutrient stock solution and 1 ml EDTA-Fe stock solution and adding distilled water to a final volume of 1 l.

**PBS (phosphate-buffered saline)**

| | | |
|---|---|---|
| 137 | mM | NaCl |
| 2.7 | mM | KCl |
| 4.3 | mM | $Na_2HPO_4$ |
| 1.4 | mM | $KH_2PO_4$ |

For preparing buffers PBS/glycine, PBST and PBS-high Tween, PBS was supplemented with 50 mM glycine, 0.1% Tween 20 and 0.5% Tween 20, respectively.

**LB medium (Louria Bertani medium)**

| | | |
|---|---|---|
| 10 | g $l^{-1}$ | bacto-tryptone |
| 5 | g $l^{-1}$ | bacto-yeast extract |
| 5 | g $l^{-1}$ | NaCl |
| | pH | 7.0 |

The medium was autoclaved and used under sterile conditions.

**LB agar plates**

For preparing LB agar plates, LB medium was supplemented with 15 g $l^{-1}$ bacto-agar, autoclaved and cooled down to ~ 50° C. 25ml of medium was poured into 85 mm-petri dishes, the agar was allowed to harden, and plates were stored at 4° C. LB/amp plates were prepared as above with ampicillin being added to the medium to a final concentration of 100 µg ml $l^{-1}$ before pouring the plates. For preparing LB/amp/IPTG/X-Gal plates which were used for color screening of recombinant clones after transformation of bacteria, 100 µl of 100 mM IPTG (isopropyl-β-D-thiogalactopyranoside) and 20 µl of 50 mg $l^{-1}$ X-Gal (5-bromo-4- chloro-3-indoyl-β-D-galactopyranoside) were dispersed on a LB/amp plate and allowed to absorb for 30 min at room temperature (RT) prior to use.

**Lowicryl HM20**

The embedding resin was purchased from Electron Microscopy Sciences (Fort Washington, USA) and freshly prepared prior to use:

| | | |
|---|---|---|
| 5.96 | g | crosslinker D |
| 34.04 | g | monomer E |
| 0.20 | g | initiator C |

**Reynold´s lead citrate**

| | | |
|---|---|---|
| 2.6 | % | $Pb(NO_3)_2$ |
| 3.5 | % | $C_6H_5Na_3O_7 \times 2\ H_2O$ |
| | pH | 12 |

Distilled water (~ 75 ml) was degassed by boiling for 5 min and cooled to RT. 665 mg of lead nitrate and 880 mg of sodium citrate were dissolved in 15 ml of the water. The solution was mixed thoroughly and sonicated for 30 min with shaking every 5 min until the contents were completely dissolved and the solution was milky. NaOH (1 N in degassed water) was added dropwise until the solution became clear. Degassed water was added to a final volume of 25 ml, and the solution was filtered before use.

**SOC-medium**

| | | |
|---|---|---|
| 20.0 | g $l^{-1}$ | bacto-tryptone |
| 5.0 | g $l^{-1}$ | bacto-yeast extract |
| 10.0 | mM | NaCl |
| 2.5 | mM | KCl |
| 10.0 | mM | $MgCl_2$ |
| 20.0 | mM | $MgSO_4$ |
| 20.0 | mM | glucose |
| | pH | 7.0 |

Bacto-tryptone, bacto-yeast extract, NaCl and KCl were dissolved in 97 ml distilled water. The medium was autoclaved, cooled to RT, and supplemented with 1 ml of 2 M $Mg^{2+}$ stock solution (1 M $MgCl_2 \times 6\ H_2O$, 2 M $MgSO_4 \times 7\ H_2O$; filter sterilized) and 1 ml of 2 M glucose (filter sterilized). Sterile, distilled water was added to a final volume of 100 ml, and the complete medium was filtered through a 0.2 µm filter unit.

**TAE buffer (tris-acetate buffer)**

| | | |
|---|---|---|
| 40 | mM | TRIS |
| 5 | mM | EGTA |
| 20 | mM | acetic acid |
| | pH | 8.0 |

## 2.5 Plant Material

Thallus of *Chara globularis* Thuill. and *Chara contraria* A. Braun ex Kutz. was collected from a pond at the Botanical Garden of the University of Bonn, Germany and from ponds near Coot Lake in Boulder County, Colorado, USA, respectively. For the production of rhizoids, young thalli were cut into segments of at least two nodes and one internodal cell. The side branches of the lower node were cut off to induce rhizoid outgrowth. The segments were placed in upright culture chambers (330 ml) filled with modified Forsberg medium. Alternatively, they were embedded in a thin layer of agar (1.2% in distilled water) either in IML-2 (Second International Microgravity Laboratory Mission) containers or on microscope slides which were covered with long coverslips being fixed with tape. Both types of cuvettes were placed vertically in staining jars filled with ~ 10 ml distilled water. Rhizoids developed in liquid cultures and in agar cultures after 4 to 5 days at RT under continuous illumination at 150 to 200 μmol $m^{-2}$ $s^{-1}$. For the production of protonemata, single nodes were isolated by clipping the internodes and side branches. The segments of the thallus were arranged along the flank of a microscope slide and embedded in agar as described for rhizoids. The microscope slides were placed horizontally in staining jars filled with ~ 20 ml distilled water and protonemata developed within 10 to 20 days in complete darkness at RT.

## 2.6 Fluorescence staining with vital dyes and confocal microscopy

The fluorescence dyes that were used for in-vivo labeling of specific cellular compartments in characean rhizoids are listed in Table 1 with their corresponding absorption and emission maxima and the concentration range used in the experiments. FM styryl-dyes (FM 1-43 and FM 4-64) were applied to visualize endocytotic events at the apical plasma membrane whereas DFFDA and BCECF were used to label vacuolar compartments.

For fluorescence labeling, nodes with rhizoid bundles from liquid cultures were clipped from the thallus and incubated with the dye which was diluted in modified Forsberg medium. For microscopic observation, the samples were incubated in a droplet of either staining solution or fresh medium on a long coverslip which was attached to a Plexiglas frame with a 1:1-mixture of wax and vaseline. When covering rhizoids with a small coverslip, broken fragments of a coverslip served as spacers to avoid squeezing of the samples.

**Table I** *Fluorescence dyes*

| Fluorescence dye | Absorption / emission maximum | Concentration for use |
|---|---|---|
| **FM 1-43** (N-(3-triethylammoniumpropyl)-4-(4-(dibutylamino)styryl) pyridinium dibromide)[a] | 479 / 598 nm | 2 μM |
| **FM 4-64** (N-(3-triethylammoniumpropyl)-4-(6-(4-(diethylamino)phenyl)hexatrienyl) pyridinium dibromide)[a] | 506 / 750 nm | 1 – 2 μM |
| **Carboxy-DFFDA** (Oregon Green 488 caboxylic acid diacetate)[a] | 478 / 518 nm | 10 – 25 μM |
| **BCECF-AM** (2',7'-bis-(2-carboxyethyl)-5-(and-6)-carboxyfluorescein acetoxymethyl ester)[b] | 503 / 528 nm at pH 9 | 0.01 – 5 μg ml-1 |

[a] Purchased from Molecular Probes (Eugene, USA)
[b] Purchased from Sigma

The samples were examined with a TCS4D confocal microscope (Leica, Heidelberg, Germany) using excitation with the 488-nm line (FM 1-43, DFFDA, BCECF) or the 514-nm line (FM 4-64) of the argon/krypton laser. Images were collected with the microscope software at 8 to 32 counts with an image size of 512 × 512 pixels. Z-series and time-series, were taken to study the three-dimensional shape and dynamic properties of the labeled structures or compartments. Projections of serial confocal sections and contrast enhancement were done using image processing software, e.g. Scion Image (Scion Corporation, Frederick, USA) and Adobe Photoshop 7.0 (Adobe Systems, Mountain View, USA).

## 2.7 Molecular biology

### 2.7.1 Standard PCR

Standard PCR (polymerase chain reaction) was performed with the Taq DNA polymerase system purchased from Fermentas (St. Leon-Rot, Germany) and used for random-primed PCR, gene-specific PCR and in-cell PCR with primers indicated for the corresponding application. The PCR reaction was mixed in a 0.2 ml-tube placed on ice.

| | | |
|---|---|---|
| 11.6 | µl | sterile water |
| 2.0 | µl | 10× PCR buffer (Fermentas) |
| 2.0 | µl | 25 mM $MgCl_2$ (Fermentas) |
| 1.4 | µl | forward primer 12 µM |
| 1.4 | µl | reverse primer 12 µM |
| 0.4 | µl | dNTP-mix (10 mM each) |
| 1.0 | µl | template |
| 0.2 | µl | Taq DNA polymerase 5u/µl (Fermentas) |
| 20.0 | µl | |

PCR amplification was performed using a Bio-Rad iCycler (Munich, Germany). For each PCR reaction, the primer annealing temperature and the number of amplification cycles were adjusted according to the calculated melting temperature of the primers and to the DNA-yield. Unless otherwise noted, the following standard cycler program was used for amplification:

| | | | |
|---|---|---|---|
| 5 | min | 95.0° C | |
| 30 | sec | 95.0° C | × 40 |
| 1 | min | 64.8° C | |
| 1 | min | 72.0° C | |
| 10 | min | 72.0° C | |
| | | 4.0° C | |

### 2.7.2 Agarose gel electrophoresis and purification of PCR products

Samples for agarose gel electrophoresis were prepared by mixing the desired amount of amplified DNA with 6× running buffer (Peqlab, Erlangen, Germany) and sterile water to a final volume of at least 10 µl with the final concentration of running buffer being single-fold. DNA-samples were loaded on a 1% agarose gel which was run at 75 – 90 V for 45 – 90 min in 1× TAE-buffer. As size standard an extended 100 bp-DNA ladder (Carl Roth, Karlsruhe, Germany) was used. The gel was stained with ethidium bromide (0.5 µg $ml^{-1}$ in TAE buffer) for 10 to 30 min. For the isolation of PCR products the corresponding bands were excised from the gel under UV (ultraviolett) light, and DNA was purified using the QIAquick Gel Extraction Kit (Qiagen, Hilden, Germany) according to the manufacturer's manual. Alternatively, PCR products were purified from the PCR-reaction mix by using the QIAquick PCR Purification Kit (Qiagen).

### 2.7.3 Competent bacteria

Competent E. coli bacteria were prepared under sterile conditions according to the following protocol:

- inoculate 2.5 ml LB medium with bacteria (E. coli strains DH5α or JM109) from a stock suspension using a sterile tooth pick
- incubate the culture overnight at 37° C with shaking at 150 rpm (rounds per minute)
- dilute 1.5 ml of the culture in 100 ml LB medium and grow at 37° C with shaking (150 rpm) until the optical density ($OD_{600nm}$) is in a range of 0.5
- transfer the culture to centrifugation tubes and centrifuge at 4000 rpm for 15 min at 4° C
- discard the supernatant, resuspend each bacterial pellet in 2 ml 0.1 M $CaCl_2$ and incubate for 5 min on ice
- centrifuge at 4000 rpm for 15 min at 4° C
- discard the supernatant, resuspend each pellet in 2 ml 0.1 M $CaCl_2$ + 10% glycerol
- transfer aliquots of 200 µl to 1.5 ml-tubes, freeze in liquid nitrogen and store at –80° C

### 2.7.4 Differential display

The differential display-technology (Liang and Pardee 1992) is one method among others to compare gene expression patterns in two or more samples that experienced different conditions. mRNA is extracted from cells or tissues of the samples and reversely transcribed into cDNA strands by using an oligo dT-anchor primer binding to the polyA$^+$-tail of the mRNA transcripts. Random fragments of the 3'RNA-ends are amplified by random-primed PCR and detected by electrophoresis. Fragment patterns and intensities of the products which are specific for each of the different samples are compared and those fragments representing genes with differential expression are cloned and sequenced. To identify the corresponding gene, the complete coding region is determined by 5'RACE-PCR (rapid amplification of cDNA ends). In the present study, gene expression was compared between gravistimulated and unstimulated characean rhizoids and between rhizoids and protonemata according to a protocol modified after Theisen (2005) using capillary electrophoresis for fragment analysis. In addition, some of the gene transcripts exhibiting high expression levels but no differential expression were sequenced and characterized in order to increase the amount of gene sequences of characean algae.

#### 2.7.4.1 RNA extraction

Total mRNA was isolated from agar-embedded rhizoids of *Chara globularis* that were either unstimulated or gravistimulated by 90° for 20 or 45. Nodes with bundles of rhizoids were cut off from the thallus, pulled out of the agar and immediately frozen in liquid nitrogen. Frozen rhizoids and protonemata were clipped from the node with prechilled scissors into a reaction tube filled with 400 µl lysis buffer of the RNA-extraction kit (see below). Rhizoid bundles of 50 nodes were collected per tube.

Alternatively, the cytoplasm of gravistimulated or unstimulated rhizoids and protonemata of *C. globularis* was extracted by single-cell aspiration with microcapillaries. Agar-embedded samples were transferred to the microscope stage of an inverted microscope (Leica) that was equipped with two microcapillary holders mounted on micromanipulators. Extraction capillaries were prepared with a PC-10 puller (Narishige, Tokyo, Japan) in a two-step mode (step 1: 81.5, step 2: 45.8) using borosilicate capillaries with filament (outer diameter 1.5 mm, inner diameter 0.75 mm; Hilgenberg, Malsfeld, Germany). Before use, the tips of these capillaries were broken by carefully tapping onto a sterile petri dish in order to obtain sharp

edges. The extraction capillary was mounted on a holder that was connected to a 50 ml-syringe and loaded with lysis buffer (devoid of β-mercaptoethanol) by submerging the tip in a droplet of the buffer. Holding capillaries were prepared by pulling borosilicate capillaries (outer diameter 1.0 mm, inner diameter 0.7 mm; Hilgenberg) in a one-step mode (step 1: 55.1). The capillary tip was carefully broken on a petri dish and polished with a MF-90 microforge (Narishige). The holding capillary was mounted on the second microcapillary holder and, under microscopic control, attached to the lateral subapical flank of a rhizoid or protonema. The extraction capillary was inserted into the cell at the opposite flank, and turgor pressure forced the cytoplasm to flow into the extraction capillary where it mixed with the lysis buffer. Aspiration of the cytoplasm could be supported by applying a vacuum with the syringe connected to the extraction capillary. The capillary was quickly removed from the agar, the tip was broken inside a reaction tube filled with 400µl lysis buffer (with β-mercaptoethanol), and the contents of the extraction capillary were released by compressing the syringe. The cytoplasm of several cells was collected in each tube with the number of extracted cells being identical in those samples that were compared by differential display analysis. During cell aspiration all samples had to be placed to the horizontal position for a maximum of 2 min. Gravistimulated cells were placed horizontally for the indicated times before extraction whereas control cells, which were regarded as unstimulated samples, were directly transferred from vertical orientation to the microscope stage. To avoid blue-light induced cell division of protonemata, extraction of this cell type was performed under red light conditions, and a red filter was placed in the light path of the microscope.

Total mRNA was isolated from cell extracts of rhizoids and protonemata by using the Oligotex Direct mRNA Micro Kit (Qiagen). PolyA$^+$-mRNA was bound to polystyrene-latex particles (1.1 µm in diameter) by hybridization with covalently linked oligo dT-nucleotides ($dC_{10}T_{30}$) under high-salt conditions. The Oligotex beads were collected by centrifugation and mRNA transcripts were eluted from the particles by lowering the ionic strength. The protocol was based upon the procedure for isolation of polyA$^+$-mRNA from animal cells denoted in the Qiagen Oligotex Handbook and specifically adapted for a maximum yield of RNA from characean samples:

- mix thoroughly the cell lysate
- add 800 µl dilution buffer ODB, mix thoroughly and centrifuge 6 min at maximum speed
- transfer supernatant to a fresh tube
- add 20 µl Oligotex suspension, mix thoroughly and incubate for 10 min at RT
- centrifuge 10 min at maximum speed, carefully remove supernatant
- resuspend the Oligotex:mRNA pellet thoroughly in 100 µl buffer OL1
- add 400 µl buffer ODB, incubate 3 min at 70° C and 10 min at RT
- centrifuge 10 min at maximum speed
- resuspend the pellet in 350 µl washing buffer OW1, mix and transfer the sample onto a small spin column placed in a 1.5-ml microcentrifuge tube
- centrifuge 2 min at maximum speed, discard the flow-through
- pipet 350 µl washing buffer OW2 onto the column, centrifuge 2 min at maximum speed, discard the flow-through
- repeat previous step
- transfer the spin column to a fresh microcentrifuge tube and pipet 20 µl hot (70° C) elution buffer OEB onto the column, pipet up and down three or four times to resuspend, centrifuge 2 min at maximum speed
- store eluted mRNA at –80° C until use

#### 2.7.4.2 Reverse transcription

The mRNA templates present in the extracts were reversly transcribed into cDNA by using the ProtoScipt First Strand cDNA Synthesis Kit (New England Biolabs, Frankfurt, Germany) according to the manufacturer's instruction except that fluorescently labeled oligo dT-anchor primer T17mod was used instead of the oligo dT-primer provided with the kit.

- Mix in a sterile microcentrifuge tube placed on ice:

| | | |
|---|---|---|
| 10 | µl | RNA extract |
| 2 | µl | oligo dT-anchor primer T17mod (80 µM) |
| 4 | µl | dNTPs |
| 16 | µl | |

- heat for 5 min at 70° C, spin briefly, put promptly on ice

- add:

| | | |
|---|---|---|
| 2 | µl | 10× RT buffer |
| 1 | µl | RNase inhibitor |
| 1 | µl | M-MuLV Reverse Transcriptase |
| 20 | µl | |

- incubate for 60 min at 42° C
- inactivate the enzyme at 42° C for 5 min
- store cDNA at –20° C

The presence of residual DNA in the RNA extracts was tested in control reactions by either treating the extracts with RNase prior to cDNA-synthesis or replacing the reverse transcriptase by nuclease-free water. In an additional negative control, the RNA extract was replaced by nuclease-free water to test for contaminations of the reaction with external RNA. If PCR-amplification products were detected in any of the negative controls, cDNA synthesis was repeated with fresh RNA extract. As positive control, cDNA was prepared from total rat liver RNA, and a specific DNA sequence was PCR-amplified by using the set of gene specific primers provided with the kit.

#### 2.7.4.3 Random-primed PCR

Random fragments of the 3'mRNA-ends were amplified by random-primed PCR which was performed according to the standard PCR protocol using the fluorescently labeled oligo dT-anchor primer T17mod, a decamer random primer and the synthesized cDNA as template. A variety of different random primers (Table VI) was used in parallel PCR reactions to generate fragments from a large number of mRNA transcripts present in the extracts. The cDNA-template was replaced by sterile water in negative control reactions.

In the first PCR-amplification cycles the random primer was annealed at low temperature in order to produce a maximum number of fragments which were subsequently amplified under more specific annealing conditions. The number of cycles was optimized for each experiment with respect to the number of PCR products and their corresponding intensities.

| | | | |
|---|---|---|---|
| 5 | min | 95.0° C | |
| 30 | sec | 95.0° C | × 3 – 10 |
| 1 | min | 33.0° C | |
| 1 | min | 72.0° C | |
| 30 | sec | 95.0° C | × 30 – 40 |
| 1 | min | 64.8° C | |
| 1 | min | 72.0° C | |
| 10 | min | 72.0° C | |
| | | 4.0° C | |

#### 2.7.4.4 Capillary electrophoresis

For fragment analysis of the fluorescently labeled products of random-primed PCR and for the detection of labeled products of gene-specific PCR, capillary electrophoresis was performed with an ABI Prism 310 Genetic Analyzer (Applied Biosystems, Foster City, USA). For sample preparation 1 µl of PCR-reaction mix or 3 µl of gel-eluted DNA was mixed with 12 µl deionized formamide and 0.5 µl size standard (ROX 2500; Applied Biosystems) in electrophoresis vials (Applied Biosystems). The samples were heated to 95° C for 5 min to denature the DNA and promptly placed on ice for 2 min. For capillary electrophoresis, samples were loaded on a silica capillary that was filled with polymer (Applied Biosystems 310 Genetic Analyzer Performance Optimized Polymer) and immersed in reaction buffer (Applied Biosystems ABI Prism Buffer with EDTA). The PCR products present in each sample were separated according to their mobility in an electric field produced by the application of high tension (15 kV). For each sample, the injection time was 10 s and run time was 30 – 45 min. The PCR products that were fluorescently labeled with the 6-FAM (6-Carboxyfluorescein) modification of one of the primers were detected by an argon laser. Data analysis was done using the GeneScan software (Applied Biosystems) with the internal marker serving as size standard for the determination of fragment size. Screenshots were taken in pct-format and converted to jpg-format using Adobe Photoshop 7.0.

#### 2.7.4.5 Isolation of gene fragments displaying differential expression

Gene fragments that displayed distinct differences in the expression rate of the corresponding gene in the compared samples – revealed by an at least two-fold difference in fluorescence intensity on capillary electrophoresis in at least two parallel random-primed PCR reactions – were processed for sequence analysis. For the isolation of a fragment, the PCR-reaction mix with the highest content of the product was run on a 3% agarose gel for 3 h at 70 V. After staining of the gel thin bands were collected in the size range of the corresponding fragment, and DNA was eluted with 30 µl. The fraction comprising the designated fragment was identified by capillary electrophoresis and stored at –20° C for cloning. The fragment was named after the random primer used in the PCR reaction and after its size in base pairs (bp), e.g. B10-568. After sequencing of the gene fragment (see below), differential expression of the corresponding gene was verified by gene specific PCR according to the standard protocol with cDNA-templates and gene-specific primers. The forward primer was modified with the 6-FAM fluorescence label at its 5'-end so that expression levels in the different samples could be analyzed by capillary electrophoresis.

#### 2.7.4.6 Cloning, transformation and sequencing

Isolated fragments of the random-primed PCR reaction or any other PCR products were cloned into the linearized vector pGEM-T Easy of the pGEM-T Easy Vector System I (Promega, Mannheim, Germany) at the single 3'-T overhangs of the insertion site. Negative controls omitting the DNA insert and positive controls using a control-insert DNA provided with the kit were performed as described in the user's manual. The ligation reaction was mixed in a 0.5 ml-tube.

| | | |
|---|---|---|
| 5 | µl | 2× rapid ligation buffer |
| 1 | µl | pGEM-T Easy vector |
| 3 | µl | template (eluted PCR product) |
| 1 | µl | T4 DNA ligase 3u/µl |
| 10 | µl | |

Ligation was performed for 2 h at RT or overnight at 4° C. Competent E. coli cells of strains DH5α or JM109 were prepared as described under 2.7.3 and slowly thawed on ice. Each

ligation reaction was gently mixed with 50 µl of bacteria and placed on ice for 20 min. As negative control, 50 µl of bacteria was processed without any vector. Cells were heat-shocked for 45 s at 42° C and immediately returned to ice for 5 min before 550 µl SOC medium was added, and cultures were incubated for 2 – 3 h at 37° C with shaking.

For growing bacterial colonies, 150 – 300 µl of each of the transformation and control cultures was plated onto duplicate LB/amp/IPTG/X-GAL plates and incubated overnight at 37° C. Successful transformation with the cloned plasmid was indicated by the white color of colonies whereas no insert was present in blue colonies. If any bacterial colonies were detected on the control plates with non-transformed bacteria the experiment was discarded, and the ligation reaction repeated. Several positive colonies containing the cloned insert were transferred to a replica plate (LB/amp) with a sterile tooth pick and diluted in 100 µl sterile water. The replica plate was incubated for 8 h at 37° C and stored at 4° C.

To determine the insert size of the transformed colonies the diluted bacteria suspension was used as template for in cell-PCR that was performed according to the standard PCR protocol with primers M13F (forward) and M13R (reverse) flanking the insertion site of the vector. Inserts were amplified using the following cycler program with the extension time of each cycle at 72° C being adapted to the size of the fragment that had been cloned (1 min of extension per 1 kb (kilobases) insert size):

| | | | |
|---|---|---|---|
| 5 | min | 95.0° C | |
| 30 | sec | 95.0° C | ⎫ |
| 1 | min | 64.8° C | ⎬ × 40 |
| 0.5 – 2 | min | 72.0° C | ⎭ |
| 10 | min | 72.0° C | |
| | | 4.0° C | |

PCR products which matched the size of the cloned insert were purified from an agarose gel, eluted in 30 µl elution buffer and sequenced at MWG (Ebersberg, Germany) using value reads with primers M13F and M13R for forward and reverse sequencing, respectively. The obtained sequences were analyzed as described under 2.7.6.

### 2.7.5 RACE-PCR

Starting from known sequences of differentially expressed genes and of the characean myosin 5'RACE-PCR was performed using the 5'RACE-System (Invitrogen, Karlsruhe, Germany) in order to determine adjacent parts of the gene sequence in 5'-direction of the corresponding mRNA. All material was autoclaved for one hour, and all reagents were prepared with nuclease-free water in order to avoid degradation of the RNA by RNases. Positive control experiments for all steps of the RACE-protocol were performed according to the instruction manual using control RNA and cDNA templates and control gene specific primers provided with the kit.

The extract of polyA$^+$-mRNA served as template for cDNA synthesis with a first antisense gene-specific primer (GSP 1) binding to the mRNA within the sequence of the corresponding gene fragment:

- mix in a 0.5 ml-tube placed on ice:
  - 1.0 µl primer GSP 1 (2.5 µM)
  - 14.5 µl polyA$^+$-RNA extract
- denature the RNA for 10 min at 70° C, chill on ice for 1 min and collect the contents of the tube by brief centrifugation
- add in the given order:
  - 2.5 µl 10× PCR buffer
  - 2.5 µl 25 mM $MgCl_2$
  - 1.0 µl 10 mM dNTP-mix
  - 2.5 µl 0.1 M dithiothreitol
- mix gently, spin down and place for 1 min at 42° C
- add 1 µl reverse transcriptase SuperScript II and mix gently
- incubate for 50 min at 42° C
- inactivate the enzyme at 70° C for 15 min, centrifuge 20 s and place reaction at 37° C
- add:
  - 0.5 µl RNase H 5u/µl (Fermentas)
  - 0.5 µl RNase T1 1000u/µl (Fermentas)
- mix and incubate for 30 min at 37° C
- collect the reaction by brief centrifugation and place on ice

The cDNA was purified and eluted with 50 µl elution buffer using the QIAquick PCR Purification Kit (Qiagen) instead of the purification system proposed in the RACE-manual.

A homopolymeric oligo dC-tail was added on the 3'-end of the cDNA in order to create a binding site for the abridged anchor primer which was required for PCR amplification:

- mix in a 0.5 ml tube placed on ice:

| | | |
|---|---|---|
| 6.5 | µl | water |
| 5.0 | µl | 5× tailing buffer |
| 2.5 | µl | 2 mM dCTP |
| 10.0 | µl | purified cDNA |

- incubate for 3 min at 94° C, chill for 1 min on ice, spin down and place on ice
- add 1 µl TdT (terminal deoxynucleotidyl transferase) and mix gently
- incubate for 10 min 37° C
- inactivate the enzyme at 65° C for 10 min, spin down and place reaction on ice

The tailed cDNA was PCR-amplified with a second gene-specific primer (GSP 2) annealing to the cDNA at a nested position (3' to GSP 1) and an Abridged Anchor Primer (AAP) binding to the homopolymeric tail at the 3'-end of the cDNA. In order to reduce non-specific amplification and to increase target yield, the PCR reaction was performed as hot-start PCR using the Fermentas Taq polymerase system with the enzyme being added to the reaction mix after initial denaturation of the template at 95° C. The primer annealing temperature was adapted according to the calculated melting temperature provided by the manufacturer. The PCR reaction was mixed in a 0.2 ml-reaction tube placed on ice:

| | | |
|---|---|---|
| 31.5 | µl | sterile water |
| 5.0 | µl | 10× PCR buffer (Fermentas) |
| 3.0 | µl | 25 mM $MgCl_2$ (Fermentas) |
| 2.0 | µl | primer GSP 2 (10 µM) |
| 2.0 | µl | primer AAP (10 µM) |
| 1.0 | µl | dNTP mix (10 mM each) |
| 5.0 | µl | tailed cDNA |
| 0.5 | µl | Taq polymerase 5u/µl (Fermentas) |
| 50.0 | µl | |

Amplification program:

| | | | |
|---|---|---|---|
| 2 | min | 95.0° C | |
| 30 | sec | 95.0° C | × 35 |
| 1 | min | 55 – 62° C | |
| 3 | min | 72.0° C | |
| 10 | min | 72.0° C | |
| | | 4.0° C | |

To increase the yield of specific PCR product, DNA from the first PCR was reamplified in a nested PCR with a nested gene-specific primer GSP 3 and the Abridged Universal Amplification primer AUAP binding to the adapter region of AAP. As for the first amplification reaction PCR was performed as hot-start PCR, and primer annealing temperatures were adapted.

Mix in a 0.2 ml reaction tube placed on ice:

| | | |
|---|---|---|
| 33.5 | µl | sterile water |
| 5.0 | µl | 10× PCR buffer (Fermentas) |
| 3.0 | µl | 25 mM $MgCl_2$ (Fermentas) |
| 1.0 | µl | primer GSP 3 (10 µM) |
| 1.0 | µl | primer AUAP (10 µM) |
| 1.0 | µl | dNTP mix (10 mM each) |
| 5.0 | µl | template (1:100 dilution of first PCR reaction) |
| 0.5 | µl | Taq polymerase 5u/µl (Fermentas) |
| 50.0 | µl | |

| | | | |
|---|---|---|---|
| 2 | min | 95.0° C | |
| 30 | sec | 95.0° C | × 35 |
| 1 | min | 57 – 64° C | |
| 3 | min | 72.0° C | |
| 10 | min | 72.0° C | |
| | | 4.0° C | |

Amplification products of the first PCR reaction and of the nested PCR were purified from an agarose gel, cloned, and sequenced as described under 2.7.4.6.

### 2.7.6 Sequence analysis and alignment

The data obtained from sequencing of amplified fragments was analyzed using the tools provided by the ExPASy server (Expert Protein Analysis System, URL: http://www.expasy.ch/; Gasteiger et al. 2003) of the Swiss Institute of Bioinformatics and Clone Manager 4.0 software (Scientific & Educational Software, Cary, USA). Homology search of nucleotide and amino acid sequences and alignments with database entries were done using BLAST (Basic Local Alignment Search Tool) at the web page of the NCBI (National Center for Biotechnology Information; URL: http://www.ncbi.nlm.nih.gov/BLAST) and ClustalW at the web page of the European Bioinformatics Institute (URL: http://www.ebi.ac.uk/clustalw/index.html). Nucleotide and amino acid sequences are listed in this study according to the IUB (International Union of Biochemistry) one letter code.

## 2.8 MAXUS-5 sounding rocket flight experiment

Parabolic flights of sounding rockets such as TEXUS (technological experiments under reduced gravity) and MAXUS (enlarged version of TEXUS) represent a powerful facility for conducting experiments under microgravity (μ*g*) conditions. They are well suited for biological experiments since they provide relatively long phases of microgravity conditions in the range of 7 to 13 min. These durations are much longer than the microgravity phases of free-fall experiments in a drop tower (4.5 to 9 s) and of parabolic plane flights (31 times 22 s μ*g*-conditions within 120 min). In contrast to long-term microgravity experiments on Space-Shuttle flights, satellite flights (Foton capsules) or on board the International Space Station (ISS), sounding rocket experiments allow the direct access of the investigator to the experiment before and after the flight. By means of late-acess units samples can be delivered to the payload module shortly before lift-off and immediately be transported back to the ground laboratory for analysis of the data after landing of the payload. During the flight, the experiment data are downlinked on-line and the experimenter is able to control and modify the settings of the module via telecommand from ground. It has previously been demonstrated that parabolic flights of sounding rockets are highly suited to study the actomyosin-mediated

transport mechanisms of statoliths in gravity-sensing characean cells by microscopic observation in microgravity (Volkmann et al. 1991; Buchen et al. 1993; Braun et al. 2002). The MAXUS-5 experiment was designed to specify the lateral forces of molecular interactions between statoliths and the actin cytoskeleton by determining the threshold acceleration level required for statolith displacement.

### 2.8.1 Sample preparation

Samples of characean rhizoids and protonemata were mounted in two different types of vacuum-tight cuvettes. Fixation cuvettes were designed for chemical fixation of the samples at the end of the microgravity phase whereas samples in the observation cuvettes remained unfixed in order to discover acceleration-induced curvature responses. Both types of cuvettes consist of a core frame made of $V_2A$ steel, two Plexiglas windows and two aluminum cover windows. They are sealed by o-rings between the core frame and the Plexiglas windows. For the flight, fixation cuvettes were connected to the fixation unit of the module, which allowed the timer-controlled exchange of the internal solution.

Flight samples were prepared starting 10 hours before lift-off. Samples of protonemata were prepared under red light, and windows were covered with photoresistant tape after preparation in order to avoid blue-light induced cell division. Small agar-blocks containing embedded nodes with bundles of short rhizoids or with outgrowing protonemata were transferred to the cuvettes. Observation cuvettes were completely filled with agar whereas samples in the fixation cuvettes were embedded in a thin layer. Fixation cuvettes were filled with distilled water using a syringe and plugged until used. Five hours before lift-off those samples were selected for the flight that exhibited normal cell shape and constant growth as revealed by microscopic control.

### 2.8.2 Payload module TEM 06-R01M

The payload module TEM 06-R01M which was constructed by EADS ST (Bremen, Germany) was designed to study the effect of defined lateral acceleration forces on the position of statoliths and on growth orientation in vertically oriented characean rhizoids and protonemata. The rotatable platform of the module was equipped with two microscopic units (one for each cell type) and with a fixation unit. Each of the microscopic units consists of a

tube redirected by 90°, a 20× objective lens (Zeiss, Oberkochen, Germany) and a black/white CCD camera chip XC-ST50 (Sony, Cologne, Germany). In the protonema unit a red filter was installed in the optical path behind the light source. During the flight, the microscopic images were downlinked on-line to the ground facility at Esrange, and the position of the cuvettes and the focus were adjusted by telecommand. The fixation unit comprised a reservoir tank containing the chemical fixative connected to the filler plugs of the fixation cuvettes and intercepting tanks receiving the displaced solution from the release plugs.

The flight cuvettes with rhizoids and protonemata were mounted on two late-access units (one for each cell type), that were inserted into the module approximately 100 min before lift off. One observation cuvette and one fixation cuvette were located on each of three different positions of the late-access units at defined distances from the center of the platform. Samples of the observation cuvettes at the middle position of each late-access unit were available for in-vivo video microscopy during the rocket flight. After insertion of the samples the temperature in the module was adjusted to 21° C by peltier elements.

### 2.8.3 Experiment procedure

The ESA (European Space Agency) MAXUS-5 sounding rocket was launched from the satellite station Esrange, near Kiruna in northern Sweden on April 1, 2003. It reached an altitude of 700 km and provided microgravity conditions (< $10^{-4}g$) over a period of 736 s (Table II).

**Table II** *Technical data of the MAXUS-5 sounding rocket flight*

Time points of the parabolic flight are indicated in s after lift-off. Data were provided by Kayser-Threde (Munich, Germany) and EADS ST.

| | |
|---|---|
| Launch date | April 1, 2003 |
| Launch time | 8:00 LT (local time) |
| Height of apogee | 701.3 km |
| Start of µg (< $10^{-4}g$) | +95 s |
| End of µg | +831 s |
| Reentry | +858 s |

The threshold acceleration level that induces lateral displacement of statoliths in characean rhizoids and protonemata was determined by rotating the platform of the experiment module TEM 06-R01M during the microgravity phase of the rocket flight. During rotation the vertically oriented samples on the three different radii of the platform experienced lateral accelerations of 0.05$g$, 0.14$g$ and 0.25$g$. During the microgravity phase, the movements of statoliths and first gravitropic responses were observed in rhizoids and protonemata at the middle position of the platform by in-vivo video microscopy. Timer-controlled chemical fixation (3% glutaraldehyde, 0.1 M

Pipes, pH 7.0) at the end of the microgravity phase (+800 s) conserved the position of statoliths and allowed documentation and statistic analysis of the redistribution of statoliths caused by the laterally applied accelerations on ground. Rhizoids and protonemata in the observation cuvettes of each acceleration level remained unfixed, and microscopic observation after early retrieval of the late access units allowed the detection of any potential curvature responses that were induced by the lateral acceleration stimuli.

For documentation of the final statolith distribution after centrifugation in microgravity the geometrical center of the statolith complex of chemically fixed rhizoids was determined according to Hodick (1994) and averaged for each acceleration level. The microscopic images were overlaid with a Cartesian coordinate system with its origin at the cell vertex and the median cell axis as the x-axis. The position of each statolith was determined by its x- and y-value in the coordinate system. Averaging of coordinate values of all statoliths resulted in the geometrical center of the statolith complex.

For further analysis of the acceleration-induced statolith displacement in all chemically fixed cells and in the living cells of the observation cuvette of the 0.14*g* acceleration level, the distribution of statolith frequency across the cell diameter was determined. Microscopic images were overlaid with a lattice (30 × 30 µm, box size 3 × 3 µm), and the number of boxes blackened by the presence of statoliths in all rhizoids of each set of samples was summed up for each column and divided by the number of cells analyzed. This method provided distribution diagrams of statoliths along the lateral cell axis.

## 2.9 Parabolic Plane flight experiments

By providing alternating levels of hypergravity and microgravity conditions parabolic plane flights are highly suited to study the effect of reduced or enhanced accelerations on gravity sensing in biological specimens. Although the duration of a single microgravity phase is too short to detect changes in the kinetics of gravitropic curvature reactions, it is very well feasible to study the cumulative effect of all microgravity phases of the flight profile which sum up to a total duration of approximately 12 min or 10% of the total flight time.

Each parabolic flight maneuver of the Novespace Airbus A300 Zero-G (Fig. 1) provides microgravity conditions for 22 s. The aircraft is pulled up with full engine power from the horizontal flight position to an ascending angle of 47°. At this ‘angle of attack’, the thrust is reduced to a minimum (‘injection’) so that the forces acting on the aircraft compensate each

other during the parabolic flight curve and – similar to an object in a free-fall situation – gravity is the only remaining acceleration. The aircraft is weightless until the engines are reset to full power at a descending angle of 42° (‘pull out’) and the aircraft is brought back to the normal flight position. Before and after each microgravity phase the aircraft is subjected to hyper-g accelerations in the range of 1.8g for approximately 20 s during pull-up and during pull-out. The profile of a parabolic flight comprises 31 parabolas flown within 120 min on each of three flight days per campaign.

The present experiment was designed to characterize the functional mechanism of receptor activation in characean rhizoids and to investigate if receptor activation depends on mechanical forces exerted by the weight of the statoliths. The experiment was performed during the 36th ESA parabolic flight campaign at Bordeaux airport, France, in March 2004, and during the 6th DLR (Deutsches Zentrum für Luft- und Raumfahrt) parabolic flight campaign at Cologne airport, Germany, in September 2004.

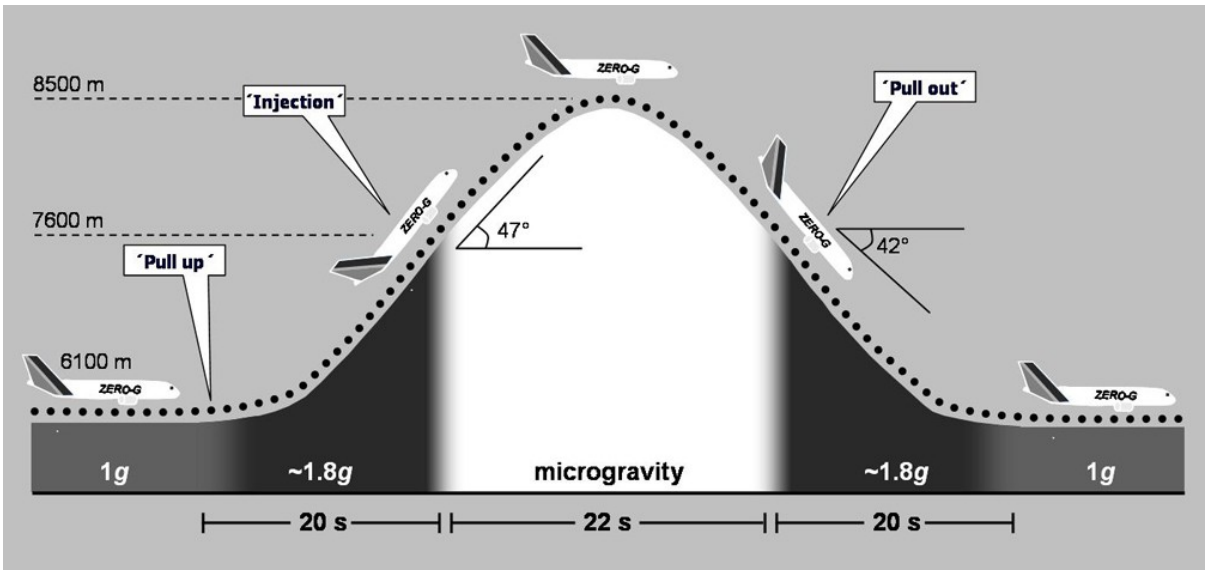


**Fig. 1** *Profile of the parabolic flight maneuver of the A300 Zero-G aircraft*
Each parabola provides a microgravity phase of 22 s that is preceded and followed by hypergravity conditions of 1.8g. The maneuver is performed 31 times on each flight and the microgravity phases sum up to a total duration of approx. 10% of the total flight time of 120 min. For a detailed description of the flight maneuver see text.

### 2.9.1 Flight hardware and procedures

The experiment hardware that was described in detail by Hauslage (2005) was mounted on a custom-made aluminium rack and included the specimen containers and a centrifuge for in-flight controls. A modified Biorack microscope equipped with a video camera was used for observations of statolith movements during the flight phases. Video sequences were recorded in MPEG2 format on a laptop computer. In order to reduce vibrations, all specimen containers and the centrifuge were mechanically isolated from the rack by 10-mm silicon foam plates (Castan GmbH, Ludwigsburg, Germany).

In the present experiment it was tested if activation of the gravireceptor molecule in characean rhizoids depends on mechanical forces exerted by the weight of sedimented statoliths. Therefore curvature angles of flight samples whose sedimented statoliths were weightless during the microgravity phases of the parabolic flight were compared to the curvature angles of in-flight controls which were mounted on the reference centrifuge of the experiment rack and centrifuged at 1*g* during the microgravity phases. Flight samples and in-flight controls were tilted by 90° during the flight beginning 10 min prior to the first parabola. This warranted that sedimentation of statoliths onto the lateral cell flank was completed under 1*g* conditions in all rhizoids and that the following acceleration profile was applied to cells with fully sedimented statoliths. The samples were tilted back to the vertical orientation after the last parabola of the flight profile. After landing, photographs of the rhizoids in both sets of samples were recorded by video microscopy. The maximally achieved curvature angles were measured and statistically analyzed. On the 36th ESA campaign additional ground control samples were positioned horizontally under continuous 1*g* conditions for the same total gravistimulation time as the flight samples and in-flight controls. During the flight video sequences of rhizoids on the Biorack microscope were recorded in order to analyze the position of the statolith complex during the different acceleration levels of the flight profile.

### 2.9.2 Preflight control experiments

Control experiments under 1*g*-conditions on ground were performed to assess the effect of hypergravity conditions and the effect of short-term removal of sedimented statoliths from the plasma membrane on gravitropic curvature. In all control experiments, rhizoids where initially tilted by 90° for 10 min to allow undisturbed sedimentation of statoliths.

To test if increasing the weight of sedimented statoliths alters the gravitropic response, gravistimulated rhizoids were laterally centrifuged parallel to the direction of the gravistimulus for 15 min at 2, 3, 4 or 5*g*. The maximally achieved growth angles were compared with control cells which were gravistimulated at 90° for 25 min at 1*g*. For simulating the short-term hypergravity phases of the parabolic flight profile, rhizoids were intermittently centrifuged 62 times at 2*g* for 20 s within a total gravistimulation time of 120 min, and final curvature angles of these cells were compared with controls cells which were continuously gravistimulated at 1*g* for 120 min.

The effect of short-term interruption of the contact of sedimented statoliths with the plasma membrane on the gravitropic response was tested by inverting gravistimulated cells from 90° to 270° 31 times for 30 s, 22 s, 10 s, or 5 s within a total of 120 min according to the flight profile. As for the other control experiments, maximally achieved curvature angles of the intermittently inverted rhizoids were measured and compared with control samples that were continuously gravistimulated for 120 min at continuous 1*g* conditions. For tracking the movements of statoliths following the inversion of gravistimulated cells, high-magnification video microscopy was used. Rhizoids were mounted on the rotatable stage of a vertically positioned Axioskop microscope (Zeiss), and statoliths were observed with a Plan Neofluar 100× oil immersion lens (Zeiss). Rhizoids were gravistimulated for 10 min at 90° and subsequently inverted to 270° by tilting the microscope stage. Digital images of the apical cell regions were recorded before and after inversion in 1-s intervals with an AxioCam HS camera (Zeiss). For statistical analyses of statolith movements, only those statoliths were tracked that were considered to be sedimented on the plasma membrane at the moment of inversion (t = 0). A line was drawn as reference line to indicate the initial position of sedimented statoliths. The distances between statoliths and the reference line were documented and measured using the AxioVision software (Carl Zeiss Vision GmbH, Hallbergmoos, Germany).

## 2.10 Electron microscopy

The electron microscopic part of the study was intended to develop and establish procedures for the preparation of samples of characean rhizoids by high-pressure freeze fixation and freeze substitution. These high-quality samples were used for detailed ultrastructural analyses by 3D dual-axis electron tomography and for subcellular immunolocalization of protein

epitopes. High-pressure freeze fixation and electron tomography were conducted in the lab of Prof. L. Andrew Staehelin (Department of Molecular, Cellular, and Developmental Biology, University of Colorado, Boulder, USA).

### 2.10.1 High-pressure freeze fixation

Samples for ultrastructural analyses and immuno-electron microscopy were prepared using high-pressure freeze fixation (Gilkey and Staehelin 1986; Moor 1987; Dahl and Staehelin 1989) with a Baltec HPM010 (Technotrade, Manchester, USA). Small characean nodes with very short rhizoids were cut off from agar-embedded thallus pieces soaked with either 150 mM sucrose or 150 mM mannitol which were used as cryoprotectants. The node was pulled out of the agar and transferred to a type-A freezing hat with a cavity of 150 µm (Ted Pella, Redding, USA) that was filled with the cryoprotectant. The specimen sandwich was completed by putting on a second hat with its cavity facing the cavity of the first hat forming a specimen chamber with a depth of 300 nm. The samples were transferred to the specimen holder inserted into the high-pressure freezer and frozen under high pressure (2100 bar) with liquid nitrogen ($lN_2$) as cryogen within 50 ms and with a cooling rate of 4000° C $s^{-1}$. Specimen sandwiches were stored in liquid nitrogen and transferred to $lN_2$-cooled cryocaps containing the freeze substitution medium.

### 2.10.2 Freeze substitution and embedding

Different substitution protocols were developed in order to achieve the best results for each microscopic application, i.e maximum contrast for ultrastructural analysis and excellent preservation of protein epitopes for immuno-electron microscopy. To avoid heating of the samples and ice crystal formation during exchange of the substitution media all solutions and pipettes were pre-chilled to the corresponding temperature of the previous step. The solutions used for freeze substitution were prepared with pure water-free acetone (Electron Microscopy Sciences). Chemical fixatives, i.e. GA (glutaraldehyde), TA (tannic acid), $OsO_4$ (osmium tetroxide) and UA (uranyl acetate), were added as indicated in the protocols.

For ultrastructural analyses rhizoid samples were freeze substituted according to the following protocol:

| | | |
|---|---|---|
| –80° C | 3 d | 1% GA + 0.1% TA in acetone |
| | | wash 2× with acetone |
| | 2 d | 2% $OsO_4$ in acetone |
| –20° C | 1 d | 2% $OsO_4$ in acetone |
| +4° C | 1 d | 2% $OsO_4$ in acetone |
| RT | | wash 3× with acetone |

After freeze substitution, samples were removed from the freezing hats, transferred to fresh cryocaps and infiltrated at RT in increasing concentrations of Epon resin (Ted Pella) according to the following schedule: 12 h each in 5, 10, 20, 30, 50 and 70% resin in acetone, 12 h in 100% resin and 2 h in fresh resin. Rhizoids were transferred to flat embedding molds, and polymerization was performed at 60° C for 16 h under vacuum.

The samples for immuno-electron microscopy were freeze substituted and embedded in Lowicryl HM20 using a freeze substitution unit (Leica, Vienna, Austria) that provided controlled temperature conditions and allowed UV-polymerization of the resin at low temperature.

| | | |
|---|---|---|
| –90° C | 90 h | 0.25% GA + 0.1% UA in acetone |
| | 6 h | warm to –60° C at a rate of 5° C per hour |
| –60° C | | wash 3× with acetone, remove samples from freezing hats |
| | 12 h | acetone |
| | 1 d | 2% $OsO_4$ in acetone |
| | 4 h each | 30 and 60% Lowicryl in acetone |
| | 12 h | 90% Lowicryl in acetone |
| | 4 h each | 2× 100% Lowicryl |
| | 12 h | 100% Lowicryl |
| | | transfer samples to pre-chilled polymerization chambers (see below) |
| | 48 h | polymerization under UV light |

The polymerization chambers were constructed by sticking rubber frames with an inner diameter of 19 mm and a thickness of 1 mm to microscope slides and covering with a plastic coverslip. Polymerization yielded translucent platelets with embedded rhizoid samples.

### 2.10.3 Sample preparation for electron tomography

For electron tomography 250 nm-sections were prepared with an Ultracut S ultramicrotome (Leica) and collected on Formvar-coated copper slot grids (0.5% Formvar in ethylene dichloride; Electron Microscopy Sciences). Sections were counterstained with Reynold´s lead citrate and uranyl acetate (3% in 70% methanol) for 3.5 and 8 min, respectively. Washing was performed with 70% methanol, 40% methanol and distilled water for 1 min each. After staining, 15-nm colloidal gold particles were added to both sides of the grid to be used as fiducial markers for aligning the series of tilted images. A 10 µl-droplet of gold suspension was applied to each side of the grid and removed with filter paper after 20 min of incubation at RT. Grids were thoroughly washed by submerging in distilled water and allowed to dry.

### 2.10.4 Sample preparation for immunogold labeling

Rhizoids were identified in the polymerized resin platelets by microscopic observation, excised with a razor blade and stuck to mounting blocks with two-component glue. Thin sections (~ 80 nm) were prepared with an Ultracut S ultramicrotome and collected on Formvar-coated nickel slot grids (0.5% Formvar in ethylene dichloride). For immunolabeling, grids were incubated on small droplets of the solutions in a humid chamber according to the following schedule:

- 10 min 0.1 N HCl
- 20 min block with 5% milk powder or BSA (bovine serum albumin) in PBST
- 2 h primary antibody diluted in PBST
- wash 3× with PBS-high Tween
- 1.5 h secondary antibody (gold conjugate) diluted in PBST
- wash 3× with PBS-high Tween
- wash with distilled water
- 2 – 4 min counterstaining with Reynold´s lead citrate
- wash 3× with distilled water
- 5 – 8 min counterstaining with 3% uranyl acetate in 70% methanol
- wash vigorously with distilled water in beaker
- allow grids to dry

For reducing unspecific labeling, antibody solutions were optionally supplemented with 2% milk powder or BSA. Control samples were prepared by omitting the primary antibody and incubating the grid on a droplet of PBST solution instead. Sections were observed at 60 – 80kV with either a CM 10 (Philips, Eindhoven, Netherlands) or an EM 10A (Zeiss) electron microscope. Depending on the equipment available, the microscopic images were recorded with a digital camera or on negative film.

### 2.10.5 Electron tomography

3D dual-axis electron tomography is an innovative tool for detailed ultrastructural studies at a resolution level that is greatly improved compared to conventional electron microscopy. At increasing tilt angles of the microscope goniometer, series of electron micrographs are recorded about two orthogonal axes. The single-axis tomograms that are computed from each of the image series are combined to the final dual-axis tomogram which comprises a set of serial tomographic slices at one-pixel distances. Using electron tomography, the cellular ultrastructure can be analyzed at a resolution of less than 4 nm, and the three-dimensional shape of cellular compartments can be visualized by modeling of the contours that are detected in the tomographic slices.

#### 2.10.5.1 Intermediate-voltage electron microscopy and acquisition of tilt series images

Electron tomograms of 250 nm-sections were prepared using a Tecnai TF30 intermediate-voltage electron microscope (FEI, Hillsboro, USA) operating at 300 kV. Single images (2048 × 2048 pixels) were taken at tilt angles of +60° to –60° at 1°-intervals about two orthogonal axes (Mastronarde 1997) and collected with a Gatan Megascan 795 digital camera (Gatan, Pleasanton, USA). Image series were recorded at magnifications of 12000× to 23000×.

#### 2.10.5.2 Three-dimensional tomographic reconstruction and modeling

The reconstruction of three-dimensional tomograms from the images of a tilt series was performed using the eTomo-application of the IMOD software package (version 3.3.8) which was designed at the University of Colorado (Mastronarde 1997) and is available for download at the IMOD home page (URL: http://bio3d.colorado.edu/imod). The images were aligned by

the software using the gold particles on the surface of the grids as fiducial markers. Each set of aligned tilts was reconstructed into a single-axis tomogram using the R-weighted backprojection algorithm (Gilbert 1972). Finally, the two single-axis tomograms were merged into a dual-axis tomogram using a warping procedure (Mastronarde 1997). Completed tomograms were displayed and analyzed with the 3dmod-application, the graphics component of the IMOD package (Kremer et al. 1996). Membranous structures, microtubules, actin filaments and all types of vesicles were modeled by drawing contours on single slices of a tomogram. The ‘imodmesh’-function was used to connect contours between the slices producing a three dimensional reconstruction of the modeled structures. Dimensions of cellular structures and compartments were measured using the ‘imodinfo’-command.

# 3 RESULTS

## 3.1 Molecular biology

The molecular biological part of the study aimed at the identification of genes that are involved in the regulation of gravitropism in characean rhizoids and protonemata by comparing gene expression patterns under differential conditions of gravistimulation. The mRNA extracts of rhizoids were used in addition for the determination of the nucleotide sequences of some strongly expressed genes in order to contribute to the expansion of genomic information of characean algae. Partial sequencing of a myosin from rhizoids was performed as preparation of a systematic molecular characterization of this protein class which is believed to play a crucial role for gravity sensing and tip growth by mediating a variety of different cellular processes.

Since characean algae are not very well established as model systems for molecular studies, basic procedures for the extraction, isolation and amplification of mRNA from rhizoids and protonemata had to be developed in this study. The optimized protocols established the basis for the analysis of gene expression patterns and for cDNA-sequencing.

### 3.1.1 Extraction of mRNA from characean rhizoids and protonemata

For the extraction of cytoplasm and isolation of mRNA, agar-embedded samples of rhizoids were used to avoid any contamination from liquid cultures. Nodes with attached rhizoid bundles were pulled out of the agar and frozen in liquid nitrogen. Frozen rhizoids were clipped from the nodes and solubilized in tubes containing extraction buffer. For the comparison of gene expression patterns, mRNA was extracted from control cells in vertical orientation and from gravistimulated cells which were placed horizontally for 20 and 45 min, respectively.

Total polyA$^+$-RNA was isolated from the cell extracts by hybridization to latex beads and collected by centrifugation. Highly abundant tRNA and rRNA molecules that do no bind to the beads due to the lack of a polyA-tail were washed out whereas mRNA was specifically isolated although it accounts for only 1 – 5% of the cellular RNA. Any procaryotic mRNA that might be present in the cell extracts was removed since it does not hybridize to the dT-oligonucleotides linked to the beads.

Capillary electrophoresis after random-primed PCR demonstrated that the mRNA-isolation procedure was highly effective and that degradation of RNA during processing of the samples was avoided: The amount of isolated mRNA was comparable in different samples, and the patterns of amplified fragments as well as peak intensities were almost identical (Fig. 2, 4). These observations demonstrated that mRNA extracts of rhizoids that were pulled out of the agar were very well suited for differential display analysis.

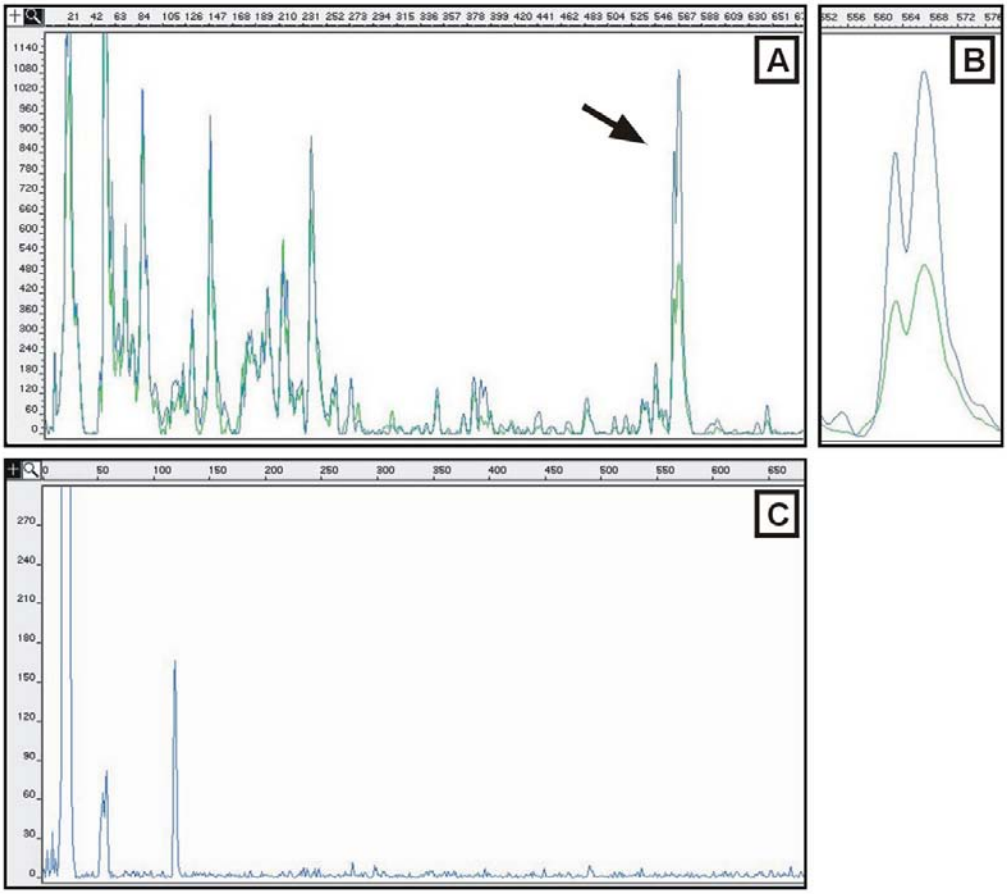


**Fig. 2** *Amplification products of random-primed PCR with primer B10*

A: Fragment patterns and peak intensities were widely identical in samples of unstimulated (green) and gravistimulated (20 min 90°; blue) rhizoids. Fragment B10-568 (arrow) which exhibited two-fold higher fluorescence intensity in gravistimulated samples as compared to unstimulated samples is enlarged in B.

C: In the control reaction without cDNA template no products were amplified. The peaks that are visible represent the fluorescently labeled primer and unspecific fluorescence signals that were detected throughout all PCR reactions.

x-axis: fragment length in bp; y-axis: relative fluorescence intensity

Alternatively, the cytosol of rhizoids and protonemata was extracted by inserting a microcapillary that was filled with extraction buffer (single-cell aspiration). Since it proved difficult to amplify products from extracts of single cells, several cells were pooled for each sample. mRNA from pooled extracts of 25 cells was sufficient as template for gene-specific PCR amplification (Fig. 3). However, single-cell aspiration was not an adequate extraction method for differential display analysis because the level of variation in mRNA-yield and in the pattern of random-primed PCR fragments in differentially stimulated samples was too high even when identical numbers of cells were extracted.

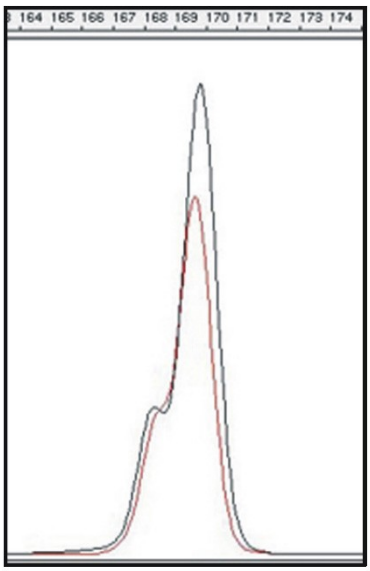


**Fig. 3** *Products of gene-specific PCR in samples obtained by single-cell aspiration*

A product with the expected length of 170 bp was specifically amplified in pooled extracts of 25 rhizoids (red) and protonemata (black) using gene-specific primers which bound within the sequence of the random PCR fragment B05-273. The difference in peak intensity between the samples is in the range of the experimental variation.

x-axis: fragment length in bp; y-axis: relative fluorescence intensity

### 3.1.2 Random-primed PCR

To compare the expression levels of mRNA transcripts in extracts of differentially stimulated samples, fragments of the 3'mRNA-ends were amplified by random-primed PCR and analyzed by capillary electrophoresis. Several different random primers were used in parallel to cover a broad range of transcripts. Capillary electrophoresis was used for fragment analysis since it has several advantages compared to gel electrophoresis: i) products are separated with very high resolution, ii) the fragment length can be determined very precisely, and iii) detection is very sensitive so that even rare products are displayed.

Due to the low amount of starting material, only some fragments representing highly expressed transcripts were present in samples that were obtained by single-cell aspiration. Therefore, extracts from bundles of agar-embedded rhizoids that were either unstimulated or gravistimulated by 90° for 20 or 45 min prior to mRNA extraction were used for differential

display analysis. In general, a high number of fragments in a size range of 100 – 600 bp was amplified in each random-primed PCR reaction whereas no products were detected in controls where the RNA template was omitted (Fig. 2). The patterns and expression levels of the fragments were very similar in stimulated and unstimulated samples as revealed by coinciding peak positions and fluorescence intensities in capillary electrophoresis. The overall similarity of the electropherograms was an important precondition for the identification and isolation of single fragments that displayed differential expression of the corresponding genes upon gravistimulation. Fragments that were isolated for cloning and sequencing were named after the random primer used for PCR amplification and the length of the fragment in bp (e.g. B10-568 represents a fragment with a length of 568 bp provided by PCR amplification with random primer B10).

### 3.1.3 Identification of differentially expressed genes

As described above, most of the random fragments exhibited equal transcription levels in unstimulated and gravistimulated cells. However, certain products displayed distinct differences in peak intensities in differentially stimulated samples and pointed thereby to the differential expression of the corresponding gene. The criteria for regarding a gene as differentially expressed were: i) an at least two-fold difference in fluorescence intensity of the corresponding fragment between gravistimulated and unstimulated samples, ii) the confirmation of the difference in the fluorescence levels in at least two parallel random-primed PCR reactions, and iii) the verification of the expression pattern observed after random-primed PCR by amplification of a specific gene product using gene-specific primers. An increase or decrease of fluorescence intensity in gravistimulated samples indicated a gravistimulation-dependent up- or down-regulation of the gene.

Several amplification products matched the criteria for differential expression in random-primed PCR and were subsequently isolated and cloned in order to determine the nucleotide sequence of the corresponding 3'mRNA-fragment. Since the genome of Chara is not sequenced, the nucleotide sequence of the fragment was usually not sufficient for identifying the corresponding gene. Therefore, the coding region of the gene was sequenced using 5'RACE-PCR technology in order to classify the gene according to homologies with sequences from other organisms that were available at genome databases.

One of the fragments that displayed a distinct difference in peak intensity after random-primed PCR was B16-292. In several parallel experiments the fluorescence level of B16-292 was at least 3-fold higher in gravistimulated samples (20 min 90°) as compared to unstimulated controls (Fig. 4). After isolation and sequencing of the fragment the expression pattern was verified by gene-specific PCR. The fluorescence intensity of the characteristic 186/189 bp-double peak was three times higher in gravistimulated as in unstimulated samples thereby confirming the results from random-primed PCR and pointing to an up-regulation of the corresponding gene upon gravistimulation.

Several runs of 5'RACE-PCR provided a sequence of 3127 nts (nucleotides) including the complete coding region of the gene with a length of 1878 nts which corresponds to a protein of 626 aa (amino acids). The nucleotide and amino acid sequences are shown in Fig. 5. BLASTX alignment of the translated nucleotide sequence displayed a very high level of homology (e-value in the range of 1e–120) with glucosyltransferases of Arabidopsis (*Arabidopsis thaliana*), rice (*Oryza sativa*), and other higher plants (Table VII). Homology of B16-292 with cellulose synthase-like proteins from rice (Table VII) is attributed to the fact that glucosyltransferases are components of the cellulose synthase multi-enzyme complex. The nucleotide and amino acid sequences of B16-292 were published as database entries entitled *Chara globularis putative glucosyltransferase* with the acc. nos. (genbank accession numbers) AY995817 and AAX98242, respectively.

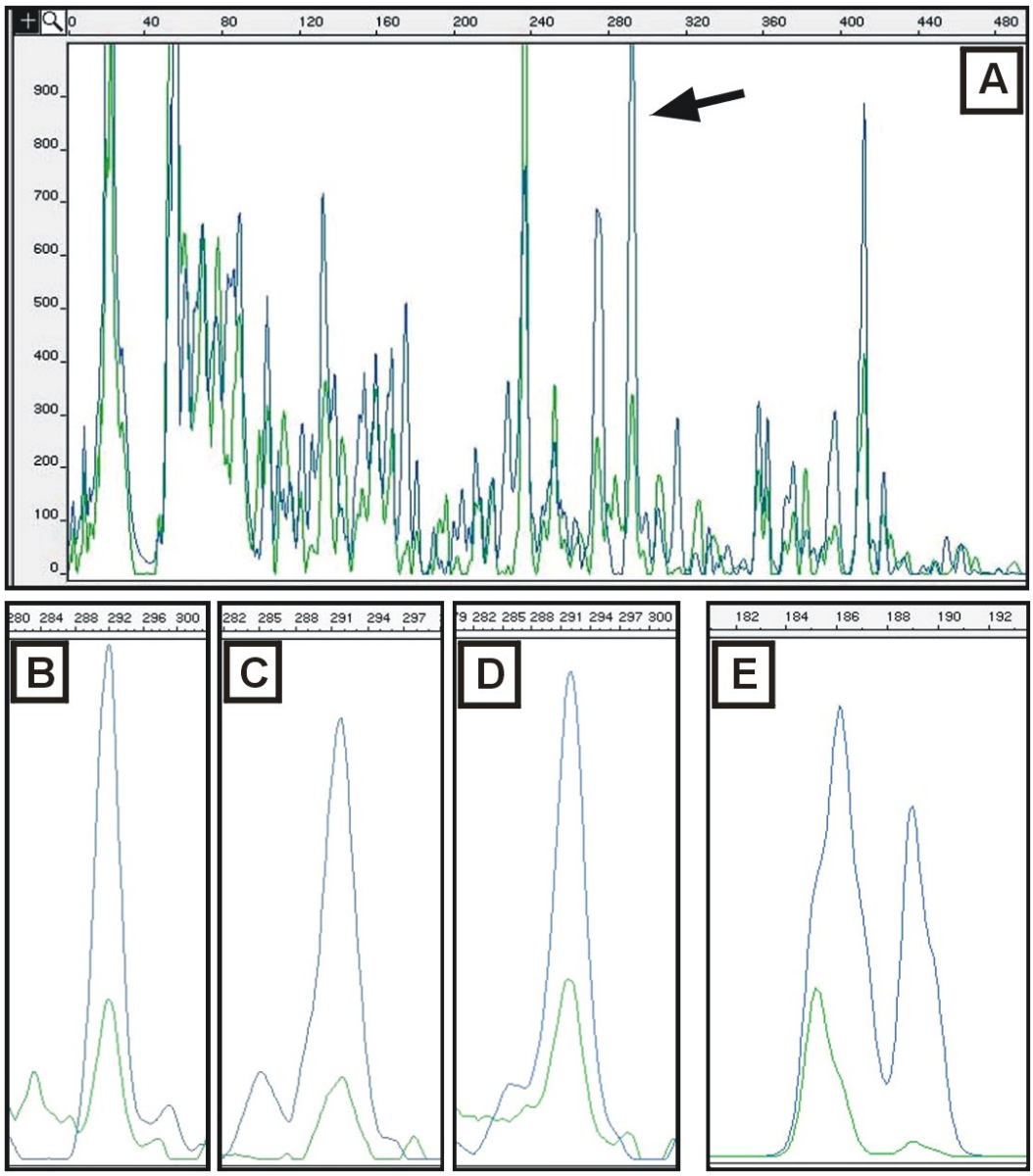


**Fig. 4** *Random amplification product B16-292*

Among the products of random-primed PCR with primer B16 (A) fragment B16-292 (arrow; enlarged in B) displayed significantly higher levels of fluorescence intensity in extracts of gravistimulated samples (20 min 90°; blue) as compared to unstimulated samples (green). This pattern was verified by several parallel experiments (C–D) and by gene-specific PCR (E) which provided an amplification product of the expected length that was detected as a 186/189 bp-double peak in capillary electrophoresis.

x-axis: fragment length in bp; y-axis: relative fluorescence intensity

**Nucleotide sequence of B16-292**

```
1    tggaacctgc cgaggtcacc cacggactgt agaaggttgg ggacggtagg tggtggtgga
61   acgcactgct atttgaatct tgcgctcttt tgctcttctt cagcggtcgt tctccggagg
121  tataggagac caaggagacg tgtactcgct tctcagccat agcgagtttg gcactgctat
181  ggcgatgaaa acagaagggt gcaagtcatc tgtttcctgt tcctgactct aaggagtgag
241  agggaagaag tgaaggaggg ggatctgtta ctatactggt aaactgctgt tgtagttggt
301  cacgatcatg gcgcactaca acaagtcgcc ttgggtgggg agggaggaga agggaaaatg
361  ggggggagtg ggagatttcc cctccatgcg aacgggtgag aagccgcggc cgatgggagg
421  tcgattttta cgctatcttc ctcggtgggt tgttcaatcg atcgtcgagc ggtctatggc
481  tgggaagatg ggttcgaagt ctgcccctgc tgccaagaag accggcttcc ataaagtaac
541  tctaggcatc tgcctcgtct tcgcaacgct gttcgtgatg agttactcgt cgtccccggc
601  ggtgactgcc tttctggaat ttctaacgtc tcctctgacg gaagtggcgg gaatttttgc
661  gacggctacg gaggcattcc gttcaatcag agctacatac gtggcgccgg taatgcaatc
721  cgttatcaat gtgctcatca tcgtgttcac cgtgcagtcg ttggacacga tgggcatgac
781  gctcatcttg ttttatctgt cattcaccgg ctggaggcct ccggttgtca ctcctatgaa
841  gcagccgcgt gcctcggatc cggaaaaccc gacgagcaag gcggagacga tttgcccccg
901  tgtgatgatc cagatcccga tgttcaacga gcgggagtgc tacaagatat cgatcggagc
961  gtgctcgcgg cttgattggc cgcgtgacaa gctggtcatc caggtgctgg acgactccaa
1021 taacgaggag atcaaggaga tggtgaagga ggaggtgagc agatggcagg cgcagggcgt
1081 taacatcgac taccgccaca gagtcgatcg gacggggtac aagggcgggt ctttgaagga
1141 aggcatgaag gcgccgtacg tcaaggagtg cgactttgtg gcggtgtttg acgccgattt
1201 ccagccaagg cctgactggc tgttgagaac ggtgccgtat ttcaaggacg atccgaagct
1261 cgctctcgtt cagacgcgct gggagtacag caaccaattc tgcaacctgc ttacgcgctt
1321 ccagttcatc aacacgtctt atcacttcca ggtggagcag caggtcatgg gagccactat
1381 gggctttttc ggtttcaacg gaactggcgg catctggaga atcgcagccg tgaacgaatg
1441 tggaggatgg gacgtgagga cgacggtcga agatatggac atcgctgtca gagctcacat
1501 ccacggtttg aagttcgtct atcttaatga cgtgcgtgtg ccttgcgagc tgcctcagac
1561 tctggaagcg tacacgcgtc agcagcacag atggcatgct gggccgatga acctgttccg
1621 gctgctgttc aagagaatct tgacgtctag ggccttgaca atgtggagca agttcaattt
1681 gatcgttctc ttcttctttg tcaggcgtct ccttgttccc acggtgaatt tcatgctttt
1741 cgttgtcctt ctccccctct ctctcttcgt ccccgaagcg aacatcccga tctgggtcac
1801 ctacacgttc cccatgttct tgtctttctt caggatgttg ctctgctcgt cgctgtttcc
1861 ttacatgttc ccttatctct tcttcgagaa cactatggtg atgacgaagc tgagcgccaa
1921 catccagggc ctgttccagt tcggacgagt gaatgaatgg atcgtcacgc agaaggtggg
1981 agcgttggcg aagcccggcg aggcagtcgc ttccaagaag aagaagtcca tcaagatctt
2041 caagagagag ctggccatgt ccgtgttcct tttgctagcg gcgattcaga gtctagcgat
2101 cgagaagggc atccacttct acatcttctt gttccaaggg ttgacattct tcgccttcgg
2161 atttgatctc ctcagcgacc atagctaatc aagaacgcac ctgtgctatt caattcatcc
2221 aattctatgt ttcctatttc atgattcgcg tcctcatcaa attagcagca gcacgcttgt
2281 gcatttacta acttcttaac ttgtcgagga gtagtatgcc cctgcctccc cccccaatcg
2341 ggtagtgaag tcagcgacgc gctacagtgg tcggtcgatc aggtgcgtgc tnccactttt
2401 cgctttcgct tttgcaggtt tccaacttcc tccagctttt tctttntatt atttgacccg
2461 ttatcctcac acgaatacta gatcattgat tgttttcgca attggtcggg gtgatgtcaa
2521 gtgatcaagc aagacgagag aatgggggtg aggatgatga tgaagatggg gctgatgatg
2581 ttctggaaac ctgccaaata tttgacactt cttaattctg gggctgacct tttacgctct
2641 tgtatgcgat ttgtccagta atcccatata acgaactcaa tatgggagtt tgttaattga
2701 ttattattat gtgcgccttt tgatgaggat aggtataata cccgacgatt atcacgccta
2761 ggcaagcggg tagaatgagg cgaatggcga ggctcgcttt ttcaagagag ggtacggtgt
2821 ttcccccatt ttcttcttct gtatcgttca tgaccgagtg gatgtgctct aatcaatgga
2881 gtgcccggaa tctgactatt gtttattctt ctgtttatcc aggacggtgt tcgggttctg
2941 ggattagctg ctaatagcta tgggaagcgg cgttgccgca tgattgatga tgggacacag
3001 gtatgttttg gtgggaatcg taaatggatt ggagatggac gcttctttcc tctccgattt
3061 ggaaatttga aggtttgcat attagtttaa tatcacctct gtgttcacga ataaaaaaaa
3121 aaaaaaa
```

**Amino acid sequence of B16-292**

```
1    MAHYNKSPWV GREEKGKWGG VGDFPSMRTG EKPRPMGGRF LRYLPRWVVQ SIVERSMAGK
61   MGSKSAPAAK KTGFHKVTLG ICLVFATLFV MSYSSSPAVT AFLEFLTSPL TEVAGIFATA
121  TEAFRSIRAT YVAPVMQSVI NVLIIVFTVQ SLDTMGMTLI LFYLSFTGWR PPVVTPMKQP
181  RASDPENPTS KAETICPRVM IQIPMFNERE CYKISIGACS RLDWPRDKLV IQVLDDSNNE
241  EIKEMVKEEV SRWQAQGVNI DYRHRVDRTG YKGGSLKEGM KAPYVKECDF VAVFDADFQP
301  RPDWLLRTVP YFKDDPKLAL VQTRWEYSNQ FCNLLTRFQF INTSYHFQVE QQVMGATMGF
361  FGFNGTGGIW RIAAVNECGG WDVRTTVEDM DIAVRAHIHG LKFVYLNDVR VPCELPQTLE
421  AYTRQQHRWH AGPMNLFRLL FKRILTSRAL TMWSKFNLIV LFFFVRRLLV PTVNFMLFVV
481  LLPLSLFVPE ANIPIWVTYT FPMFLSFFRM LLCSSLFPYM FPYLFFENTM VMTKLSANIQ
541  GLFQFGRVNE WIVTQKVGAL AKPGEAVASK KKKSIKIFKR ELAMSVFLLL AAIQSLAIEK
601  GIHFYIFLFQ GLTFFAFGFD LLSDHS
```

◄ **Fig. 5** *Nucleotide and amino acid sequence of B16-292*

The sequenced region of 3127 nts (acc. no. AY995817) comprises the complete coding region of the gene (highlighted in grey) with a length of 1878 nts. The corresponding protein with a length of 626 aa and the displayed amino acid sequence was clearly identified as a glucosyltransferase (see Table VII). The characteristic QXXRW-motif of glucosyltransferases is underlined.

The fluorescence intensity of B16-275 was low in unstimulated control samples but gradually increased in samples that were gravistimulated for 20 and 45 min pointing to a gradual up-regulation of the corresponding gene during gravistimulation (Fig. 6). The determined gene sequence comprised 650 nts but only a short part of the coding region (data not shown). BLASTX analysis displayed homology of this region with the 3'mRNA-end of a bovine reverse transcriptase-like protein (acc. no. CAA10770). However, since the level of homology was rather low (e-value 1e–08), the nature of the gene has to be determined by sequencing of the complete coding region. In addition, the differential expression of the gene during gravistimulation needs to be verified by gene-specific PCR.

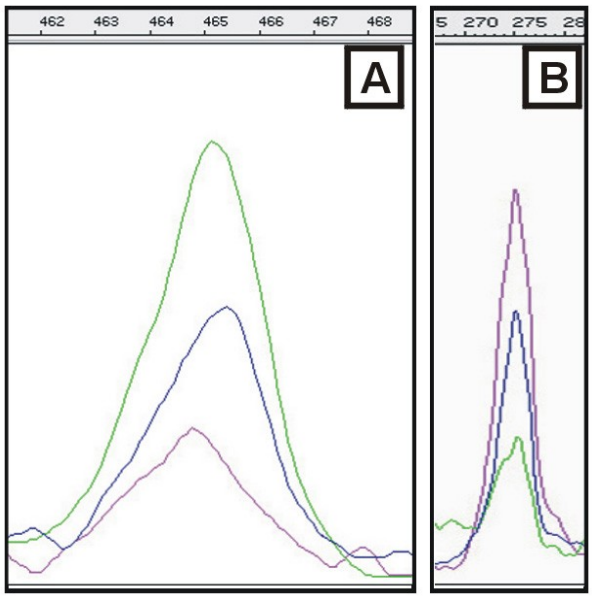


**Fig. 6** *Random amplification products B07-465 and B16-275*

Remarkable differences were detected in the fluorescence intensity of fragments B07-465 (A) and B16-275 (B) between extracts of unstimulated (green) and gravistimulated rhizoids that were horizontally positioned for 20 (blue) or 45 min (pink) prior to extraction. B07-465 points to a gradual down-regulation of the corresponding gene upon gravistimulation whereas B16-275 indicates gradual up-regulation.

x-axis: fragment length in bp; y-axis: relative fluorescence intensity

Two additional fragments exhibited distinct differences in the fluorescence signals after random-primed PCR but could not be sequenced. A gradual decrease in fluorescence intensity of B07-465 upon gravistimulation for 20 and 45 min indicates a reduction of the expression rate of the corresponding gene in gravistimulated samples (Fig. 6). After PCR amplification with random primer B10, the pattern and intensities of the fragments were almost identical in gravistimulated and unstimulated samples. Only B10-586 exhibited a distinct difference in

fluorescence intensity which was two-fold higher in gravistimulated rhizoids (20 min) than in unstimulated cells (Fig. 2).

### 3.1.4 Sequencing of abundant gene transcripts

Some of the pronounced fragments of random-primed PCR reactions indicating a high expression rate of the corresponding gene were isolated, and the coding regions were sequenced in order to expand the amount of genomic sequence information of characean algae.

Starting with the PCR fragment B05-273, 1027 nts of the corresponding gene were sequenced including the complete coding region of 399 nts or 133 aa (Fig. 7). The translated nucleotide sequence was aligned at full length and high levels of homolgy (e-value in the range of 1e–40) with ribosomal proteins of the L14 family (Table VIII). Additional partial alignments were confined to the C-terminal ends of various glycoproteins which have not been unequivocally classified and may represent additional members of the L14-family of proteins due to the high levels of homology. Based upon the alignment of B05-273 with L14-proteins of a very broad range of species, e.g. human L14-proteins (e-value < 5e–29), the gene was published in the genome database as *Chara globularis 60S ribosomal protein L14* with acc. nos. AY519976 and AAR99906 for nucleotide and amino acid sequence, respectively.

**Nucleotide sequence of B05-273**

```
1    tgctctttca cctccttctt ctttgctcac attgctcgcg cttctcttca tcgctcttcg
61   cttccgctgt cggtccctaa aaaaccaaaa tgccgttcag acgctttgtc aagattggga
121  ggatttgtct tgttaactat ggggagcact atggcaagct cgttgccata gttgacgtcg
181  tagatcaaaa tcgggcgctt gttgatgctc ccgacgtgac aaggcagcag atcagcttca
241  accggctgtc cttgacggac ttgaaggttg acatcttgcg gaatgccaag aaagacacac
301  tcaaggaggc atttgtaaag ggagaaacct accagaagtg ggcgagcagt gcttggggaa
361  ggaagcttga agtccggaag acgcgcgcag ctctaacgga ctttgacagg ttcaaggtca
421  tgactgctcg gatgaagagg agttctcttg tcaaaagaga actagccaag atgagaaaga
481  cgaaggcttg aaaacatgtg agtgggatga agacaaccgg catggcgttt gaagctgtca
541  ggaagagcaa atgaacggag cttcagcagt ggcgttttga tgatgagaga gcagatttga
601  taaagggtgg acgagttgag ttgttaaaga acggagtcag gaggggttct tccgtgagaa
661  aggggttgtg ggaatcgttt tttctctcag ccaaaggacc tgtcacttct tgtcatagca
721  caatgataga tcgcaggtca ttacggtttc aatgaggcaa tggtatatag ccggttgtag
781  cggtgttttg ccctccatga ggctctctat tgaaccatga gggctctcta ttgatagccg
841  tttctttcgt cgcgggctac ccatttgaca tttgatatcc gacgtctgat gtatcagttg
901  ctgctgtgtc gcttctggtc agtataaagg atcgtatttg atgttttcga gctaccagta
961  cattaaaagt tttgagaaac ggttttggtt ttcacaattc attgattcca taaaaaaaaa
1021aaaaaaa
```

**Amino acid sequence of B05-273**

```
1   MPFRRFVKIG RICLVNYGEH YGKLVAIVDV VDQNRALVDA PDVTRQQISF NRLSLTDLKV
61  DILRNAKKDT LKEAFVKGET YQKWASSAWG RKLEVRKTRA ALTDFDRFKV MTARMKRSSL
121 VKRELAKMRK TKA
```

**Fig. 7** *Nucleotide and amino acid sequence of B05-273*

A region of 1027 nts of the gene was sequenced (acc. no. AY519976) comprising the complete coding region (highlighted in grey) of 399 nts. The gene product with a length of 133 aa is a 60S ribosomal protein of the L14 family (see Table VIII).

The random fragment of PCR amplification B07-492 was identified to represent another ribosomal protein that was subsequently sequenced. The determined nucleotide sequence of 830 nts (Fig. 8) comprised the complete coding region of the gene (405 nts, 135 aa) which exhibited significant levels of homology (e-value 1e–47) with ribosomal proteins of the L27 family from various organisms (Table IX). The nucleotide (acc. no. AY682471) and amino acid (acc. no. AAT84169) sequences were published in the databases as *Chara globularis 60S ribosomal protein L27*.

In addition to the ribosomal proteins, the nucleotide sequence of the fragment B07-481 was determined. However, the corresponding gene could not be identified since no homology with database entries was observed by BLASTX alignment. Therefore, the complete coding region needs to be determined before the nature of the gene can be clarified.

**Nucleotide sequence of B07-492**

```
1   tctcttcgag ttgcggccac catagcctac cgtcaaatag ttgttgctgc gccttcctgc
61  gtcagcgaaa atggtgaagt ttttgaagca gaacaaggtg gtcgttttgc tgaacggtcg
121 ttatgcaggg cacaaagccg tgatcgtcaa gaatttcgat ggtggcacgg gcgggagacc
181 ttatggccac gccctggtgg cgggcatagc taagtacccc agaaaggtta cgaagaggct
241 gtctgagaag aagctcgcca agagggctag actcaagccg tttatcaagg tcatcaacta
301 caaccacatc atgccgacga ggtacgctct cgatgtggac ttgaagacca ccgtgatccc
361 ggagaagctt gaaactcagg cgaagaaggt ggagaccaga aaggaggtga agaagatcct
421 cgaggagagg ttcaagacag gaaagaacag atggtttttc tccaagttga gattctaggc
481 ttcgaaggac gtcagggtgt gccggagaag ttttgaagtt taagtcgcgc agaatttgat
541 aacccttttcg gttgtagggg tcaggtattg ggaaagtggc tcgcaaggtc gtaaccattc
601 cgtatggata cggtggtcat acaagataag atatctgttg tgcaagctct ttgcgatgta
661 ttttgagttg tcctccgtga atcgagtctt atgagtgaca agaaccggca tattgggtga
721 catgaacggg aggaactttt gctttgaatg aagcaagcat gcaatttatc gcgttgtacg
781 ccgtgaatgg agtgtaatgg atgataagaa ccggcaaaaa aaaaaaaaaa
```

**Amino acid sequence of B07-492**

```
1   MVKFLKQNKV VVLLNGRYAG HKAVIVKNFD GGTGGRPYGH ALVAGIAKYP RKVTKRLSEK
61  KLAKRARLKP FIKVINYNHI MPTRYALDVD LKTTVIPEKL ETQAKKVETR KEVKKILEER
121 FKTGKNRWFF SKLRF
```

**Fig. 8** *Nucleotide and amino acid sequence of B07-492*

The sequence of 830 nts (acc. no. AY682471) comprises the complete coding region (highlighted in grey) with a length of 405 nucleotides. The 135 aa-sequence of the corresponding protein which was identified as a 60S ribosomal protein of the L27 family (see Table IX) is displayed.

### 3.1.5 Partial sequencing of a class XI myosin from *Chara globularis*

Myosins represent a class of motor proteins that are crucial for gravitropic tip growth of characean rhizoids and protonemata because they regulate fundamental processes such as vesicle transport and positioning of statoliths. Based upon the published sequence of a class XI myosin heavy chain from the closely related species *C. corallina* (CCM, acc. no. AB007459; Kashiyama et al. 2000) the corresponding homolog from rhizoids of *C. globularis* was partially sequenced.

Determination of the nucleotide sequence of the *C. globularis* myosin was started with the amplification of a fragment of the CCM-tail using primers that were specific for the nucleotide sequence of CCM. The poor conservation of the tail domain among the myosin class of proteins ensured that the class XI myosin was specifically amplified but no additional myosins. The amplification product of the *C. globularis* myosin was isolated, cloned and sequenced. Determination of the nucleotide sequence of the mRNA was subsequently extended by 5'RACE-PCR. An overall region of 1383 nts was sequenced (Fig. 9) that comprised parts of the coiled-coil domain and the head domain and six IQ motives of the neck domain as revealed by protein alignment with CCM (Fig. 10). The level of homology between the amino acid sequences of the myosin from *C. globularis* rhizoids and CCM was very high

(e-value 1e–157), which underlines the high degree of similarity between these proteins from the closely related species.

**Partial nucleotide sequence of a *C. globularis* class XI myosin**

```
1    tggagaaatg caacctcaag ggccgtcaga ttggcaagac aaaagtgtcc ctgcgggcag
61   ggcagatggc tattctggat acgaagaggt caaacgtgct caataaggct gcagtcaaga
121  tccagcacat ggtgcagact ttcctgatgc ggagagacta cgagaggatg aagaatgcgt
181  cactattggt gcaggcatac tggagaggga caatggcaag actggagttc agattcctcc
241  aggagcaggt ctcagctgtt tgcttccaaa ggtatatccg tggatacctt acacagaaga
301  attacctcga gatgcggcaa gctgctatca ggattcaatc cgctgtcagg tctcttgctg
361  catggagggt tcttcgtact ttgaaagaca accattctgc cactcagatt cagtcgaaat
421  ggcgcagcta tgttgaattc aggagctaca atgagctgtt gaggtcatgt atagtcttcc
481  aaggtgcctg gcgaggcaag gaggcacgaa gcgagctcaa gaagcttcga caggctgccc
541  gtgaaactgg tgctttgcgt gaggcaaagg acaggctggc gaagaagtgt gaggagctca
601  cattgcgtct tgggctggca aaggtgagcc ttattgcaag gaacagcgag ctggccaaaa
661  agcagtcagc gatggaggag gtgcaggcac aagtggagca aatgaaggtg ttattggcga
721  aggagcgtga ggcacatgag gcaagcttag ctcaggcaaa ggccgctgcg gctcagcgtt
781  tggatgcgga catgtctgca cagccttcca aagaggtcct ggatagaatc gaggctttga
841  gtgaggagaa catgaaactc aaggaacttg tcgaagacta tgagaagaag aaggcactgg
901  cagagagttc tgcaaaaagg atagaggagg aggcagacct gaagcatgat actatgcaga
961  aatcattggg cagagcggag gaacaggttc agaatttgat atcagagaac cagagcctgc
1021 aatccgagaa agagaattta caatcagaga atcgggtttt gagacagcag gcattgagca
1081 tgaaagatct ggagacgaag aaccaggcca agctgaacca gttagaagac aacagccaag
1141 ctctgaaagc tgagaaccag acactcagac aacagctcga acagctgatt tcaaacgctc
1201 cgatcaagcc cacgccggag cctgtgatta cagtctatcc agatgtgcag cgaatcaagc
1261 ccacgacgga gcctgtgatt acaacctatc cagatgccca gccagagaaa tcccatgata
1321 ttcggacaga gcgcagtgac tccaagagat tggagaaatc ccaacatatt cggagtgaga
1381 gca
```

**Translated amino acid sequence of the partial myosin nucleotide sequence**

```
1    EKCNLKGRQI GKTKVSLRAG QMAILDTKRS NVLNKAAVKI QHMVQTFLMR RDYERMKNAS
61   LLVQAYWRGT MARLEFRFLQ EQVSAVCFQR YIRGYLTQKN YLEMRQAAIR IQSAVRSLAA
121  WRVLRTLKDN HSATQIQSKW RSYVEFRSYN ELLRSCIVFQ GAWRGKEARS ELKKLRQAAR
181  ETGALREAKD RLAKKCEELT LRLGLAKVSL IARNSELAKK QSAMEEVQAQ VEQMKVLLAK
241  EREAHEASLA QAKAAAAQRL DADMSAQPSK EVLDRIEALS EENMKLKELV EDYEKKKALA
301  ESSAKRIEEE ADLKHDTMQK SLGRAEEQVQ NLISENQSLQ SEKENLQSEN RVLRQQALSM
361  KDLETKNQAK LNQLEDNSQA LKAENQTLRQ QLEQLISNAP IKPTPEPVIT VYPDVQRIKP
421  TTEPVITTYP DAQPEKSHDI RTERSDSKRL EKSQHIRSES
```

**Fig. 9** *Partial nucleotide sequence and translated amino acid sequence of C. globularis myosin*

The partial myosin sequence comprises 1383 nts and exhibits a very high level of homology with the sequence of CCM. Within the translated amino acid sequence (reading frame +3) characteristic myosin domains were identified (see Fig. 10): i) the C-terminal part of the CCM head domain (underlined with full line); ii) six IQ motifs (highlighted in grey); iii) a part of the coiled-coil region of CCM (underlined with dashed line).

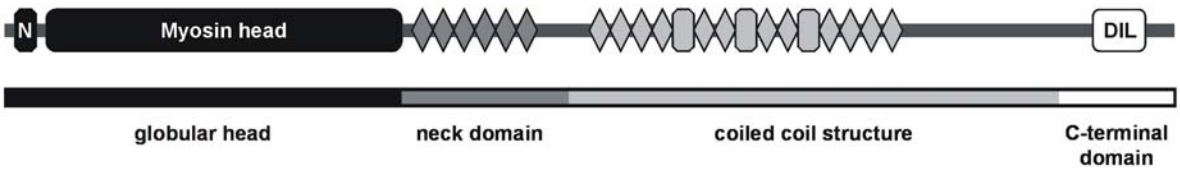


**Fig. 10** *Molecular structure of CCM*

The class XI myosin that was isolated from *C. corallina* (Kashiyama et al. 2000) comprises different structural and functional domains. The N-terminal myosin head includes the highly conserved ATP-binding site. The neck domain is composed of six IQ motifs (dark grey rhombs). The coiled-coil structure is characterized by conserved tandem-repeats (light grey rhombs) and interrupted by coiled-coil breaking motifs (light grey boxes).

N: N-terminal domain; DIL: non α-helical C-terminal tail domain. Figure modified after Kashiyama et al. (2000).

## 3.2 Early mechanisms of gravity sensing studied under microgravity conditions

Microgravity experiments were performed during parabolic flights of the ESA MAXUS-5 sounding rocket and of the Airbus A300 Zero-G to specify basic molecular principles and mechanisms underlying the early phase of gravity sensing in characean rhizoids and protonemata. The MAXUS-5 experiment was designed to define the forces of molecular interaction between statoliths and the actin cytoskeleton which restrict statolith sedimentation and gravity susception by determining the threshold acceleration level required for lateral displacement of statoliths. The parabolic plane flight experiments were intended to characterize the statolith-dependent mechanism of gravireceptor activation eliciting gravitropic signaling at the graviperception sites of the plasma membrane in rhizoids. Comprehensive ground control experiments underlined that the parabolic flight profile with alternating hyper- and microgravity phases was excellently suited to investigate if sedimented, but weightless statoliths were capable of activating the gravireceptor molecules. The results of the MAXUS-5 experiment and of the parabolic plane flight experiments were published recently (Limbach et al. 2005).

### 3.2.1 The threshold acceleration level required for lateral statolith displacement

Vertically downward growing rhizoids and protonemata were subjected to lateral centrifugation during the microgravity phase of the MAXUS-5 sounding rocket flight.

Analyses of digital images taken from samples that were fixed at the end of the microgravity phase revealed that centrifugation with 0.25*g* and 0.14*g* were sufficient to induce lateral displacement of statoliths in rhizoids (Fig. 11B, C). Several statoliths were sedimented onto the centrifugal cell flank, whereas no statoliths were found to be present at the centripetal plasma membrane (Fig. 11B, C). At an acceleration level of 0.05*g* no redistribution of statoliths was observed (Fig. 11A), and the shape of the statolith complex was similar to those of normal vertically growing cells on ground. Chemically fixed samples of protonemata could not be analyzed because the cells were in bad condition during the parabolic flight as indicated by bulging of the tip.

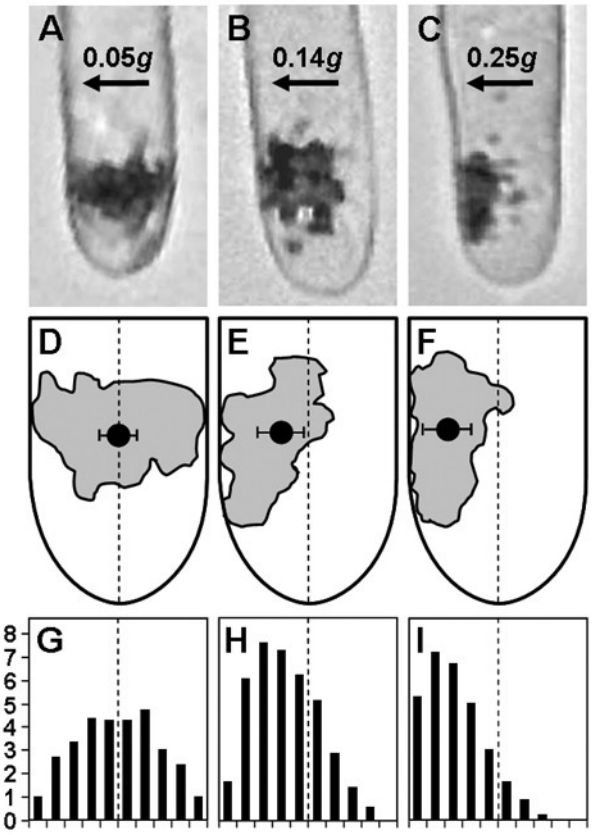


**Fig. 11** *Final statolith position in chemically fixed rhizoids after lateral centrifugation in microgravity*

The figure shows the position of statoliths in chemically fixed rhizoids which were laterally centrifuged with 0.05*g* (A, D, G), 0.14*g* (B, E, H) or 0.25*g* (C, F, I) for 13 min during the microgravity phase of the MAXUS-5 sounding rocket flight. Centrifugation with 0.25*g* and 0.14*g*, but not 0.05*g*, induced a displacement of statoliths and settlement of some statoliths onto the centrifugal cell flank.

A–C: Micrographs showing the position of statoliths in representative samples of each acceleration level.

D–F: Geometrical centers of the statolith complexes (filled circles represent means ± SE in lateral direction, $n \geq 4$). The shape of the statolith complex in one representative rhizoid of each acceleration level (rhizoids are different from those displayed in A–C) is shown in grey.

G–I: Distribution of statolith frequency across the cell diameter ($n \geq 4$).

Arrows indicate the direction of centrifugal forces. Dashed lines represent median axes of the cells. The diameter of rhizoids is 30 µm.

The distribution of statolith frequency across the cell diameter in the three sets of chemically fixed rhizoids is shown in Fig. 11G–I. Whereas the majority of statoliths was displaced into the centrifugal half of the cells after lateral acceleration with 0.14*g* and 0.25*g* (Fig. 11H, I), statoliths were still symmetrically arranged across the cell diameter after centrifugation at 0.05*g* (Fig. 11G). Accordingly, the geometrical center of the statolith complex in 0.14*g* and 0.25*g* samples, but not in 0.05*g* samples, was shifted from a position around the median axis of the cells (Fig. 11, dashed line), the normal position in downward growing cells, in the direction of the acceleration stimulus (Fig. 11D–F).

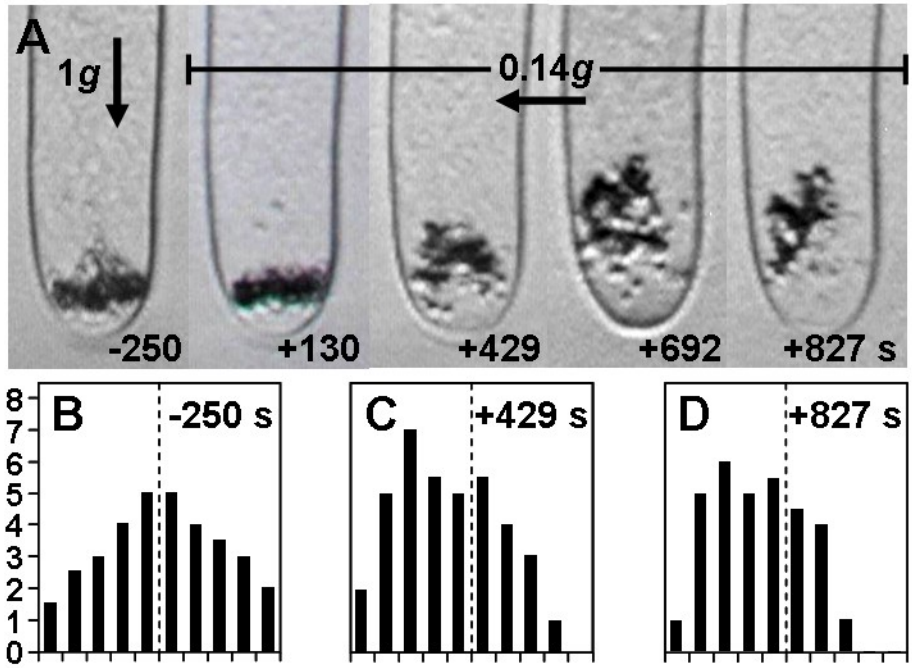


**Fig. 12** *Statolith distribution in rhizoids during lateral centrifugation in microgravity*

The distribution of statoliths was observed in characean rhizoids by in-vivo video microscopy before lift-off (–250 s) of the MAXUS-5 sounding rocket and during lateral centrifugation at 0.14*g* in microgravity (indicated in s after lift-off).

A: Series of micrographs of a representative rhizoid exhibiting symmetrical distribution of statoliths across the cell diameter before lift-off. Centrifugal displacement of statoliths caused by the 0.14*g* acceleration in microgravity was first detectable at +429 s. Individual statoliths settled onto the cell flank towards the end of the microgravity phase (+692 s and +827 s). Arrows indicate the direction of gravitational and centrifugal forces. The diameter of the rhizoid is 30 µm.

B–D: Average distribution of statolith frequency across the cell diameter of 4 rhizoids at indicated times of the rocket flight demonstrating that statoliths were displaced from a symmetrical arrangement before lift-off (B) to an asymmetrical distribution during lateral centrifugation (C–D).

Video-microscopic recording allowed tracking of statoliths in four rhizoids during lateral centrifugation at 0.14*g* under microgravity conditions of the MAXUS-5 sounding rocket flight. A representative example of statolith redistribution induced by 0.14*g* is shown in Fig. 12. Statoliths were symmetrically distributed across the cell diameter of the rhizoid before lift-off (Fig. 12, t = –250 s) and shortly after the onset of centrifugation in microgravity (Fig. 12A; t = +130 s). The statolith complex appeared slightly more condensed due to the launch accelerations with peaks of up to 12.8*g* in apical direction. During continued lateral acceleration statoliths were gradually displaced towards the centrifugal flank (Fig. 12, t = +429 s, +692 s, +827 s). Sporadically, some statoliths settled onto the gravisensitive plasma membrane of the centrifugal flank (Fig. 12, t = +692 s); however, settlement was only transient since the statolith position was not only influenced by centrifugation but also by

actomyosin-dependent transport mechanisms. A few individual statoliths were sometimes even observed near the centripetal plasma membrane (Fig. 12, t = +692 s). The image sequence in Fig. 12A represents snapshots of the dynamically changing statolith position and is therefore suited to demonstrate the displacement of statoliths towards the centrifugal flank, but the images do not provide clear evidence for the centrifugation-induced settlement of statoliths onto the lateral plasma membrane, which was distinctly visible in chemically fixed samples (Fig. 11B). Nevertheless, microscopic analyses of living rhizoids after retrieval of the payload have shown that lateral acceleration of 0.14*g* for 13 min resulted in curvatures angles of 5 to 9 degrees (Fig. 13; n = 4), whereas centrifugation with 0.05*g* did not provoke any curvature response.


**Fig. 13** *Curvature responses of rhizoids that were laterally centrifuged in microgravity*

The micrograph which was recorded in the ground lab after early retrieval of the MAXUS-5 payload shows two rhizoids from observation cuvettes that were centrifuged at 0.14*g* during the microgravity phase of the rocket flight. The cells exhibited four distinct curvatures (1–4) that could be clearly attributed to oppositely oriented stimuli during and after the rocket flight. The first curvature response (1) with angles of 7 – 9° was elicited by lateral centrifugation of the vertically oriented cells in microgravity. Before early retrieval of the payload, rhizoids were gravistimulated in the opposite direction as compared to the centrifugation stimulus and cells responded with a second curvature reaction (2). Reorientation of the samples during payload retrieval and in the ground lab is reflected by curvature responses 3 and 4. The diameter of rhizoids is 30 µm.

It can be concluded that sporadic contact of statoliths with the centrifugal plasma membrane was sufficient to initiate the gravitropic signalling pathway. Whereas the rhizoids that were observed by video microscopy grew at constant rates of 60 – 100 µm $min^{-1}$ before, during and after the parabolic flight, growth rates of protonemata were remarkably lower (20 – 40 µm $min^{-1}$) and decreased gradually during the experiment indicating the suboptimal conditions of the cells. However, a gradual statolith displacement towards the centrifugal cell flank during

lateral centrifugation at 0.14*g* was also detected in protonemata although the effect was less pronounced than in rhizoids (data not shown).

In addition to the lateral shift of the statolith position, a basipetal displacement of statoliths during the microgravity phase was observed (Fig. 12A). This effect has already been described earlier and is attributed to net-basipetally acting actomyosin forces which are no longer compensated by the gravity force (Braun et al. 2002). Under normal 1*g*-conditions, both forces work in concert to keep statoliths in a dynamically stable position of balance.

### 3.2.2 Functional characterization of gravireceptor activation in rhizoids

#### 3.2.2.1 Effects of increasing the weight of sedimented statoliths on the gravitropic curvature response

Ground control experiments were performed to test the impact of the sequence of hypergravity accelerations as they occur during parabolic flights on the gravitropic response of characean rhizoids. The profile of hypergravity phases was mimicked by centrifuging rhizoids 62 times for 22 s at 2*g* during an overall gravistimulation time of 120 min. The centrifugation stimuli were applied in the direction of the gravistimulus after rhizoids had been placed horizontally for 10 min. Thus, by increasing the weight of fully sedimented statoliths, centrifugation enhanced the mechanical pressure on the plasma membrane of the subapical lateral cell flank, but did not accelerate the statolith sedimentation process. Intermittently centrifuged rhizoids exhibited a mean curvature angle of 45.03° (± 8.18), which was in the same range as the curvature angle of control samples (44.62° ± 11.00) that were gravistimulated for 120 min under continuous 1*g* conditions (student´s t-test, P = 0.8136; Fig. 14). These results demonstrate that the graviresponse was not promoted by increasing the pressure of sedimented statoliths on putative gravireceptor molecules located in the plasma membrane.

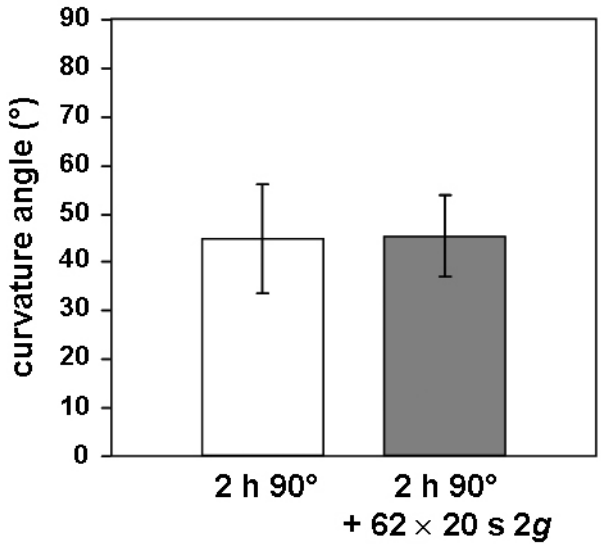


**Fig. 14** *Effect of intermittent centrifugation of gravistimulated rhizoids on gravitropic curvature*
The graph displays the curvature angles of control cells which were continuously gravistimulated for 120 min at 90° on ground (white bar; n = 69) and of rhizoids which were horizontally positioned for 120 min on ground and intermittently centrifuged 62 times for 22 s at 2*g* (grey bar; n = 59). Not significantly different curvature values of controls and centrifuged samples (student´s t-test, P = 0.8136) provide evidence that increasing the weight of sedimented statoliths by repeated short-term centrifugation does not affect gravitropic curvature. Data represent means ± SE.

Similarly, when rhizoids were pre-stimulated by tilting them for 10 min by 90° at 1*g* followed by stimulation at 1*g*, 2*g*, 3*g*, 4*g* or 5*g* for 15 min, the mean curvature angles were all in the same range of 23.09° (± 5.33), 24.73° (± 6.62), 24.64° (± 5.68), 23.71° (± 4.61) and 25.92° (± 4.65), respectively (pairwise student´s t-test, P > 0.05; Fig. 15). No tendency was recognizable towards reduced or enhanced curvatures angles that might have been caused by increasing the weight of sedimented statoliths by centrifugation. As mentioned above, pre-stimulation of all cells at 1*g* warranted that the statoliths sedimented onto the lateral cell flank under the same conditions, so that the graviresponse started at the same time in all samples.

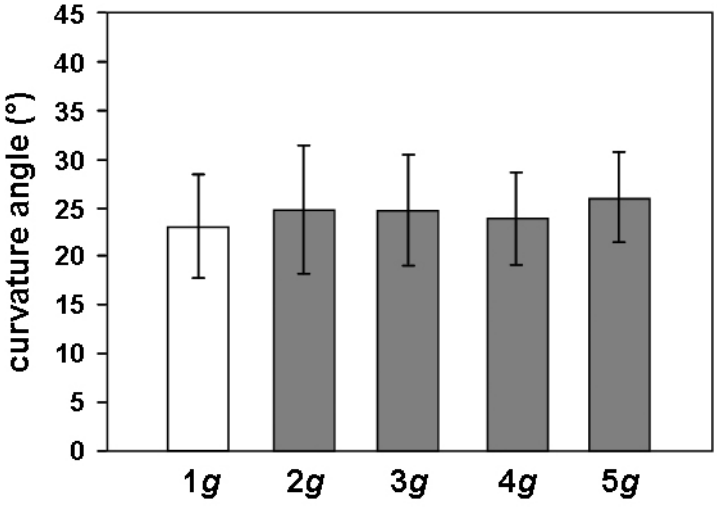


**Fig. 15** *Effects of hyper-g centrifugation on gravitropic curvature of rhizoids*
Curvature angles of rhizoids were analyzed after 10 min pre-stimulation at 90° on ground and subsequent stimulation at 1*g*, 2*g*, 3*g*, 4*g*, or 5*g* for 15 min in the direction of the initial gravistimulus. 1*g*-controls (white bar) and centrifuged samples (grey bars) exhibited curvature angles that were all in the same range as revealed by pairwise student´s t-test (P > 0.05). The results indicate that enhanced pressure on the gravisensitive site of the plasma membrane due to an increased weight of statoliths had no impact on gravitropic curvature. Data represent means ± SE (n ≥ 11).

#### 3.2.2.2 Effects of short-term removal of statoliths from the plasma membrane on the gravitropic curvature response

The parabolic plane flight profile provides 31 short microgravity phases within a flight time of approximately 120 min. In order to evaluate if 22 s – the duration of each of the microgravity phases – would be sufficient to interrupt gravity perception and to alter the gravitropic response, comprehensive inversion experiments were performed on ground. Rhizoids were pre-stimulated for 10 min by 90° and subsequently inverted 31 times from 90° to 270° within 120 min according to the sequence of the microgravity phases during parabolic flights. The intermittent removal of statoliths by inverting cells for 30 s, 22 s and 10 s resulted in significantly reduced curvature angles as compared to the corresponding control samples that were continuously gravistimulated (student´s t-test, $P < 0.01$; Fig. 16; Table III). Reduction of curvature was strongest when rhizoids were inverted for 30 s (–28.59%). This effect decreased but was still significant when the inversion intervals were reduced to 22 s (–15.59% to –19.76%) and 10 s (–13.03% to –20.10%). When rhizoids were inverted 31 times for only 5 s, curvature angles were no longer significantly different from those of continuously gravistimulated control cells (student´s t-test, $P > 0.05$; Fig. 16; Table III). In addition, the gravitropic curvature of rhizoids which were intermittently inverted 31 times for 22 s within 120 min was similar as compared to those which were continuously gravistimulated for only 109 min matching the total gravistimulation time of 120 min reduced by the total inversion time of 31 × 22 s (data not shown). For inversions and controls of each experiment set rhizoids of the same age growing under identical conditions were used. The variation in the curvature angles between the different experiment sets (Table III) can be attributed to different growth conditions, e.g. temperature and seasonal conditions.

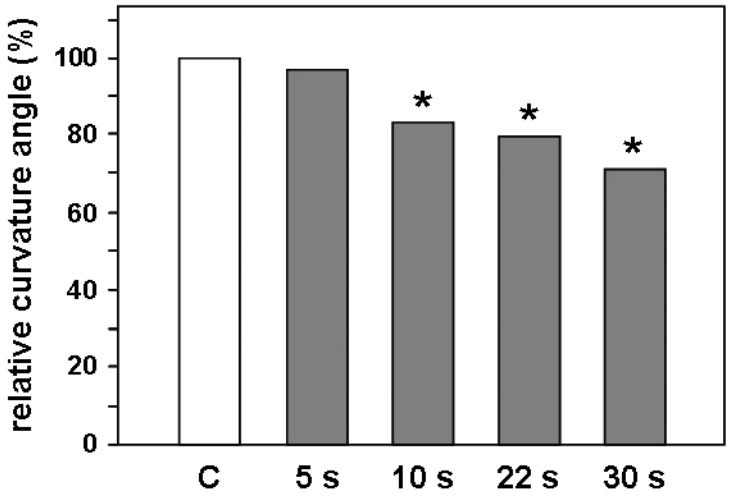

◄ **Fig. 16** *Effects of short-term removal of sedimented statoliths from the plasma membrane on gravitropic curvature of rhizoids*

The graph displays mean curvature angles of rhizoids which were pre-stimulated on ground for 10 min at 90° and subsequently inverted 31 times to 270° (grey bars) relative to the mean curvature angles of the corresponding control samples which were set to 100 percent (C; represented by the white bar). Rhizoids were repeatedly inverted for 5 s, 10 s, 22 s or 30 s during a total experiment duration of 120 min whereas control samples were stimulated at 90° for 120 min under continuous 1*g*-conditions. Significantly reduced curvature angles of the inverted samples (student´s t-test, $P < 0.01$; indicated by an asterisk) were observed when the duration of the inversion phases was longer than 5 s ($n \geq 44$ for each sample). The complete data of all inversion experiments including the absolute curvature values are summarized in Table III.

**Table III** *Rhizoid curvature angles of intermittently inverted rhizoids and continuously gravistimulated control cells on ground*

Inversion profiles are described by the duration of a single inversion phase and by the total duration of 31 inversion events listed as absolute value and as percentage of the total experiment duration of 120 min. Control rhizoids were continuously gravistimulated for 120 min at 90°. Values of maximally achieved curvature angles are means ± SE. The number of cells measured (n) is shown in parentheses. Differences between mean curvature angles of inverted cells and the corresponding control cells are shown in percent. For description of experiment see Fig. 16.

| Exp. No. | Inversion profile | | | Curvature angle (°) | | Difference |
|---|---|---|---|---|---|---|
| | Single s | Total min | Total % | Control cells | Inverted cells | % |
| 1 | 5 | 2.6 | 2.15 | 37.44 ± 8.94 (45) | 36.23 ± 8.23 (44) | – 3.25 |
| 2 | | | | 38.87 ± 8.78 (69) | 36.14 ± 7.23 (63) | – 7.02 |
| 3 | | | | 42.89 ± 6.02 (61) | 44.81 ± 7.37 (53) | + 4.49 |
| 4 | 10 | 5.2 | 4.31 | 61.40 ± 8.63 (40) | 53.40 ± 15.00 (25)[a] | – 13.03 |
| 5 | | | | 39.31 ± 9.36 (55) | 31.41 ± 8.87 (49)[a] | – 20.10 |
| 6 | | | | 42.89 ± 6.02 (61) | 35.74 ± 7.99 (57)[a] | – 16.67 |
| 7 | | | | 49.72 ± 10.68 (46) | 41.97 ± 9.63 (34)[a] | – 15.58 |
| 8 | 22 | 10.3 | 8.61 | 48.38 ± 9.60 (50) | 38.82 ± 11.50 (44)[a] | – 19.76 |
| 9 | | | | 66.23 ± 4.82 (13) | 55.90 ± 6.30 (21)[a] | – 15.59 |
| 10 | 30 | 15.5 | 12.92 | 59.11 ± 11.37 (104) | 42.21 ± 10.24 (77)[a] | – 28.59 |

[a] Curvature angles of inverted and control cells were significantly different (student´s t-test, $P < 0.01$)

During inversion of gravistimulated rhizoids, movements of statoliths that were initially sedimented on the plasma membrane were tracked by high-magnification video microscopy in order to analyze the time course of statolith sedimentation away from the upper gravisensitive plasma membrane. After 2 s of inversion, individual statoliths had already lost contact with the plasma membrane and 5 s after inversion, the statoliths were found at a mean

distance of approximately 0.5 µm (Fig. 17) indicating that the inversion intervals of the above described experiments were sufficient to remove statoliths from the plasma membrane. Thus, the inversion experiments demonstrate that gravity perception and the graviresponse are terminated very quickly as soon as the contact of statoliths with the gravisensitive plasma membrane is interrupted.

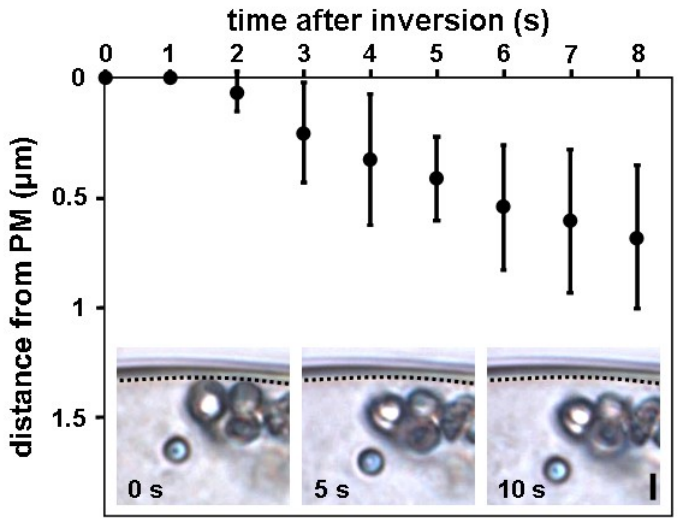


**Fig. 17** *Displacement of statoliths after inversion of gravistimulated rhizoids*

The graph shows the mean distances (± SE, n = 18) of statoliths from the upper cell flank at the indicated times after inversion of gravistimulated rhizoids from 90° to 270° on ground. Only those statoliths were selected for the measurements that were regarded as fully sedimented on the plasma membrane (PM) after 10 min of gravistimulation at 90°. A dashed line was drawn as reference line to indicate the position of the sedimented statoliths on the upper plasma membrane and the subsequent measurements of the distances were referred to this line. The series of micrographs shows that all statoliths have sedimented away from the upper plasma membrane already 5 s after inverting the representative rhizoid. The bar represents 1 µm.

#### 3.2.2.3 Effects of short-term weightlessness of sedimented statoliths on the gravitropic curvature response

During the 36$^{th}$ ESA and the 6$^{th}$ DLR parabolic flight campaigns, all in-flight control samples in the onboard centrifuge and flight samples were tilted by 90° 10 min prior to the first parabola. This ensured that the statoliths were properly sedimented on the lateral cell flank in all samples so that the following hypergravity and microgravity phases acted on sedimented statoliths. Immediately after the last parabola, all samples were tilted back into the original

orientation. Since the above mentioned centrifugation experiments have shown that short hypergravity phases do not affect the graviresponse, the comparison of the maximally achieved curvature angles of flight samples and in-flight controls should provide information, whether sedimented statoliths, which are weightless but still sedimented on the lower plasma membrane during the short microgravity phases, are able to activate the gravireceptor or not. Initially, during the 36th ESA campaign, ground control samples were continuously gravistimulated at 1*g* conditions for the same time as the flight samples. But since it was not feasible to provide the same environmental conditions, temperature gradients and vibrations as for the flight samples, these controls were not regarded as proper controls. In-flight control samples, which were centrifuged at 1*g* during the microgravity phases, however, experienced the same conditions as flight samples and, therefore, represent the adequate reference system.

Analyzing the statolith position in gravistimulated Chara rhizoids, which were observed by video microscopy during the different flight phases, revealed that the shape of the sedimented statolith complex remained unchanged and that statoliths were not lifted from the plasma membrane during the short-term microgravity conditions (data not shown).

On five out of six flight days, all 31 parabolas were flown in a consecutive sequence providing a total of 11.4 min microgravity, which is in a range of 7.73% to 9.88% of the total experiment duration time (Table IV).

**Table IV** *Rhizoid curvature angles of flight samples and in-flight controls of parabolic plane flight experiments*

All samples were horizontally positioned for the indicated experiment duration time of seven parabolic plane flights. In-flight control samples were laterally centrifuged at 1*g* during the microgravity phases. The total duration of all 22 s-microgravity phases of each flight is listed as absolute value and as percentage of the experiment duration time. Values of maximally achieved curvature angles are means ± SE. The number of cells measured (n) is shown in parentheses. Differences between mean curvature angles of flight samples and the corresponding in-flight controls (shown in percent) were non-significant (student´s t-test, $P > 0.05$). For details of experiment setup see Fig. 18.

| Flight No. | Exp. duration | µg time | | Curvature angle (°) | | Difference |
|---|---|---|---|---|---|---|
| | | Total | Total | Control cells | Flight cells | |
| | *min* | *min* | *%* | | | *%* |
| 1 | 121 | 11.4 | 9.39 | 46.76 ± 10.67(62) | 46.65 ± 14.13 (115) | – 0.23 |
| 2-A | 84 | 6.6 | 7.86 | 40.55 ± 8.69 (67) | 40.44 ± 10.69 (118) | – 0.28 |
| 2-B | 59 | 4.8 | 8.08 | 36.64 ± 10.20 (80) | 35.78 ± 7.95 (95) | – 2.34 |
| 3 | 125 | 11.4 | 9.09 | 47.39 ± 9.27 (121) | 47.22 ± 9.17 (138) | – 0.36 |
| 4 | 147 | 11.4 | 7.73 | 50.82 ± 7.53 (38) | 51.21 ± 7.28 (74) | + 0.77 |
| 5 | 146 | 11.4 | 7.79 | 51.69 ± 7.73 (81) | 49.53 ± 7.49 (32) | – 4.18 |
| 6 | 115 | 11.4 | 9.88 | 53.12 ± 7.68 (58) | 52.18 ± 8.01 (38) | – 1.76 |

On one flight day, the A300 Zero-G aircraft flew only 18 parabolas in 84 min, followed by 13 parabolas in 59 min providing microgravity portions of 7.86% and 8.08%, respectively (Table IV). In all cases, the curvatures angles of the flight samples (n = 32 – 138 per flight) and the corresponding in-flight controls (n = 38 – 121 per flight) were almost identical, and minor differences were not significant (student's t-test, P > 0.05; Fig. 18; Table IV). Even the highest deviations of curvature angles from flight samples and in-flight controls of –1.76% to –4.18% were still small considering the corresponding portions of total microgravity time (7.79% to 9.88%; Table IV) and compared to the reduction of curvature after intermittent inversion for 10 s and 22 s (–13.03% to –20.10%; Table III). The results of the parabolic flight experiments demonstrate that weightless statoliths, which are still present at the gravipeception site, but do not exert any pressure, are capable of activating the gravireceptor which triggers gravity-perception and the graviresponse during the microgravity phases as during the hypergravity phases and at 1*g*.

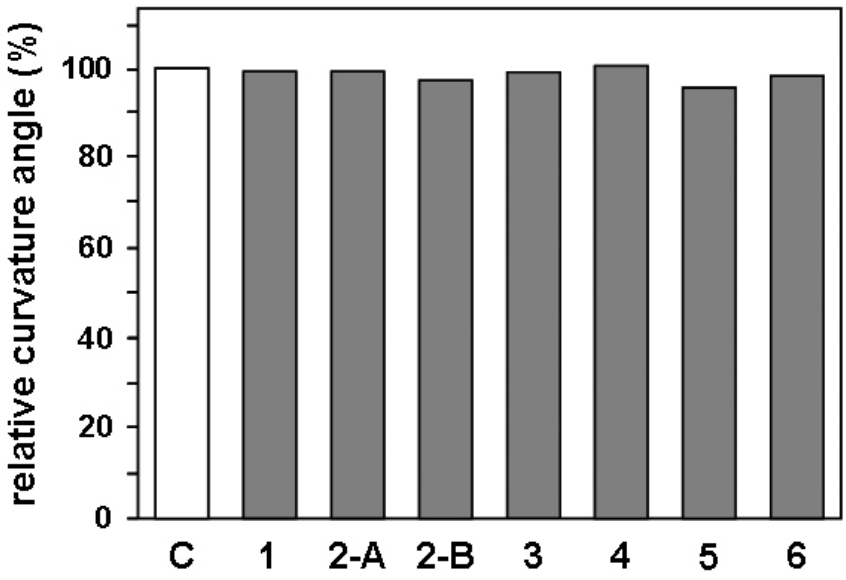


**Fig. 18** *Effects of short-term weightlessness of sedimented statoliths on gravitropic curvature of rhizoids*

The graph shows mean curvature angles of flight samples (grey bars) relative to the mean curvature angles of the corresponding in-flight control samples which were set to 100 percent (C; represented by the white bar). The experiments were conducted during the 36th ESA (samples No. 1–3) and during the 6th DLR parabolic flight campaign (No. 4–6). On flight day No. 2, two flights with reduced flight profiles were conducted (No. 2–A and 2–B; for details of flight profiles see Table IV). All samples were tilted into a horizontal position 10 min prior to the first parabola and tilted back after the last parabola of the flight profile. In-flight control samples were laterally centrifuged at 1*g* during the microgravity phases. No significant differences in curvature angles were observed between flight samples and in-flight controls on any of the flights (student´s t-test, P > 0.05; n ≥ 32 for each sample) indicating that graviperception was not interrupted when statoliths became weightless during microgravity. For complete data and absolute curvature values of all flight experiments see Table IV.

## 3.3 Electron microscopy of cryofixed characean rhizoids

Since chemical fixation causes some serious artifacts and limits the level of resolution of electron microscopic research, protocols for the preparation of samples using high-pressure freeze fixation and freeze substitution of characean rhizoids were developed in this study. Cryofixation technology was combined with innovative 3D dual-axis electron tomography as imaging technique for high-resolution ultrastructural analysis of the apical cell region and provided new insights into the structural and functional organization of tip growth. The improved preservation of protein conformation in high-pressure frozen samples allowed to establish a reliable immunogold labeling protocol for the specific localization of cellular proteins.

### 3.3.1 High-pressure freeze fixation, freeze substitution and electron tomography

The parameters of high-pressure freeze fixation and freeze substitution were optimized for the preparation of electron microscopic samples of characean rhizoids leading to the final protocols denoted under 2.10.1 and 2.10.2. Although squeezing of the large multicellular thallus pieces was inevitable when putting together the freezing hats, most rhizoids were not affected by mechanical damage since they usually extended into free space of the freezing chambers. Nevertheless, the rhizoids from one node exhibited large differences in freezing quality due to slight gradients in the freezing conditions (e.g. cooling rate and pressure value) across the volume of the freezing chamber. Therefore, preparation of a high number of samples was required (approx. 300 nodes with attached rhizoid bundles) to obtain several rhizoids exhibiting an optimum freezing quality and ultrastructural preservation.

Cryoprotectants were used for freeze fixation to avoid the formation of cytoplasmic ice crystals that may damage cellular compartments and interfere with microscopic imaging. To check the tendency of the cryoprotectants to cause artifacts, sucrose and mannitol were applied to agar-embedded rhizoids in the concentration that was used during fixation (150 mM), and the effects were observed in the light microscope. Within 20 min of incubation, the cells continued growth at constant rates and did not exhibit any changes in morphology or any indication of plasmolysis, which qualified both substances to be used as cryoprotectants. Nevertheless, the period of incubation with the cryoprotectant during processing of the

rhizoid samples prior to freeze fixation was minimized and never exceeded 2 min. Rhizoids stopped growth during long-time exposure to sucrose and could therefore not be prompted to adapt to high sugar levels by gradually raising the sucrose concentration in the medium during cultivation. Sucrose proved more convenient as cryoprotectant than mannitol since the formation of ice crystals was prevented more efficiently, and the overall quality of ultrastructural preservation was superior.

Several protocols for freeze substitution of samples for ultrastructural investigations were tested. Freeze substitution with 2 or 4% $OsO_4$ in acetone provided excellent results. However, the overall contrast of the samples and the visibility of the membranes were even better when high-pressure frozen rhizoids were substituted with 1% GA + 0.1% TA in acetone before being transferred to 2% $OsO_4$. Therefore, freeze substitution for ultrastructural analyses was performed according to the protocol denoted under 2.10.2 although the exchange of the substitution medium at –80° C proved difficult.

For electron microscopic imaging, 3D dual-axis electron tomography was used which is an innovative technique for high-resolution ultrastructural research. Provided that the freezing quality of the samples is excellent and no ice crystals are present in the cytoplasm that would interfere with the accurate alignment of the image series, the cellular ultrastructure can be analyzed in serial tomographic slices with a resolution of less than 4 nm in x-, y- and, most importantly, also in z-direction. Computer-based modeling of contours in the slices of electron tomograms displays the shape and the arrangement of cellular structures and compartments in three dimensions. The results of electron tomography and 3D-remodeling in characean rhizoids are described in detail under 3.3.2 – 3.3.4.

In addition to the techniques for ultrastructural studies, a procedure was developed for the preparation of high-pressure frozen rhizoids for immuno-electron microscopy. This protocol ensures an optimum preservation of protein conformation which is required for the specific binding of antibodies (see 3.3.5). To avoid alterations of epitope structures, freeze substitution was performed with minimal concentrations of chemical fixatives. In addition, Lowicryl HM20 was chosen for embedding of the samples since polymerization of the low-viscosity resin can be performed at low temperature (–60° C), which attenuates the effects of the polymerization process on protein conformation.

After resin infiltration, the complete content of each cryocap was transferred to a flat-embedding chamber and polymerized under UV light. Rhizoids could not be oriented in the

embedding molds because space for specimen handling was very limited in the freeze substitution unit, and the weakly stained cells were undetectable in the resin. Instead, rhizoids were identified after polymerization in the transparent resin platelets by light microscopy and re-mounted for sectioning. LR-White resin which is less toxic than Lowicryl HM20 and widely used for the preparation of samples for immuno-electron microscopy was not suited for rhizoid samples although it allows embedding of the samples at RT and thereby facilitates handling. When samples were embedded in LR-White using gelatin capsules, rhizoids could not be detected in the polymerized resin blocks even when observed in the light microscope. The flat-embedding chambers used for Lowicryl HM20 did not provide an alternative since polymerized resin platelets were brittle and broke apart when they were removed from the microscope slide.

### 3.3.2 Ultrastructural characteristics of high-pressure frozen rhizoids

The ultrastructure of high-pressure frozen and freeze-substituted rhizoids was studied by conventional electron microscopy of ultrathin sections (~ 80 nm) and by high resolution electron tomography of 250-nm sections. In the different cell regions a total of 29 dual-axis tomograms was prepared using three different rhizoids which exhibited the best freezing quality of all samples tested.

Cryofixation technology that was used for the preparation of characean rhizoids efficiently eliminated fixation artifacts observed after chemical fixation and provided an excellent preservation of the cellular ultrastructure as evidenced by some remarkable features of the samples: i) the cytoplasm appeared homogeneous and no large ice crystals were observed (Fig. 19, 20), ii) cellular organelles and membrane compartments were neither swollen nor shrunken (Fig. 19, 20, 23, 24), and iii) most cellular membranes were strongly contrasted and widely visible with the three contours of the lipid bilayer (Fig. 20, 21, 23–27). Only the membranes of the endoplasmic reticulum (ER) were poorly stained, and the shape of ER cisternae had to be determined by the electron density of the lumen that was slightly higher than the density of the cytoplasm and by the parallel alignment of ribosomes at the cytoplasmic surface (Fig. 20).

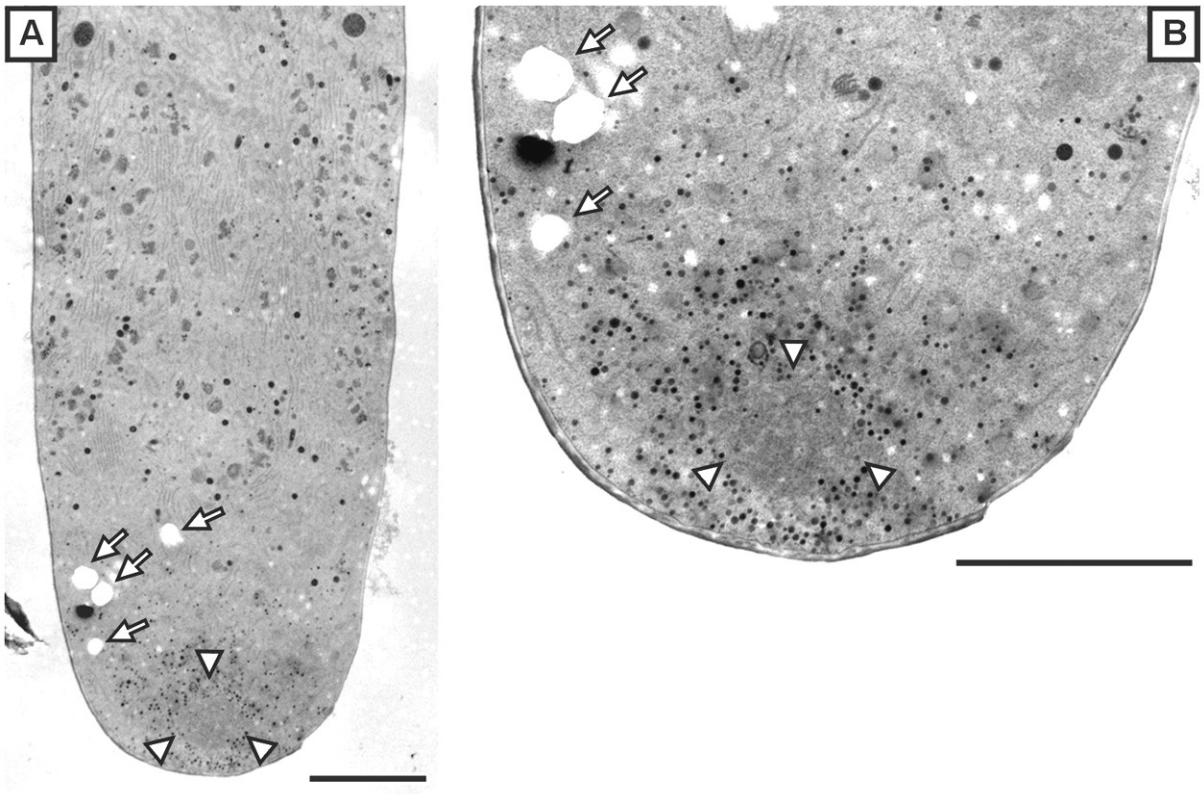


**Fig. 19** *Overview of the tip region of high-pressure frozen rhizoids*

The images that were recorded by conventional electron microscopy demonstrate the polar cytoplasmic organization of the tube-like cells. The apical cell region which comprises the statoliths (arrows) and the ER aggregate (arrowheads) in the center of the growth-organizing Spitzenkoerper complex is enlarged in B. Single cisternae of the ER aggregate were undetectable due to the poor staining of ER membranes.

Bars: 10 µm

In contrast, Golgi-stacks that typically comprised 5 – 7 cisternae (1 – 2 cis, 1 – 2 medial and 2 – 3 trans cisternae) were characterized by intensely stained membranes and by a striking polarity: The electron density of cisternal contents strongly increased from the cis to the trans cisternae whereas the width of the lumen decreased, and almost no space was observed between the membranes of the trans cisternae (Fig. 20). Precursors of newly forming cisternae were occasionally observed at the cis side (black arrows in Fig. 20), and budding profiles bearing COP-coats (coat protein) were identified at the edges of medial and cis cisternae (Fig. 20C). Large secretory vesicles (SVs) containing electron dense material were observed to bud from the trans Golgi cisternae (Fig. 20).

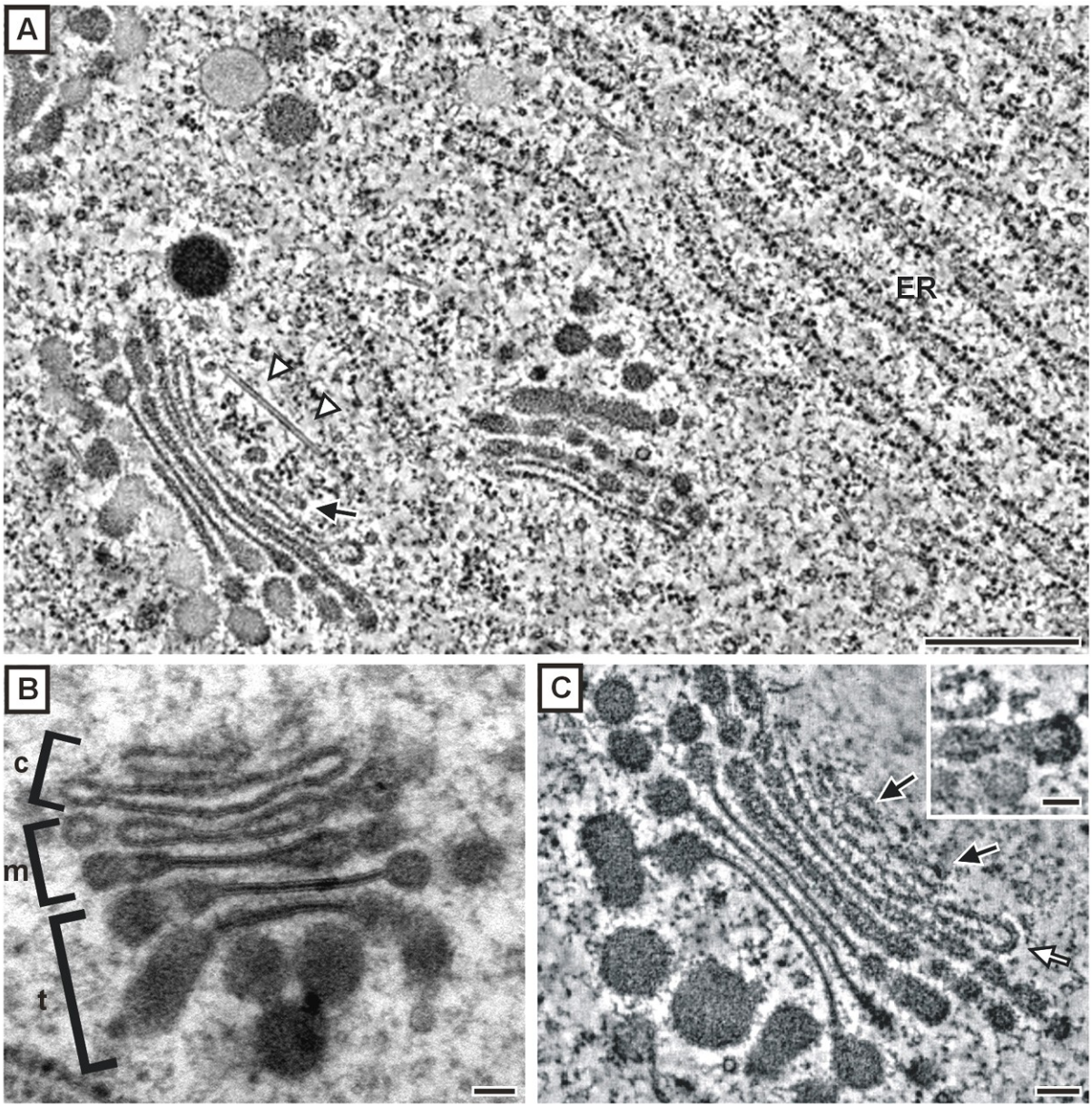


**Fig. 20** *Golgi stacks in the subapical cytoplasm of rhizoids*

The Golgi stacks in cryofixed samples of rhizoids exhibited strong polarity as revealed by electron tomography (A, C) and conventional electron microscopy (B). Cis (c), medial (m) and trans (t) cisternae (indicated by the brackets) could be clearly differentiated by luminal width and staining. Precursors of newly forming cisternae were identified at the cis side (black arrows). Budding profiles of COP-coated vesicles were observed at medial (inset in C) and cis cisternae (white arrow). C is an enlarged micrograph of the Golgi stack in the lower left corner of A from a different slice of the electron tomogram.

Arrowheads: MT. Bars: 500 nm in A, 100 nm in B–C, 50 nm inset in C

Similarly to the membranes of Golgi cisternae, the plasma membrane (PM) was also well preserved and characterized by strong contrast. It was not detached from the cell wall (CW) but found instead directly adjacent to the inner CW layer throughout the apical and subapical region of the cells (Fig. 19, 21, 26). At the apical dome, the PM was not smooth but irregularly shaped and exhibited tube-like invaginations into the cytoplasm as well as polymorphic protuberances into the CW (Fig. 21, 26). Since no spaces were observed between the PM and the CW, an artificial detachment of the membrane that might be caused by plasmolysis could be ruled out. The invaginations had a diameter of 35 – 80 nm and extended deeply into the cytoplasm (0.4 to 2.5 μm). Occasionally, a protein coat seemed to be present at their cytoplasmic surface (Fig. 21). Remodeling of the apical PM provided three-dimensional reconstructions of the invaginations and displayed their tube-like shape (Fig. 21, 26).

The high quality of high-pressure frozen rhizoid samples was underlined by the ultrastructural detection of actin microfilaments (Fig. 22 A, B) that are generally considered to be difficult to preserve for electron microscopic observation even if freeze fixation is used. The thickness of the actin structures that were identified in single tomographic slices (5 – 10 nm) indicates that single microfilaments were displayed. However, the actin microfilament system was only partly visible in the apical cytoplasm, which made tracing and modeling impossible.

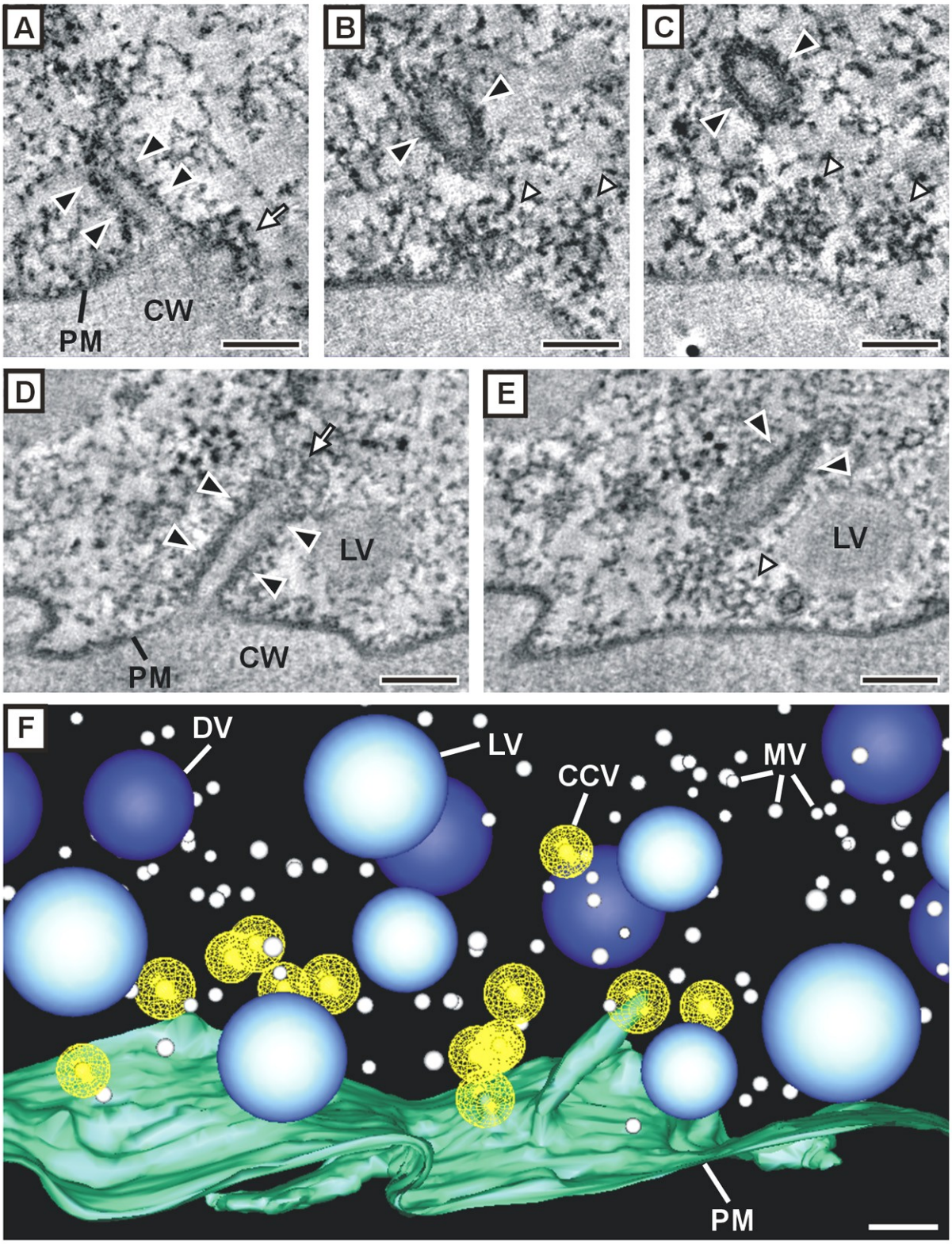


**Fig. 21** *Invaginations of the apical plasma membrane*

Micrographs A–C and D–E showing tube-like invaginations of the apical plasma membrane (black arrowheads) were taken at different planes of the corresponding electron tomograms. The three-dimensional model (F) derives from the tomogram represented by D and E and demonstrates the shape of the membrane invagination and the distribution of vesicles in the apical cytoplasm.

White arrowheads: CCVs; white arrows: budding CCVs. Bars: 100 nm

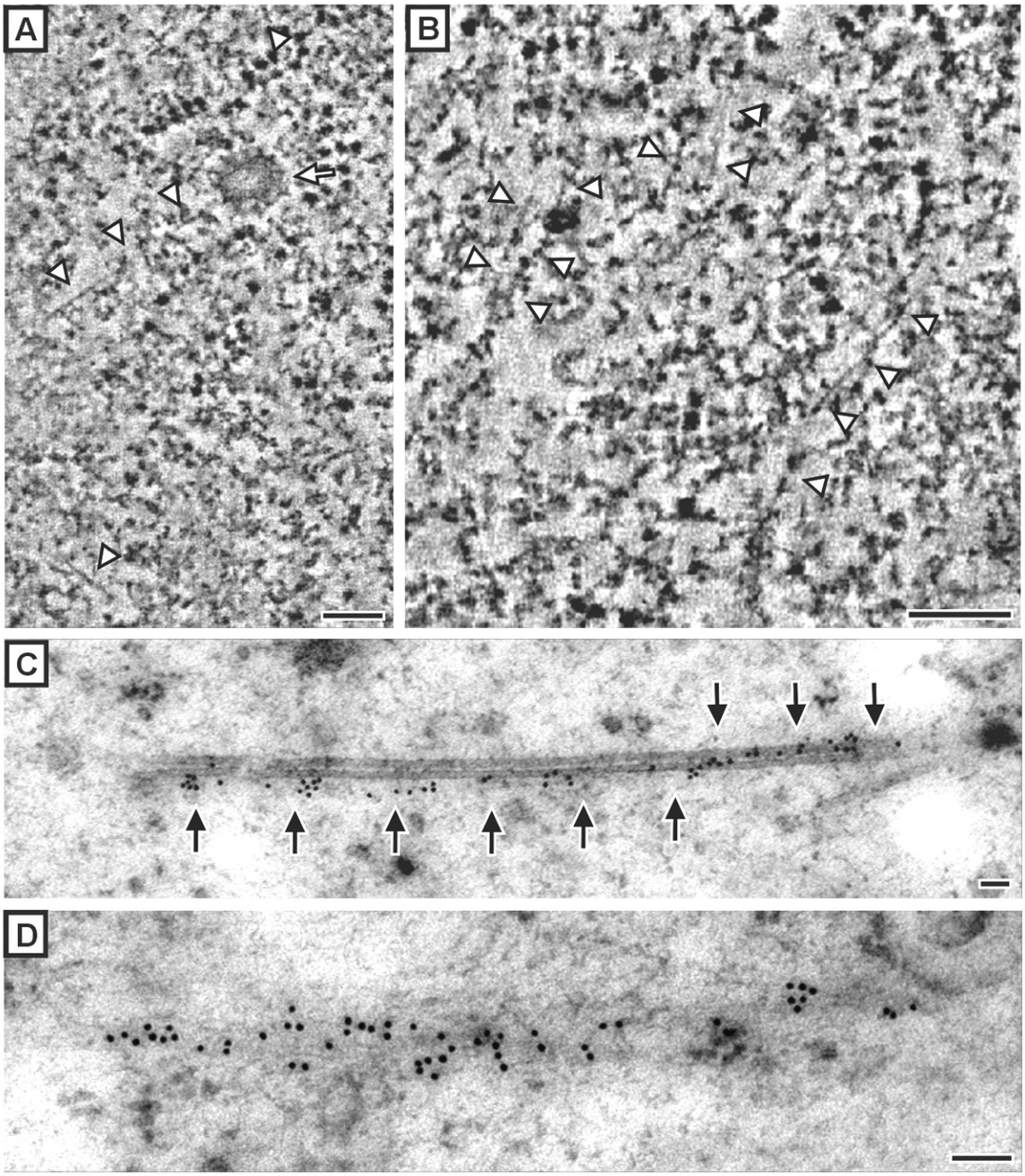


**Fig. 22** *Actin in samples of high-pressure frozen rhizoids*

Single actin microfilaments (white arrowheads) were detected by electron tomography in the region of the apical ER aggregate (A) and in the surrounding cytoplasm (B). Immunogold labeling with C4 antibody (C–D) specifically decorated bundles of actin microfilaments in the subapical cytopasm (black arrows) which were occasionally visible as underlying structures (D). The labeled microfilament bundle in C is aligned with two parallel microtubules.

White arrow: CCV. Bars: 100 nm

### 3.3.3 Identification of a vacuolar reticulum

When analyzing the ultrastructure of the Chara rhizoid a prominent membrane compartment was detected and characterized as a vacuolar reticulum based upon the striking ultrastructural similarities with a vacuolar compartment identified in fungal hyphae (see discussion 4.3.3). Previous studies failed to visualize the vacuolar reticulum in rhizoids which extended throughout the complete subapical cell region as a branched network of interconnected, vesicle-like segments (Fig. 23). The spherical segments with a constant diameter of approx. 400 nm were either aligned in rows like beads on a string (Fig. 23A) or formed highly branched polymorphic networks (Fig. 23 B, C). The components of the vacuolar reticulum were interconnected by tubes with a relatively constant diameter of 30 nm (Fig. 23 D, F) and occasionally fine, ring-like structures were observed to encircle the tubular connections (Fig. 23 F). The membranes of the reticulate compartment were often found in close proximity to MTs at distances of 15 to less than 10 nm (Fig. 23 D, E).

The luminal electron density of the vacuolar reticulum was similar to the electron density of the cytoplasm and the three contours of the strongly contrasted membranes were detectable (Fig. 23). Darkly stained, internal particles with diameters of 25 – 50 nm (Fig. 23 B, C) exhibited vesicle-like shape when analyzed by electron tomography. Occasionally, internal membranes formed large structures in the lumen indicating either invaginations of the surrounding membrane or large, membrane-enclosed inclusions (data not shown). Regarding the appearance of the membrane, the electron-density of the contents and the size of the internal structures the ultrastructure of the vacuolar reticulum resembled multivesicular bodies (MVBs; Fig. 24), spherical organelles with a diameter of 350 – 450 nm that were highly abundant in the subapical cytoplasm. However, in MVBs the density of internal particles was much higher, and MVBs were never found to be interconnected.

The vacuolar reticulum was most prominent in the subapical region of the rhizoid and close to the nucleus where it exhibited the highest number of aligned ‘beads’ and the highest degree of branching. Occasionally, the membrane system extended into the statolith region, however, the frequency was low, and the observed fragments consisted of only two or three interconnected segments. The characteristic shape of the vacuolar reticulum was never detected in the apical cytoplasm of the rhizoid

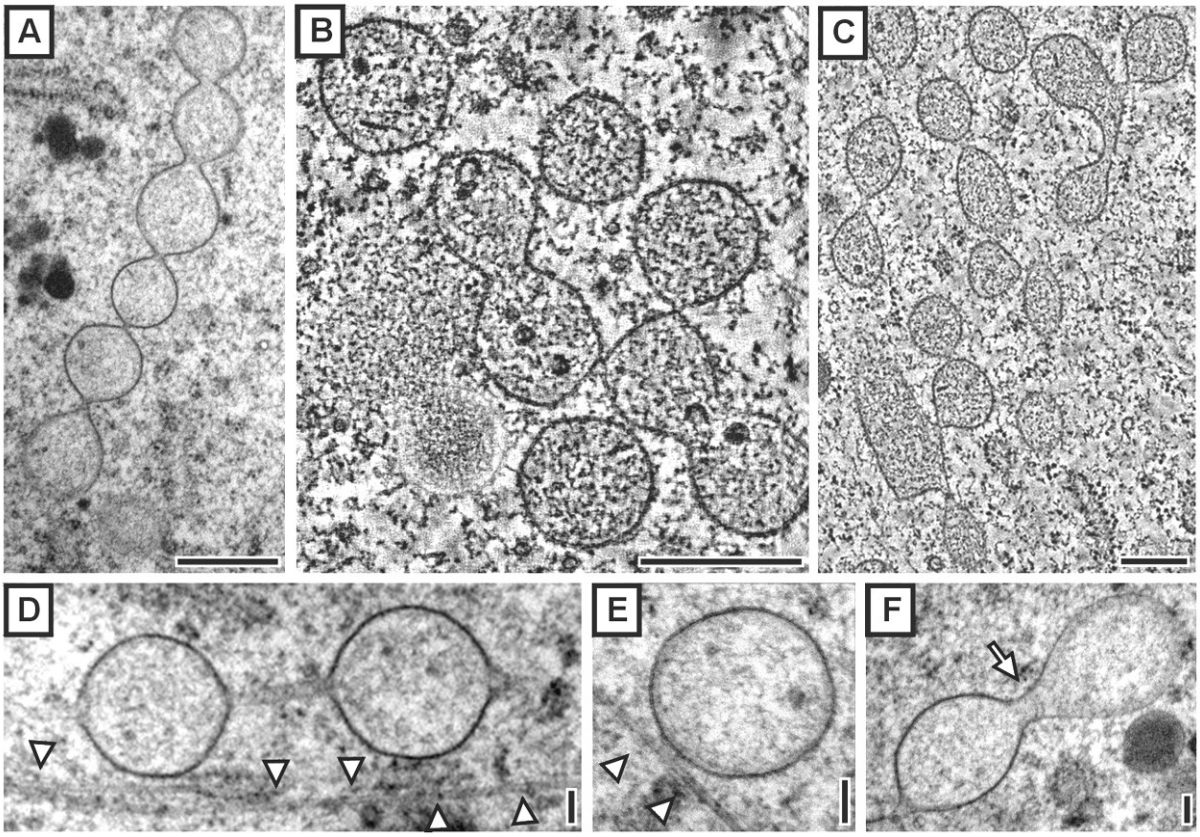


**Fig. 23** *Vacuolar reticulum*

A prominent network of interconnected, spherical segments was detected in the subapical cytoplasm of rhizoids by conventional electron microscopy (A, D–E) and electron tomography (B–C). The segments of the vacuolar reticulum which contained darkly stained internal particles (A–E) were often observed in close proximity to microtubules (arrowheads). Fine, ring-like structures encircling a tubular connection (arrow) are depicted in F.

Bars: 500 nm in A-C, 100 nm in D-F

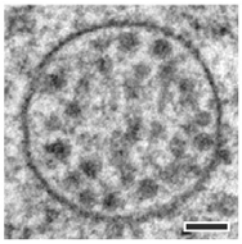

**Fig. 24** *Multivesicular body*

MVBs were observed in large number in the subapical cytoplasm of rhizoids. The micrograph which was recorded by conventional electron microscopy shows a MVB enclosing numerous internal particles.

Bar: 100 nm

### 3.3.4 Characterization of vesicle types and vesicle distribution in the cell apex

The ultrastructural analyses of high-pressure frozen rhizoids were focused on the distribution of vesicles at the apical PM and within the growth-organizing Spitzenkoerper complex in order to unravel basic principles of vesicle-mediated tip growth in characean rhizoids. Due to the limited resolution of conventional electron microscopy the specific ultrastructural features of the different vesicle types could only be detected by electron tomography. Five vesicle types were found in the apex of characean rhizoids that were distinguished by size, electron density and by the presence of a protein coat (Fig. 25; Table V). A schematic reconstruction of the distribution of all vesicle types in the apical cytoplasm of rhizoids is depicted in Fig. 31 of the discussion section.

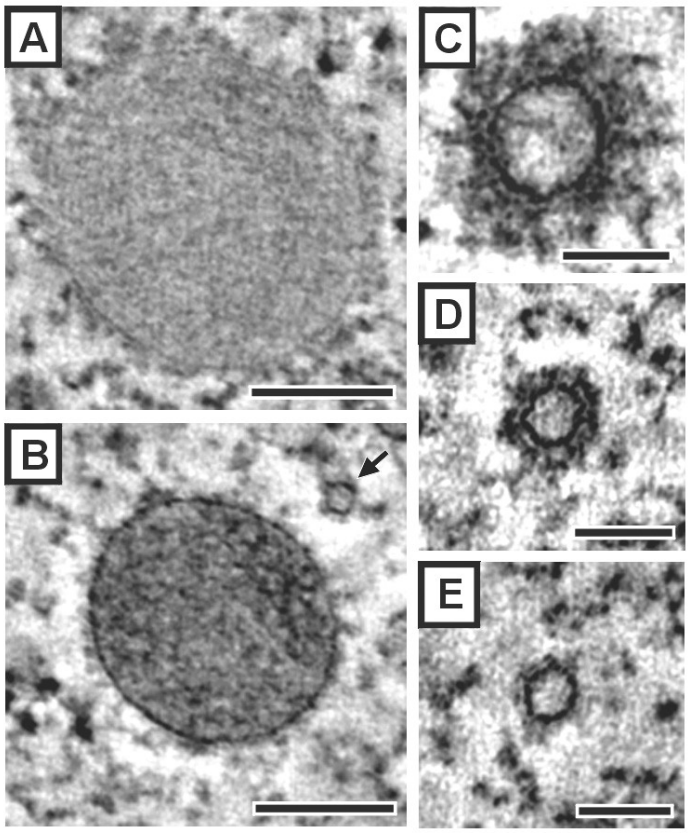


**Fig. 25** *Vesicle types in the apical cytoplasm of rhizoids*

The micrograph displays the different types of vesicles in the apical cytoplasm as observed by electron tomography.

A: Light vesicle

B: Dark vesicle (arrow points to a microvesicle)

C: Clathrin-coated vesicle

D: Coated vesicle

E: Microvesicle

Bars: 100 nm in A–B, 50 nm in C–E

**Table V** *Criteria of the vesicle types in the apical cytoplasm of characean rhizoids*
Vesicle radii were determined in 3D-models of electron tomograms using the 'imodinfo' command of the IMOD software package. Values are means ± SE and the number of measured vesicles (n) is shown in parentheses. As a more common value, the corresponding vesicle diameters are listed in addition. To determine the vesicle density in electron tomographic reconstructions, the number of vesicles was referred to the cytoplasmic volume of the corresponding tomogram which was calculated by considering the area of cytoplasm covered by the tomogram and the section thickness of 250 nm. Values indicate the range of vesicle density as observed in different tomograms. For clathrin-coated vesicles, the populations associated with the plasma membrane (PM) and with the ER aggregate (ER) are listed separately.

| Vesicle type | | Radius *nm* | Diameter *nm* | Vesicle density *vesicles per µm³ cytoplasm* |
|---|---|---|---|---|
| Light vesicles | | 100.8 ± 14.0 (n = 55)[a] | 201.7 | 9.5 – 18.8 |
| Dark vesicles | | 89.5 ± 15.2 (n = 75)[a] | 179.1 | 14.7 – 25.3 |
| Clathrin-coated vesicles | ER | 21.7 ± 3.4 (n = 119)[b] | 43.3 | 19.5 – 25.4 |
| | PM | 15.4 ± 2.7 (n = 66)[b] | 30.8 | 12.1 – 28.4[c] (56.4 – 79.4)[d] |
| Coated vesicles | | 14.2 ± 2.8 (n = 110)[b] | 28.4 | 9.6 – 38.9 |
| Microvesicles | | 12.5 ± 2.0 (n = 1309)[b] | 25.0 | 174.7 – 421.9 |

[a,b] Mean radii of vesicle types were significantly different (student´s t-test $P < 0.01$)
[c] Calculated relative to total cytoplasmic volume
[d] Calculated relative to the volume of the 500 nm-broad cytoplasmic region along the apical PM

#### 3.3.4.1 Large vesicles

Two different types of vesicles with diameters of approximately 200 nm were identified in the apical cytoplasm of rhizoids. Although they exhibited specific ultrastructural differences (see below), both types are in the following referred to as large vesicles because vesicle size is the most prominent property in order to distinguish these vesicles from all other vesicle types. Large vesicles were observed to accumulate in the apex of rhizoids where they were strongly enriched at the periphery of the apical ER aggregate but evenly distributed in the cytoplasm adjacent to the apical PM (Fig. 21, 26, 31). Large vesicles were excluded from central regions of the ER aggregate which was less prominent in high-pressure frozen samples than in chemically fixed samples due to the poor contrast of the membranes.

The first type of large vesicles (Fig. 25 B) was characterized by darkly stained contents that exhibited similar electron density as the contents of vesicles budding from trans Golgi cisternae (Fig. 20). These dark vesicles (DVs) with a mean diameter of 179.1 nm were encircled by a strongly contrasted membrane. Light vesicles (LVs), the second type of large vesicles in the apical cytoplasm, had a mean diameter of 201.7 nm and were significantly larger than DVs (student´s t-test $P < 0.01$) but less abundant (Table V). They could be clearly

discriminated from DVs by the low electron density of the vesicle contents and by their poorly stained membranes that appeared much thinner (Fig. 25 A).

#### 3.3.4.2 Microvesicles

Small microvesicles (MVs) with a mean diameter of 25.0 nm exhibited the highest density of all vesicle types (up to 421.9 per $\mu m^3$ cytoplasm; Table V). They were evenly distributed throughout the apical cytoplasm but were only rarely found in central regions of the ER aggregate (Fig. 21, 26, 27, 31). Vesicle membranes were strongly stained, and the electron density of the contents was similar to the electron density of the cytoplasm (Fig. 25E).

#### 3.3.4.3 Clathrin-coated vesicles

In this study, clathrin-coated vesicles (CCVs) were unambiguously identified in the apical cytoplasm of rhizoids. This vesicle type has not been described in rhizoids before. CCVs (Fig. 25C) were recognized by the prominent structure of their typical cage-like protein coat which is composed of hexagons and pentagons formed by the clathrin molecules. The regular structure of the protein coat was particularly well visible in tomographic slices crossing the periphery of vesicles (Fig. 26, 27). Two populations of CCVs were distinguished by their specific distribution in the apical cell region.

Vesicles of the first population had a mean diameter of 30.8 nm, and the clathrin coat with a thickness of approx. 30 nm formed a cage of 92.8 nm in diameter (Table V). They were exclusively observed in a 500 nm-broad cytoplasmic region adjacent to the apical PM (Fig. 21, 26), and their density decreased from the cell tip towards the flanks. CCVs at the apical PM were not evenly distributed but appeared in clusters of 3 – 10 vesicles (Fig. 21, 26). The vesicle clusters were occasionally observed to surround the tube-like invaginations of the membrane described under 3.3.2. Several clathrin-coated buds were identified at the apical PM which represent stages of CCV-formation (white arrows in Fig. 21A, 26C). Sometimes, CCVs were observed to be formed at the cytoplasmic ends of the PM-invaginations (Fig. 21D, F; white double arrowhead in Fig. 26D).

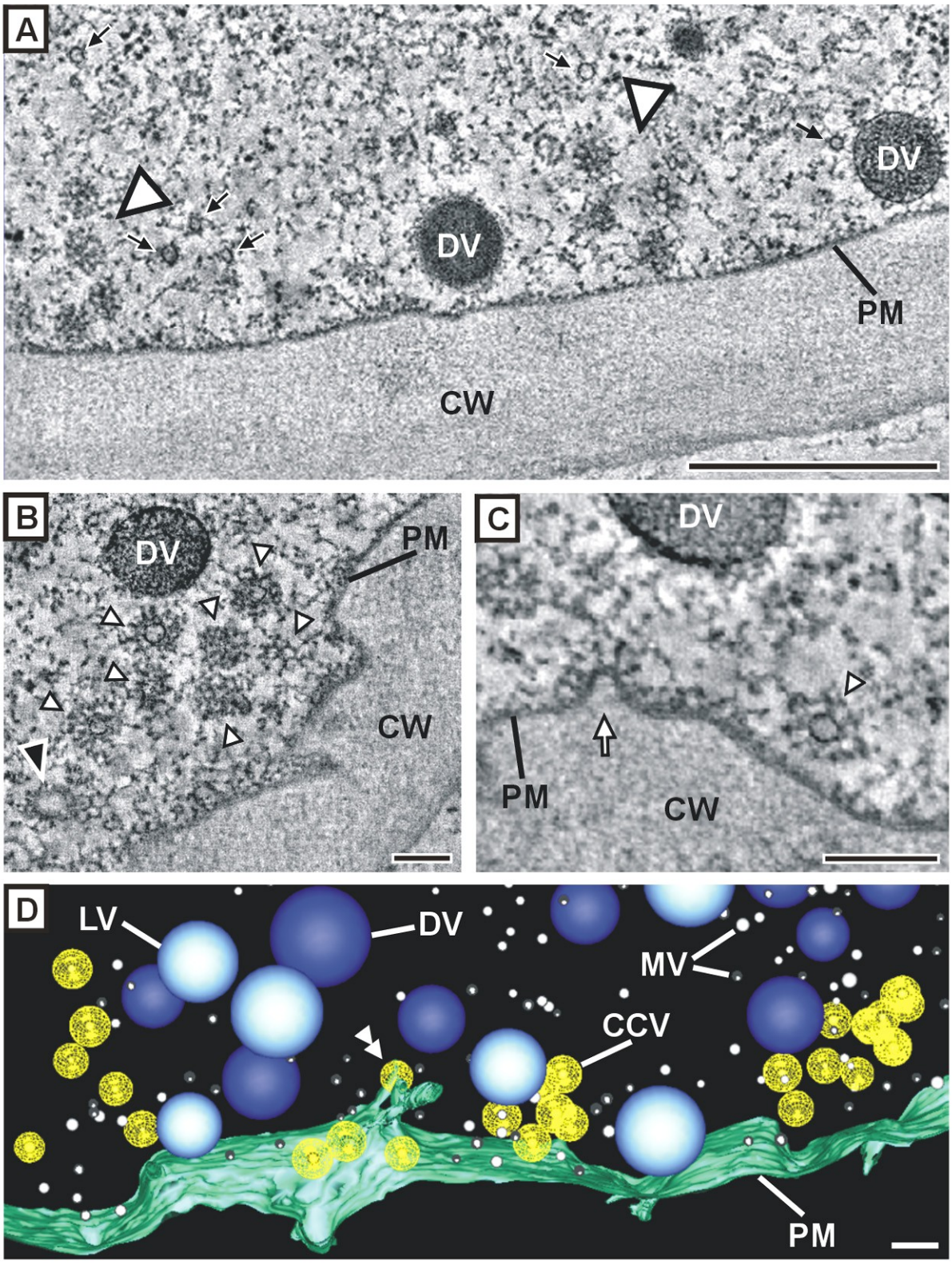


**Fig. 26** *Distribution of CCVs at the apical PM*

Electron tomographic analysis revealed that CCVs (small white arrowheads) at the apical PM of rhizoids were arranged in clusters (large white arrowheads). CCVs were formed at clathrin-coated buds (white arrow) and at the cytoplasmic ends of PM invaginations (white double-arrowhead). A 3D-model of the vesicle distribution at the apical PM is depicted in D.

Black arrows: MVs; black arrowheads: invagination of the apical PM. Bars: 500 nm in A, 100 nm in B-D

The density of plasma-membrane associated CCVs was in the range of 12 to 28 vesicles per $\mu m^3$ relative to the total volume of cytoplasm covered by the tomograms and 56 to 80 vesicles per $\mu m^3$ relative to the volume of the 500 nm-broad cytoplasmic region along the apical PM where they were exclusively detected (Table V). As discussed under 4.3.2.3 the latter calculation is more accurate for estimating the density of vesicles that are involved in endocytosis.

The second population of CCVs in the Chara rhizoid was confined to the cytoplasm in the region of the apical ER aggregate and was separated from the population of PM-associated CCVs by an at least 1 µm-broad cytoplasmic region where CCVs were never observed (Fig. 31). CCVs were detected in the center as well as at the edges of the ER aggregate with a density of ~ 20 vesicles per $\mu m^3$ cytoplasm and were occasionally observed to form vesicle clusters (Fig. 27). Interestingly, at least in one case, two CCVs were interconnected by a membrane cisterna (Fig. 27C – E). ER-associated CCVs had a mean diameter of 43.4 nm and were significantly larger (student´s t-test, $P < 0.01$) than the population of CCVs at the PM (Table V), whereas the thickness of the protein coat was consistent (~ 30 nm), and no differences were observed in the structure of the clathrin scaffold and in the electron density of the vesicle contents between both populations.

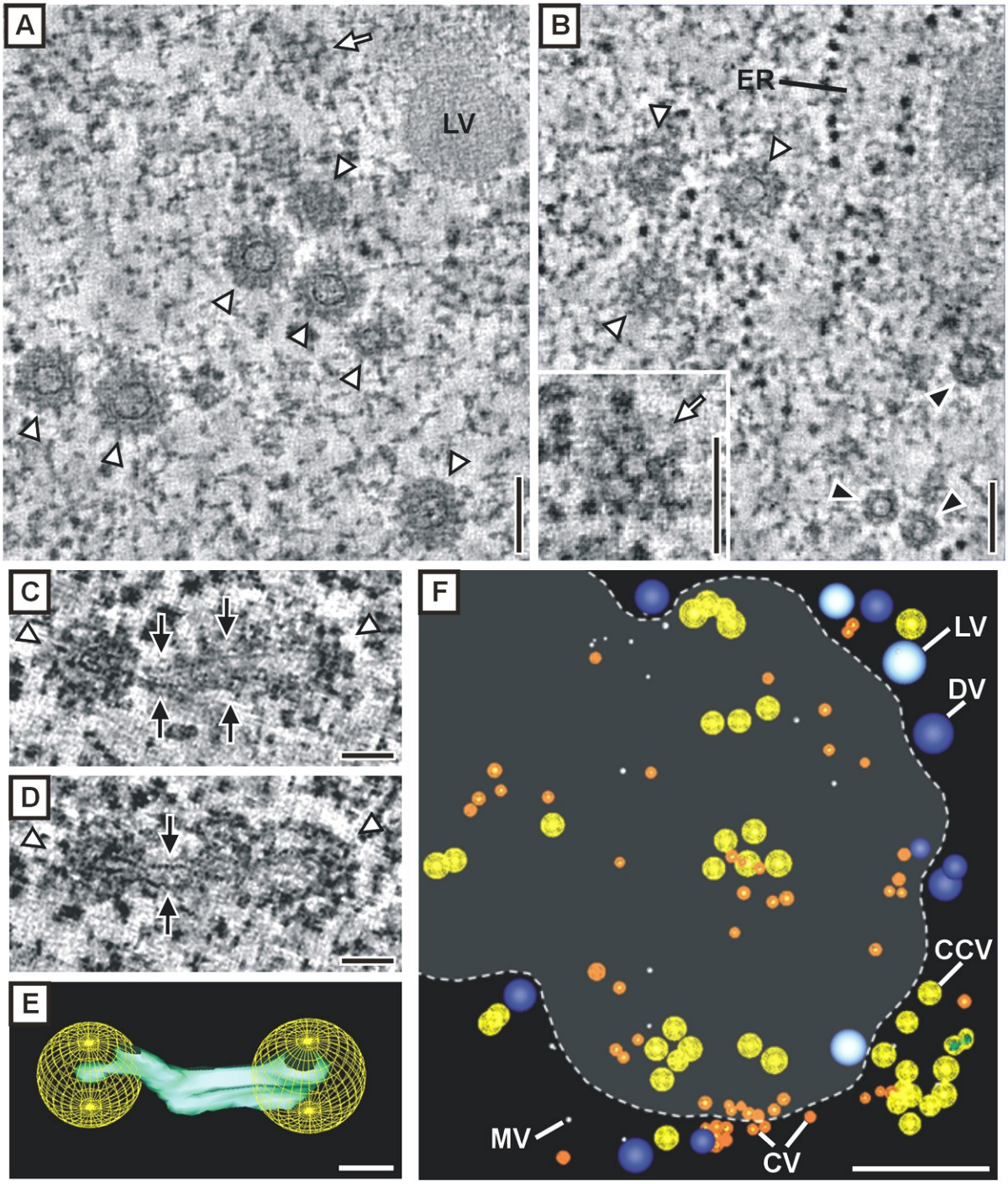


**Fig. 27** *Vesicle distribution within the cytoplasm of the apical ER aggregate in the apex of rhizoids*

A–B: Electron tomographic images showing cytoplasmic CCVs (white arrowheads) and CVs (black arrowheads) within the apical aggregate of ER cisternae (ER). The structure of the clathrin lattice of CCVs was clearly detectable (white arrows).

C–E: CCVs (white arrowheads) within the cytoplasm of the ER aggregate that were interconnected by a membrane cisterna (black arrows). C and D are micrographs from different planes of the electon tomogram. E shows the 3D-model of the structure. The cisternal membrane was modeled in green and clathrin coats in yellow.

F: Three-dimensional tomographic reconstruction demonstrating the distribution of vesicles in central regions and in the periphery of the apical ER aggregate. The shaded area indicates the shape of the ER aggregate.

Bars: 100 nm in A–B, 50 nm in C–E, 500 nm in F

#### 3.3.4.4 Coated vesicles

The fifth vesicle type identified in the apical cytoplasm of characean rhizoids was characterized by an electron dense coat at the cytoplasmic membrane surface which was, however, clearly different from the protein scaffold of CCVs. The protein coat of the coated vesicles (CVs) was only 10 nm thick and was homogeneously stained instead of forming a regular structure (Fig. 25D). CVs were slightly but significantly (student´s t-test, $P < 0.01$) smaller than CCVs (mean diameter 28.4 nm, Table V) and contained material with similar electron density (Fig. 25C, D). The vesicles accumulated at the edges of the apical ER aggregate and were found at lower density in central regions of the aggregated cisternae (Fig. 27, 31). CVs were rarely observed at distances larger than 500 nm from the ER aggregate and in the cytoplasm flanking the apical PM.

### 3.3.5 Immuno-electron microscopy

Rhizoid samples prepared for immuno-electron microscopy were characterized by a good preservation of the cellular ultrastructure although some of the samples exhibited locally confined mechanical damage which was predominantly observed at the outermost cell tip. The samples exhibited poor overall contrast because no $OsO_4$ or tannic acid was present in the freeze substitution medium. However, all major cellular compartments could be identified in the electron microscope after counterstaining of thin sections. Most importantly, protein conformation was excellently preserved and not altered during preparation as evidenced by the specific immunolocalization of various proteins.

When using C4 antibody that was raised against a conserved actin epitope, gold particles were found to be localized to parallel bundles of longitudinally oriented actin microfilaments in the subapical region of rhizoids (Fig. 22C, D). The specificity of the antibody binding to actin is highlighted by several observations (Fig. 22C, D): i) gold particles were never randomly distributed in the cytoplasm, ii) gold particles were absent from the lumen of cellular organelles and compartments, and iii) no labeling pattern was detected when the primary antibody was omitted and replaced by buffer in control samples. Fig. 22C shows the labeling of an actin microfilament bundle over a distance of approx. 1 µm. Although the filament bundles can barely be detected, the aligned gold particles clearly indicate that the microfilaments run in parallel to the MTs and cross them further apart. Actin labeling with a similar dimension of longitudinal extension is rare since it can only be observed when the

orientation of the actin bundle and of the section surface is absolutely parallel. In some cases, microfilament bundles were detectable as structures underlying the specific labeling pattern (Fig. 22D).

Using an antibody that was raised against an immunogen within the terminal globular domain of rat clathrin heavy chain, circular clusters of gold particles were observed in the subapical cytoplasm. These clusters were closely associated with MTs and were most abundant in cytoplasmic regions where the section crossed MTs or ran slightly above or below (Fig. 28A, B). The diameter of the gold clusters was in a range of 100 nm, which is well in accordance with the diameter of the protein cage of CCVs. It is therefore assumed that the clathrin antibody labeled CCVs that were aligned with MTs. In addition to the labeling in the subapical region of rhizoids, gold particles were also observed in the apical cytoplasm within the region of the ER aggregate. The gold particles that could hardly be distinguished from ribosomes at the luminal site of the ER cisternae, were found in similar clusters as in the subapical region (Fig. 28C–E). The vesicle-like pattern of clathrin immunolabeling fits well to the observations gathered in electron tomographic analyses of the apical cytoplasm demonstrating that numerous CCVs are associated with the apical ER aggregate (Fig. 27). However, no labeling was detected at the apical PM, which is attributed to poor ultrastructural preservation or mechanical damage of the outermost tip region of the samples. Labeling of CCVs in the subapical and apical regions of rhizoids was not observed in control samples, which demonstrates the specificity of antibody binding.

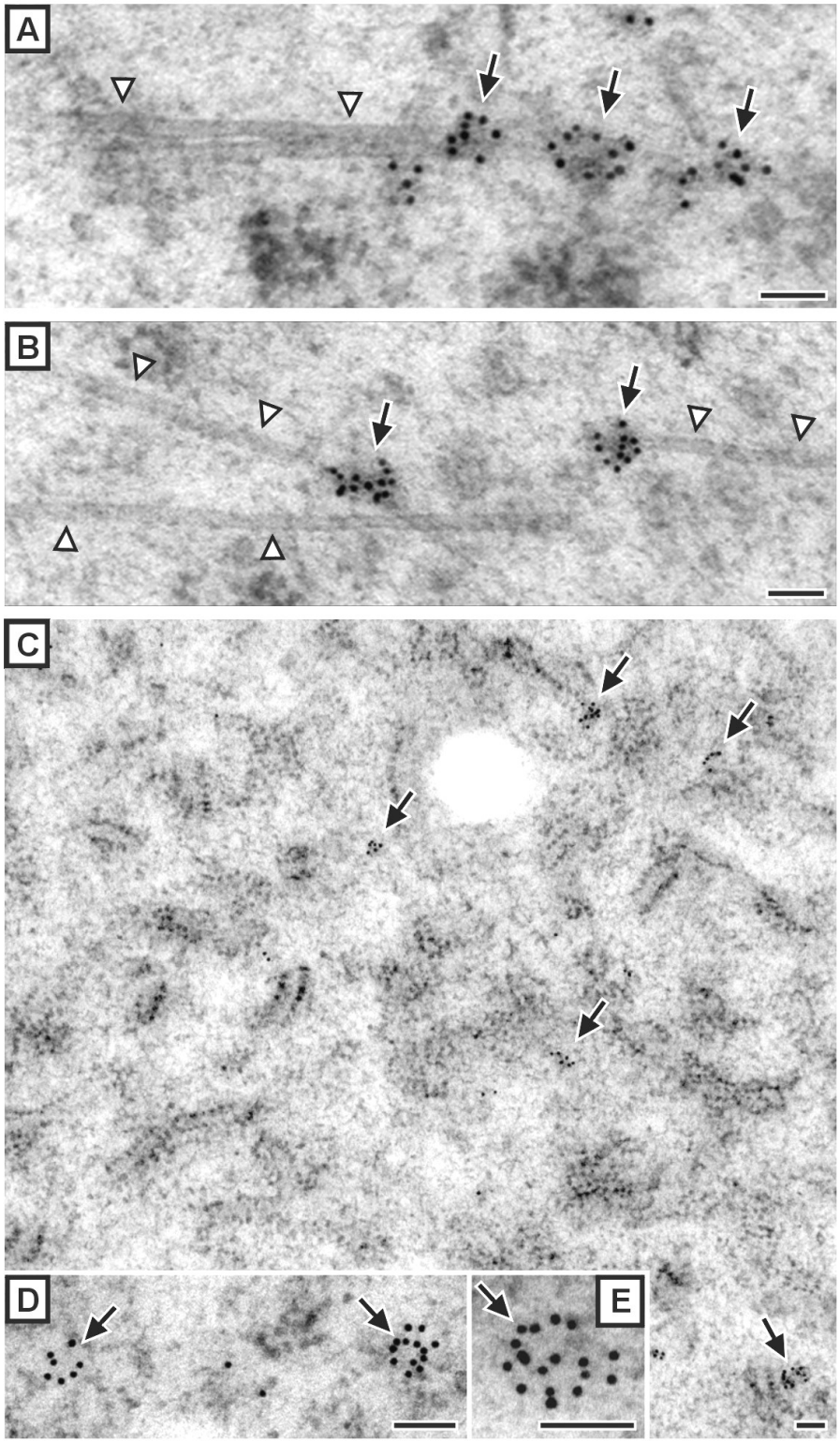


**Fig. 28** *Immunolocalization of CCVs in high-pressure frozen rhizoids*

Clusters of gold particles (black arrows) were observed after immunogold labeling with a clathrin-specific antibody. These clusters which represent CCVs were closely associated with MTs (white arrowheads) in the subapical cytoplasm (A–B). In the cell apex (C–E), CCVs were found within the region of the apical ER aggregate. ER cisternae were detectable by the parallel rows of ribosomes at their cytoplasmic surfaces (C).

Bars: 100 nm

## 3.4 Fluorescence staining of rhizoids with vital dyes

Various fluorescence dyes were used for in-vivo labeling of characean rhizoids in order to examine dynamic properties of certain cellular compartments that were identified by ultrastructural investigations in this study. Since CCVs associated with the apical PM are suggested to be involved in endocytotic processes, rhizoids were stained with FM dyes that are used in a wide range of different specimens to study dynamic aspects of endocytosis and to label endocytotic compartments. The styryl dyes are inserted into the outer leaflet of the PM and are thereby converted from the non-fluorescent to the fluorescent state. They do not permeate the membrane and are incorporated into cells by the internalization of stained membrane material.

When characean rhizoids were stained with FM 1-43 and FM 4-64 the fluorescence pattern was identical with both dyes. Since no difference in the staining pattern was detected whether the dyes were washed out before microscopic observation or not, samples were incubated in staining solution during microscopy to increase fluorescence intensity. Immediately upon application of the dyes, the PM was strongly labeled (Fig. 29A). Subsequently, the dyes accumulated in the cytoplasm and produced homogeneous staining of the cytoplasm with the fluorescence intensity being slightly higher in the cell region 0 – 100 μm from the tip than further apart (Fig. 29). The center of the Spitzenkoerper comprising the ER aggregate was less intensely stained than the apical cytoplasm (Fig. 29A) and was occasionally surrounded by a brightly fluorescing ring that was pronounced against the background fluorescence of the cytoplasm (Fig. 29B). The described staining pattern did not noticeably change during extended incubation (45 – 90 min) with the fluorescence dyes. FM staining did not label any distinct cellular compartments, and uptake of the dyes was not found to be concentrated at certain domains of the apical PM.

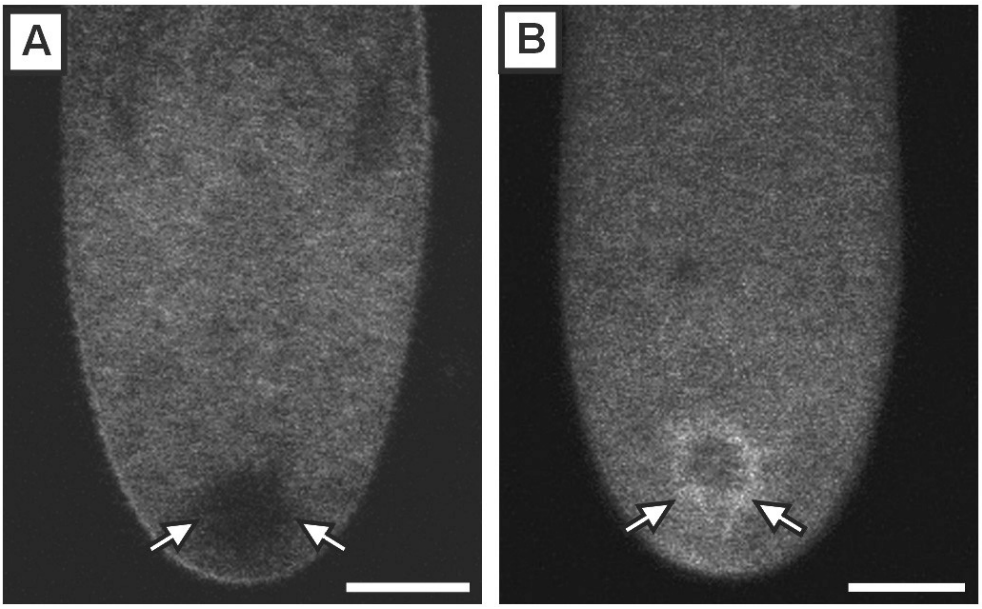


**Fig. 29** *In-vivo fluorescence staining of rhizoids with FM dyes*

Fluorescence labeling of rhizoids with 1 µM FM 4-64 produced homogeneous staining of the apical cytoplasm. The region of the apical ER aggregate (arrows) exhibited weak fluorescence intensity (A) and was occasionally surrounded by a brightly fluorescing ring (B). No differences in staining pattern were observed whether the dye was washed-out before microscopy or not. Micrographs are confocal microscopic images.

A: Rhizoid sample incubated in staining solution during microscopy 7 min after the application of the fluorescence dye

B: Rhizoid sample 45 min after wash-out of the dye which was applied for 2 min

Bars: 10 µm

In order to verify that the network of interconnected spherical membrane segments that was identified in electron microscopic images is a vacuolar compartment, living rhizoids were stained with fluorescence dyes that accumulate in plant vacuoles. Esterified, non-fluorescent carboxy-DFFDA freely permeates the PM and is hydrolyzed by intracellular esterases releasing the fluorescent product that accumulates subsequently in vacuolar compartments. DFFDA is imported across the tonoplast membrane by an anion transporter but cannot leave the vacuoles due to the lack of a corresponding transporter operating in the reverse direction.

Rhizoids were stained for 10 min with 10 to 25 µM carboxy-DFFDA. For fluorescence microscopy the dye was washed-out, and samples were observed in fresh medium. Starting at 15 min after probe wash-out a prominent network was detected against the cytosolic background fluorescence in growing cells (Fig. 30A, B). The fine network extended throughout the entire subapical region from the statolith region to the nucleus but was not present in the cell apex (Fig. 30C). In non-growing rhizoids, the strands of the network were dilated, and brightly fluorescing patches were detected. The fluorescence of the labeled

network bleached strongly during microscopic observation, which made the recording of time-series difficult. However, the network was observed to be highly dynamic with existing connection points being displaced and new connections between strands being formed (Fig. 30D–F). During prolonged incubation in fresh medium the fluorescence accumulated in the basal vacuole whereas the intensity of the subapical cytoplasm and of the network decreased.

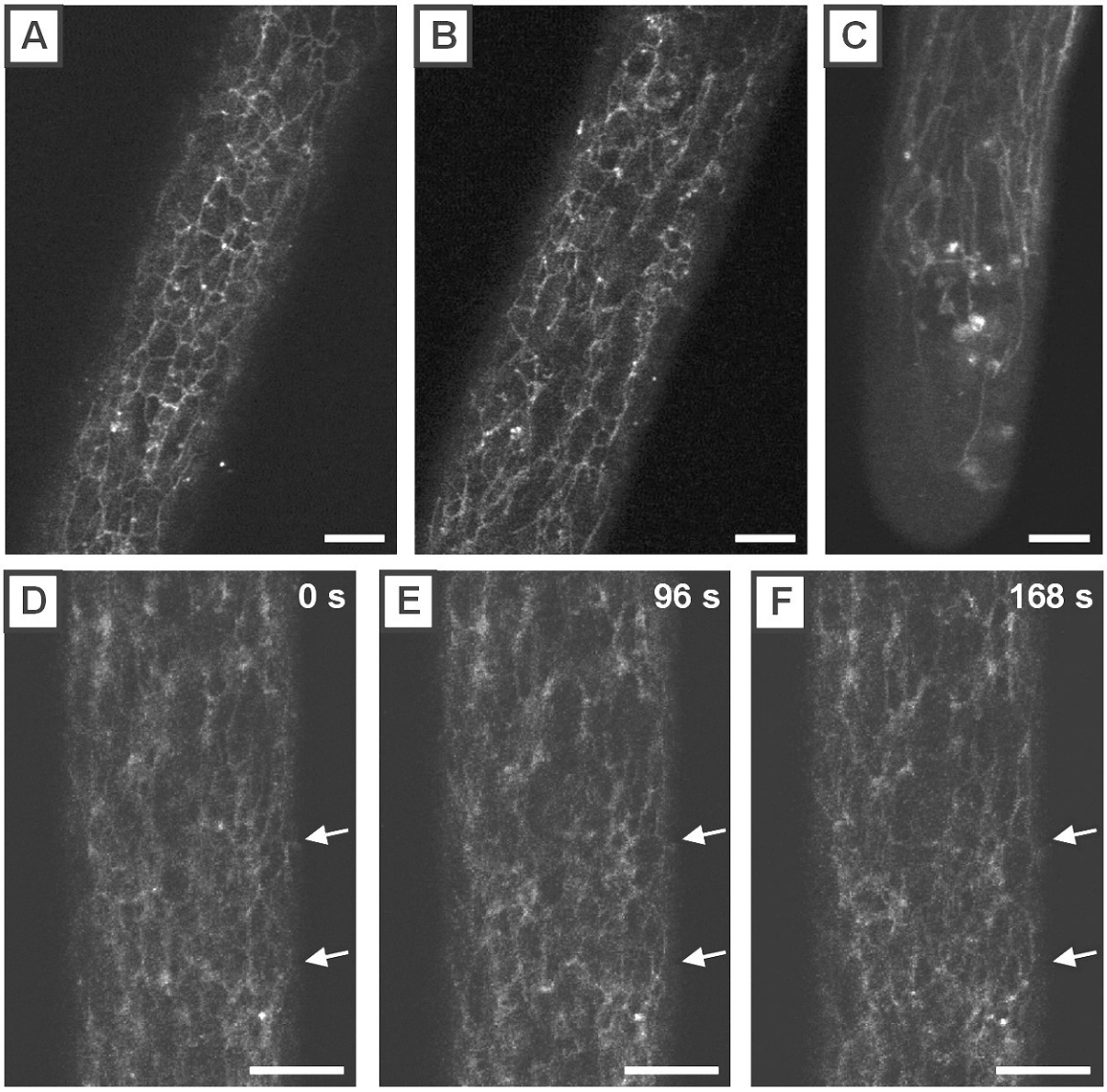


**Fig. 30** *In-vivo fluorescence staining of rhizoids with carboxy-DFFDA*

An extensive fluorescenct network was observed in the subapical region of rhizoids (A–B, D–F) after staining with carboxy-DFFDA which was applied for 10 min in concentrations of 10 µM (A–B, D–F) or 25 µM (C). No labeling was observed in the cell apex (C). Dynamic remodeling of the labeled network (arrows) was detectable in time series (D–F; time is indicated in s after start of the time series). All micrographs are confocal microscopic images and were recorded 32 min (A–B, D–F) or 34 min (C) after wash-out of the dye. Micrographs A and B are single confocal images at different planes of the same sample.

Bars: 10 µm

Further labeling experiments were performed using the dye BCECF which was loaded to the cells as non-fluorescent acetoxymethyl ester derivate (BCECF-AM). Hydrolysis of the ester group by intracellular esterases releases the fluorescent dye which exhibits a pH-dependent fluorescence excitation profile. Therefore, BCECF is widely used as indicator for intracellular pH and cell viability. In plants, the fluorescence dye has been reported to accumulate in vacuoles of root hairs at concentrations in the range of 3 µM producing a staining pattern that was similar to DFFDA (Brauer et al. 1995).

The dye was applied to rhizoids in a wide range of concentrations (0.01 – 5 µg $ml^{-1}$), and samples were either washed with fresh medium prior to microscopy or incubated in staining solution during microscopic observation. In none of the samples any cellular compartment was labeled. Instead, the entire cytoplasm was homogenously stained. Occasionally, the fluorescence intensity was slightly higher in the basal vacuole than in the subapical cytoplasm. However, BCECF is not suited for the specific labeling of vacuolar compartments in characean rhizoids.

# 4 DISCUSSION

## 4.1 Molecular biology

The molecular biological part of the study was designed to identify genes being involved in gravitropic signaling in characean rhizoids and protonemata and to extend genomic information about the green alga Chara by sequencing gene transcripts of rhizoids. Differential display analysis of gene expression was based upon the amplification of random fragments of the 3'mRNA-ends that were compared between differentially stimulated samples by capillary electrophoresis. mRNA extracts of rhizoids were also used for partial sequencing of a specific member of the myosin class of proteins which has been shown to play a crucial role in gravity sensing and tip growth by mediating the transport of SVs and the positioning of statoliths.

In this study, techniques for the efficient isolation of mRNA from characean rhizoids and protonemata were developed, and basic molecular biological applications were optimized for these cell types. New full length gene sequences were determined, and first insights into molecular aspects of gravitropic signaling were provided. Thereby, a basis was established for further investigations of gravity sensing and tip growth at the molecular level.

### 4.1.1 Isolation of mRNA from characean rhizoids and protonemata

Since the present study was the first to analyze mRNA transcripts in single-celled characean rhizoids and protonemata, the procedures for cell extraction and RNA-isolation were developed and optimized inorder to achieve maximum yield and purity of the isolated RNA. It has been reported from several cell types that DNA was successfully amplified in extracts obtained by single-cell aspiration of few cells (Karrer et al. 1995; Brandt et al. 1999; Gallagher et al. 2001; Brandt et al. 2002; Laval et al. 2002; Jones and Grierson 2003). Extraction of cytosol from single cells by the insertion of a microcapillary was shown to minimize contamination of cell extracts and to be well suited for the analysis of mRNA transcripts in specific cell types. In this study, single-cell aspiration was tested for the extraction of cytosol from rhizoids and protonemata. It proved to be the only technique that was reasonable for purifying mRNA from the very limited number of protonemata that grow out from the thallus with low frequency and density.

mRNA isolated from pooled extracts of 25 cells was an adequate template for gene-specific PCR amplification in rhizoids and protonemata. However, these extracts were not suited for differential display analysis. The number of fragments that were detected after random-primed PCR was low and fragment patterns varied between different samples, making a comparison of gene expression levels impossible. The unsatisfying results in differential display analyses of microextracted samples are attributed to the use of non-specific random primers that did not efficiently bind to low-abundance transcripts and to the Monte Carlo effect (Karrer et al. 1995) which describes the difficulties in displaying the true abundance of rare transcripts after PCR amplification.

Several authors report using of extracts of single cells for subsequent PCR amplification in various cell types (Karrer et al. 1995; Brandt et al. 1999; Laval et al. 2002). In rhizoids and protonemata, no products were detectable after PCR amplification in single-cell extracts, which may be due to an insufficient grade of purity of the isolated mRNA. However, single-cell aspiration with pooling of a small number of cells is well suited for providing cell extracts designated for gene-specific PCR amplification in higher plant cell types (Gallagher et al. 2001; Brandt et al. 2002; Laval et al. 2002; Jones and Grierson 2003) as well as in characean rhizoids and protonemata (this study).

Due to the low concentration of mRNA in the extracts obtained by single-cell aspiration, samples for the random-primed PCR reactions of the differential display protocol were prepared by collecting 50 rhizoid bundles that were removed from the agar layer prior to cell lysis. As demonstrated by capillary electrophoresis, this method provided decent templates for the analysis of gene expression patterns. Most of the fluorescence peaks appeared at identical positions in gravistimulated samples and in unstimulated controls and exhibited consistent intensities, thereby confirming that the amount of mRNA in the extracts was comparable and RNA was not degraded during extraction and processing of the samples.

The isolation of polyA$^+$-mRNA from the cell extracts was based upon hybridization with dT-oligonucleotides linked to Oligotex latex beads that were collected by centrifugation. This technique ensured the removal of rRNA, tRNA and contaminations with procaryotic mRNA because these RNA-types do not possess a polyA$^+$-sequence that could bind to the dT-oligonucleotides. The results of the different PCR applications performed in this study demonstrate that the isolation protocol was well suited for the efficient purification of mRNA from a very small amount of starting material.

### 4.1.2 Full-length characterization of characean ribosomal proteins

As the land plants' closest living relative, the green alga Chara is situated at an important evolutionary position at the transition from the lower plants to the highest stage of development in the plant kingdom (Lewis and McCourt 2004). Specific regions of plastid-encoded genes and ribosomal RNAs of diverse characean algae (e.g. McCourt et al. 1999; Karol et al. 2001) as well as the complete mitochondrial genome of *Chara vulgaris* (Turmel et al. 2003) have been sequenced and compared with the corresponding sequences of related phyla for elucidating evolutional relationships and defining crucial steps of development. However, the genome of characean algae has not been systematically sequenced and molecular information about nuclear-encoded proteins of characean algae available at genome databases is scarce.

The present study provides the full length coding sequences of two genes that were clearly identified to encode ribosomal proteins of class L14 and L27, respectively, based upon a significant level of homology with the corresponding proteins from a wide range of species including higher plants, mouse and human. Ribosomal proteins are strongly expressed housekeeping genes that play a role for metabolic pathways by mediating the assembly of ribosomes and regulating protein biosynthesis (Alberts et al. 1995; Nicot et al. 2005). Determination of the nucleotide sequences of the characean ribosomal proteins and publishing in the genome databases contributes to the extension of genomic information about characean algae. In addition, the molecular techniques are now available for the sequencing of further gene transcripts present in rhizoids. Proteins involved in the regulation of tip growth and gravity sensing can be identified by similar approaches using PCR amplification with degenerate primers that bind to conserved domains of homologous proteins in other species. As discussed below, this approach was successfully used for partial sequencing of a myosin motor protein in characean rhizoids.

### 4.1.3 Partial sequencing of a characean myosin

The availability of the nucleotide sequence of a characean myosin identified from thallus extracts of *Chara corallina* (Kashiyama et al. 2000) offered the opportunity to determine the sequence of the corresponding homolog in rhizoids of the related species *C. globularis*. In this cell type, myosins interacting with the actin cytoskeleton play a crucial role for gravity-

oriented tip growth by mediating the precise positioning of statoliths and the delivery of SVs (Sievers et al. 1979; 1991b, Hejnowicz and Sievers 1981; Bartnik and Sievers 1988; Braun and Sievers 1993; Buchen et al. 1993; Cai et al. 1997; Braun 1996b, 2002; Braun and Wasteneys 1998b; for review see Braun and Limbach 2005a). The class XI myosin from *C. corallina* (CCM) – a large protein with a length of 2182 aa – is implicated in cytoplasmic streaming. It contains characteristic domains (Fig. 10) that are well known from plant myosins of other classes (Yamamoto et al. 1999; Reddy and Day 2001): The N-terminal head domain of the motor protein includes the highly conserved binding site for ATP which is hydrolyzed during the power stroke. The neck domain comprises six IQ motifs, the putative light chain binding sites. The coiled-coil structure of the myosin tail is characterized by highly conserved 33 aa tandem-repeats, and the C-terminal globular domain is responsible for the specific interaction of the protein with binding partners.

In order to identify the class XI myosin in characean rhizoids, the first step of PCR amplification was performed using a set of primers that bound within the tail domain of CCM. Subsequently, a large region of the myosin gene from *C. globularis* was determined by 5'RACE-PCR. This sequence comprises parts of the coiled-coil domain, six IQ motives and a part of the head domain. Although some variation was observed in the nucleotide sequences, the amino acid sequences of CCM and of the *C. globularis* protein were strongly homologous and the molecular structure of the proteins was coincident.

The partial sequencing of a class XI myosin from *C. globularis* is the first time that a protein which is regarded as a keyplayer of gravity sensing and gravitropic tip growth has been identified and partially characterized at the molecular level in characean rhizoids. This work establishes the basis for investigating the manifold functions and transport pathways that are attributed to myosins in the Chara rhizoid by a systematic molecular characterization of the different protein isoforms. When regions of the less conserved neck and tail domains of the myosins are PCR-amplified by using a degenerate forward primer binding within the highly conserved head domain of myosins and random primers as reverse primers, different myosin isoforms are represented by their specific PCR products which can be distinguished by size and nucleotide sequence. Starting with these random PCR products, the protein isoforms can be fully sequenced and classified according to their molecular structure and to homologies with myosins from other specimens. This approach would greatly contribute to the understanding of the molecular mechanisms of myosin-mediated transport processes in characean rhizoids.

### 4.1.4 Gravity-modulated gene expression

Cellular signaling depends on the complex interplay of multiple processes affecting either the activity or the abundance of factors that are involved in the signaling pathway. Changes in membrane fluxes are responsible for adjusting the cytoplasmic concentration of various ions, and signaling molecules can be mobilized from intracellular stores and regulated by post-translational modifications. The regulation of gene expression is an additional essential process which contributes to the complex signaling networks by affecting the abundance of signaling molecules. Various methods have been developed to study gene expression patterns that are modulated by specific stimuli in order to identify keyplayers of cellular signaling pathways, e.g. differential display, subtractive hybridization, serial analysis of gene expression (SAGE), and microarrays (Matz and Lukyanov 1998; Lievens et al. 2001). In higher plants, gene expression patterns of gravistimulated plant organs are being analyzed at large scale by microarray applications, and several genes have recently been identified to exhibit distinct changes in their expression levels upon gravistimulation (Kimbrough et al. 2004; R. Hampp, University of Tübingen, Germany, personal communication; K. Palme, University of Freiburg, Germany, personal communication). However, when investigating higher plant organs the collective pattern of gene transcripts of a high number of cells from various tissues is displayed. Therefore, observed changes in the transcript level of certain genes cannot be attributed to specific cell types, and distinct changes occurring at the single cell level may be masked by the signals from other cell types.

For understanding the decisive early mechanisms of gravitropic signaling it is desirable to specifically analyze the gene expression of gravity-sensing cells. However, in higher plants, the statocytes of roots and shoots are located in the center of compact tissues and are therefore difficult to isolate and hardly accessible for single-cell analyses. The extraction of cytosol from single-celled characean rhizoids and protonemata offers the unique opportunity to investigate the specific effects of gravistimulation on gene expression in gravity-sensing cell types without the influence of signals deriving from different tissues. Interpetation of the results of gene expression studies is less complicated in the characean cells as compared to higher plants because all processes of gravity sensing and gravitropic growth are accomplished within the tip region of one single cell, which implicates short and direct mechanisms of gravitropic signaling (Braun and Limbach 2005a). However, cost-intensive large-scale techniques, e.g. microarray technology, are not applicable for studying gravity-modulated gene expression in rhizoids and protonemata since the amount of mRNA that can

be obtained from the characean cells is limited and a background of comprehensive database material of the Chara genome is not available.

In the present study, differential display technology (Liang and Pardee 1992) was used for gene expression analyses in characean rhizoids which provided excellent results in various other plant cell types (e.g. Lievens et al. 2001; Charbit et al. 2004; for review see Yamazaki and Saito 2002). Differential display analysis combines simple and well established methods, requires only small amounts of starting material and allows the simultaneous comparison of several different samples at the same time (Matz and Lukyanov 1998; Lievens et al. 2001; Yamazaki and Saito 2002). The differential display protocol that was used to investigate gravity-modulated gene expression in characean rhizoids was modified after Theisen (2005) and included capillary electrophoresis for the detection of random amplification products. Comparison of the specific fragment patterns in gravistimulated and unstimulated rhizoids allowed the identification of genes that exhibit distinct changes in the transcription rate, and that are therefore likely to be involved in gravitropic signaling.

In general, the pattern of fragments amplified by random-primed PCR was very similar in gravistimulated and unstimulated samples, which underlines the good quality of the mRNA extracts and the suitability of differential display technology for analyzing gene expression patterns in the Chara rhizoid. The criteria for regarding a gene as being differentially expressed upon gravistimulation were very restrictive in order to avoid the isolation of false-positives. Differential expression was only accepted when distinct differences in fluorescence intensity of the corresponding fragment were observed between the compared samples in several parallel experiments and when the differential expression pattern was verified by gene-specific PCR. Some fragments of random-primed PCR, i.e. B07-465, B10-568, and B16-275, pointed to an either up- or down-regulation of the corresponding genes during gravitropic signaling in characean rhizoids but the genes could, so far, not be fully sequenced, and differential expression has not been tested by gene-specific PCR.

For the fragment B16-292, however, indicating an up-regulation of the corresponding gene during gravistimulation, all criteria of differential expression of the gene were met. After full-length sequencing of the coding region, the gene was unambiguously indentified as a glucosyltransferase. These enzymes catalyze the transfer of sugar residues to acceptor molecules, and are known to be involved in CW synthesis as either components of the cellulose synthase complex in the PM or as pectin-synthesizing enzymes in the Golgi apparatus (Egelund et al. 2004; Scheible and Pauly 2004). Ssequence homology within this

class of proteins is relatively low but glucosyltransferases share a common domain organization (Saxena et al. 1995). The newly identified characean protein contains the characteristic domains of glucosyltransferases including the conserved sequence motif QXXRW (Saxena and Brown 1995; Saxena et al. 1995). It is therefore likely that it belongs to the class of processive glucosyltransferases which add a number of sugar residues to the acceptor molecules.

The characean protein exhibits a high level of homology with cellulose synthase-like genes of rice which are specialized glucosyltransferases and important components of the cellulose synthase-multienzyme complex (Hazen et al. 2002; Scheible and Pauly 2004). The enzymes encoded by cellulose synthase-like genes are proposed to synthesize the hemicellulose backbones of plant CWs (Richmond and Sommerville 2000). The up-regulation of the glucosyltransferase gene in characean rhizoids upon gravistimulation indicates that changes in CW properties are likely to be involved in gravitropism of the cell type. Modifications of CW structure or rigidity depending on the activity of glucosyltransferases (Bouton et al. 2002; Orfila et al. 2005) may have crucial function for the gravitropic curvature response of gravistimulated rhizoids. In accordance with this interpretation, the characean glucosyltransferase is rather a target of the gravitropic signaling pathway than a signaling factor. Interestingly, microarray analysis of Arabidopsis root tips revealed a variety of genes encoding CW-modifying enzymes that exhibited significant changes in the transcription rate upon gravistimulation (Kimbrough et al. 2004). For understanding the role of glucosyltransferases in gravitropic growth of characean cells it will be necessary to investigate functional aspects and the intracellular localization of the enzyme. In addition, it will be interesting to analyze the time-course of gene expression at an improved level of temporal resolution and to track the expression level during prolonged gravistimulation.

The molecular studies have demonstrated that great effort is required to characterize characean genes that are differentially expressed due to the lack of genomic information available in databases. In addition, differential display analysis is unlikely to cover all transcripts even if numerous different random primers are used, and rare transcripts may be underrepresented due to low amounts of mRNA. However, the present work has shown that differential display technology is well suited for analyzing gene expression in rhizoids. Using this technique, first proteins were discovered that are involved in signaling pathways of the gravity-sensing characean cell type.

## 4.2 Early mechanisms of gravity sensing

Gene expression analyses have provided new insights into molecular aspects of gravitropic signaling in characean rhizoids and protonemata. The experiments performed under microgravity conditions aimed at specifying functional interactions of some of the keyplayers of gravity sensing. In higher plants, there is considerable progress in the understanding of cellular, physiological, and molecular processes of gravitropic response mechanisms (Boonsirichai et al. 2002; Sievers et al. 2002; Blancaflor and Masson 2003), but little is known about the molecular mechanisms being involved in the early steps of gravity sensing (Kiss 2000; Morita and Tasaka 2004). The major problem for addressing these questions in higher plants is the fact that gravity-sensing statocytes are located within a compact tissue that is not easily accessible for microscopic or molecular applications. In characean rhizoids and protonemata the statoliths which are responsible for gravity susception as well as for the initiation of gravitropic signaling can easily be observed by light microscopy, and gravitropic curvature is directly related to the activity of the gravireceptors in the same cell. These properties of the characean cell types were essential criteria when designing the experiments that were conducted under microgravity conditions provided by parabolic flights of the MAXUS-5 sounding rocket and of the A300 Zero-G aircraft.

### 4.2.1 Statolith-cytoskeleton interactions determining the threshold level of gravisensitivity

Whereas in most cell types gravity does not affect the position or movement of organelles, gravity-sensing statocytes allow their statoliths to sediment along the gravity vector. There are several reports indicating that the actomyosin system is involved in the positioning of statoliths and in the modulation of the sedimentation process in higher plant statocytes in order to meet specific requirements for a most beneficial gravitropic response (Sievers et al. 1991a; Volkmann et al. 1991, 1999; Driss-Ecole et al. 2000; Perbal et al. 2004). Although the kinetics of statolith movements have been analyzed in gravisensing cells of shoots (Sack et al. 1984; Saito et al. 2005) and roots (Sack et al. 1985, 1986; MacCleery and Kiss 1999; Yoder et al. 2001), interpretation of the results with respect to gravity sensing is difficult because the interactions between statoliths and the cytoskeleton and their role in the graviperception mechanism are far from being understood in these cell types.

Therefore, characean rhizoids and protonemata were used to determine the minimum acceleration level required for lateral statolith displacement, which is the prerequisite for gravity susception to occur. Structural and functional details of the actin cytoskeleton are well described in these single-celled model systems for gravitropism research (Braun and Wasteneys 1998b; Braun et al. 2004) and the specific function of actomyosin forces in the process of gravity sensing is well understood (Braun 2002; Braun et al. 2002). It has been shown that, whenever statoliths are displaced laterally by sufficiently high accelerations, it is only a matter of time until they settle on the gravisensitive membrane region where perception will inevitably take place followed by the graviresponse (Braun 2002). Since the gravitropic signalling pathway is short and is not complicated further by complex signal transduction and transmission pathways like in higher plant tissues, it is easy to discriminate between susception and perception, and interfering with these mechanisms is quickly reflected in a modulation of the response, i.e. the reorientation of the cell tip.

Based upon this knowledge, the threshold acceleration level required for lateral statolith displacement was experimentally determined in order to specify physical and energetic aspects of molecular interactions between statoliths and the cytoskeleton underlying the primary phase of gravity sensing. Lateral centrifugation of rhizoids during the microgravity phase of sounding rocket flights was shown to induce statolith displacement at an acceleration level of 0.14*g* but not 0.05*g*. Similar results were obtained from protonemata. Given a threshold value of lateral statolith displacement of 0.14*g* ($a = 1.37$ m s$^{-2}$), the statolith volume V (statolith diameter 2 µm), statolith density ($\rho_{statolith} = \rho_{barium\ sulfate} = 4.5$ g cm$^{-3}$) and cytoplasmic density ($\rho_{cytoplasm} = 1.03$ g cm$^{-3}$), the force F that has to be exceeded by any acceleration stimulus in order to move a single statolith towards the cell flank can be calculated to be in a range of:

$$F = \Delta\rho_{(statolith - cytoplasm)} \times V \times a = 1.99 \times 10^{-14}\ \text{N}.$$

This value represents the dimension of cytoskeletal forces restricting the lateral displacement of statoliths. Experiments in microgravity (Volkmann et al. 1991; Buchen et al. 1993; Braun et al. 2002) and in simulated weightlessness (Cai et al. 1997; Braun et al. 2002) have shown that in a tip-downward growing rhizoid actomyosin forces keep statoliths in their dynamically stable resting position by exactly compensating the apically directed gravity force (the statoliths' weight). From this, it follows that the actomyosin forces acting on a statolith in basal direction to prevent statoliths from settling into the tip are in a range of 1*g,* which is about one order of magnitude higher than the forces that restrict lateral displacement of

statoliths. Due to this principle, statoliths are able to sediment towards the lower cell flank upon gravistimulation and, thus, to fulfill their role as susceptors of the gravity vector.

Considering an average distance between a statolith and the PM (distance between median cell axis and PM, s = 15 µm), the mechanical work W that is necessary to complete sedimentation of a statolith onto the graviperception site at the threshold acceleration level can be calculated:

$$W = F \times s = 2.98 \times 10^{-19} \text{ J}.$$

This value represents the minimal energy required for gravity susception in characean rhizoids and protonemata to occur. Although this energy value matches the theoretically calculated minimal energy required for the activation of a gravireceptor (Björkman 1988), it is, however, not relevant for characterizing graviperception in the characean cells. The parabolic flight experiments described in this study demonstrate that gravireceptor activation does not depend on the mechanical work that is provided by the gravity-induced statolith sedimentation process but on direct interaction of sedimented statoliths with the membrane-bound gravireceptor (see 4.2.2).

Since any acceleration stimuli which exceed the above mentioned threshold forces and deviate from the cell axis lead to sedimentation of statoliths followed by gravity perception and the gravitropic response, the threshold acceleration gives a good approximation of the general threshold of gravisensitivity in characean rhizoids and protonemata. A threshold value of 0.14*g* is in the same range as was determined by microgravity experiments for other gravisensitive cell types, i.e. ciliates (Hemmersbach et al. 1996), flagellates (Häder et al. 1995) and higher plant statocytes (Brown et al. 1995). In conclusion, the mechanisms of gravity sensing might be overbuilt (Björkman 1988; Sack 1997), however, only a high sensitivity ensures that the sensing system can operate efficiently and can correct even the smallest deviations from the gravitropic set-point angle.

### 4.2.2 Gravireceptor activation in characean rhizoids

The gravireceptor molecules in characean rhizoids which are responsible for the initiation of the gravitropic signaling pathway are located at a confined belt-like region of the PM 10 – 35 µm from the cell tip. So far, the mechanisms leading to an activation of the receptors after sedimentation of statoliths has been completed were unclear. Receptor activation could either be based upon the pressure that is exerted by the weight of statoliths or on interactions with

components of the statolith surface that are independent of the statoliths' weight. In this study, the functional mechanism of receptor activation in characean rhizoids was analyzed by investigating if sedimented statoliths were able to activate the gravireceptor even when they were weightless during the microgravity phases of parabolic plane flights. Control experiments on ground revealed that the parabolic flight profile with its alternating acceleration levels was excellently suited to study the specific impact of microgravity on graviperception by analyzing the gravitropic curvature responses of rhizoids.

#### 4.2.2.1 Ground control experiments

The results showing that intermittent centrifugation at 2*g* as well as extended hyper-*g* centrifugation of rhizoids did not alter the gravitropic curvature response, provide clear evidence that enhancing the pressure on the gravisensitive PM by increasing the weight of fully sedimented statoliths does not modulate graviperception and does not affect the graviresponse. Consequently, the hypergravity phases of the parabolic flight profile could be neglected when analyzing the effect of microgravity.

Inversion experiments on ground demonstrated that intermittent removal of statoliths from the gravisensitive plasma-membrane of gravistimulated rhizoids for only 10 s resulted in a decrease of curvature angles. Inverting cells for 5 s had no significant effect on gravitropic curvature. However, high-magnification video microscopy confirmed that 5 s after inversion of gravistimulated cells statoliths were completely removed from the PM. It can be concluded from the inversion experiments that the gravireceptor in characean rhizoids is quickly deactivated with a lag time of a few seconds when the contact between statoliths and the PM is interrupted. Thus, if receptor activation is affected in microgravity, this effect should be detectable by comparing curvature angles of flight samples and in-flight controls, although the duration of a single microgravity phase is only 22 s.

#### 4.2.2.2 Parabolic plane flight experiments

Microscopic observation of flight samples indicated that the statolith complex was not lifted from the PM during the different acceleration levels of the parabolic flight profile. Thus, a removal of statoliths from the graviperception site and a disruption of contact between statoliths and the PM could be ruled out, and weightlessness of the statoliths was the only

parameter analyzed with the experimental setup. Therefore, the results obtained from the parabolic flight experiments provide a stringent line of evidence and interpretation. In none of the parabolic flight experiments a difference of final curvature angles between flight samples and in-flight controls was observed indicating that gravity perception was not interrupted during the microgravity phases. The experiment demonstrates that even weightless statoliths were capable of activating the gravireceptor. Taking into account that increasing the weight of statoliths by centrifugation did not affect gravitropic curvature (see 4.2.2.1), it can be excluded that the gravireceptor in characean rhizoids is a mechanoreceptor, e.g. a stretch-activated ion channel, which is activated by tension or pressure exerted by sedimented statoliths. The inversion experiments on ground and the microgravity experiments confirmed that close contact of statoliths with the gravisensitive PM is the determinant for graviperception. Even short-term removal of statoliths from the PM strongly impaired gravitropic curvature. The gravireceptor in characean rhizoids is, therefore, characterized and referred to as a contact receptor.

At the resolution level of microscopic observation during the microgravity experiments some cellular particles could not unequivocally be identified as statoliths, and due to the three-dimensional shape of the tube-like cells it was impossible by means of two-dimensional image records to decide whether a statolith was in contact with the PM or not. Although video microscopy of rhizoids that were laterally centrifuged with 0.14*g* during the microgravity phase of the MAXUS-5 sounding rocket flight allowed to spatiotemporally resolve the acceleration-induced lateral displacement of statoliths, it was not intended for identifying contacts of single statoliths with the PM. However, since these living cells exhibited distinct curvature responses, it is concluded that statoliths have sporadically settled on the gravisensitive membrane site of the centrifugal flank where they initiated the gravitropic signalling pathway. This assumption is confirmed by the analysis of chemically fixed rhizoids underlining the settlement of statoliths onto the lateral cell flank at the end of centrifugation in microgravity. In vertically downward growing rhizoids on ground, statoliths are symmetrically distributed across the cell diameter and some statoliths are found in close proximity to the PM at both cell flanks. However, it cannot definitely be decided whether statoliths are in contact with the PM at both flanks generating a symmetric gravitropic signal or whether they are located close to the membrane without being in contact with the membrane-bound gravireceptors so that gravitropic signalling is not initiated at all.

A contact-dependent mechanism of gravireceptor activation in characean rhizoids is supported by previous experiments in which tip-reorientation in vertically downward growing rhizoids could only be induced when statoliths were brought into contact with the gravisensitive area of the PM by laser-tweezers micromanipulation (Braun 2002). Stretching the gravisensitive membrane from the outside by using a microcapillary does not provoke a curvature response (C. Limbach and M. Braun, unpublished results). Further centrifugation studies have shown that the graviresponse of characean protonemata also relies on the gravity-induced and actin-mediated settlement of statoliths on a gravisensitive PM area and cannot be promoted by acceleration forces (Hodick and Sievers 1998).

Until today, functional mechanisms of graviperception have not been unequivocally determined in higher plants. Gravireceptor proteins are commonly addressed as mechanosensitive receptors. Models of gravity sensing including the tensegrity model (Zheng and Staehelin 2001) postulated that receptor activation depends on mechanical forces (tension, pressure) which are generated by the gravity-driven sedimentation of statoliths and are transferred to stretch-activated ion channels (gravireceptors) via actin-dependent mechanisms (for reviews see Sievers et al. 2002; Boonsirichai et al. 2002; Perbal and Driss-Ecole 2003; Blancaflor and Masson 2003). Even though a crucial role of actin in the early signal transduction pathway is appealing, physiological and cytological studies including inhibitor treatments have so far only come to contradictory results (Blancaflor and Hasenstein 1997; Nick et al. 1997; Yamamoto and Kiss 2002; Friedman et al. 2003; Hou et al. 2003, 2004), leaving the mechanisms of gravity perception in higher plants enigmatic.

Parabolic flight experiments presented in this study have significantly enhanced our understanding of the molecular interactions which restrict gravity susception and mediate gravity perception in characean rhizoids and protonemata. The results encourage further utilization of the parabolic flight profile with its sequence of short-term microgravity phases as a powerful instrument that complements physiological, biochemical and genetic approaches and promises to contribute to the clarification of the early mechanisms of gravity sensing in higher plants.

## 4.3 High-pressure freeze fixation, freeze substitution and 3D dual-axis tomography – innovative tools for ultrastructural research in characean rhizoids

For understanding the mechanisms of gravity sensing and tip growth in characean rhizoids and protonemata, the identification of the participating molecules and molecular interactions is one important task. However, the specific functions of these cellular components can only be fully understood by integrating the structural arrangement of the cells. Therefore, protocols for high-pressure freezing, freeze substitution and 3D dual-axis tomography of characean rhizoids have been developed and optimized in the present study in order to analyze the cellular ultrastructure at a maximum level of resolution. The ultrastructure of rhizoids has been studied in great detail for more than 40 years by using chemical fixation (Sievers 1965, 1967a, 1967b; Bartnik 1998; Noecker 2000). It is, however, generally accepted that chemical fixation causes serious artifacts which impair ultrastructural examinations, and which can be avoided by using cryofixation (Gilkey and Staehelin 1986; Dahl and Staehelin 1989; Staehelin et al. 1990; Studer et al. 1992). Freeze fixation improves the structural preservation of electron microscopical samples because it warrants the fast and simultaneous fixation of all cellular components whereas chemical fixation acts relatively slowly and differently on the various classes of cellular molecules allowing structural alterations during the fixation process. It was therefore reasonable to re-evaluate the ultrastructure of the growth-organizing apical cell region of characean rhizoids in samples prepared by high-pressure freeze fixation. This cryofixation technique was specifically developed for the fixation of bulky biological specimens since strong gradients in the freezing quality were observed when conventional methods of freeze fixation were used, e.g. plunge freezing, cold metal block freezing, propane jet-freezing etc. (Gilkey and Staehlin 1986; Dahl and Staehelin 1989). By applying high pressure (2100 bar) during cryofixation, the modified jet-freezing technique has been reported to provide optimal vitrification of the cytoplasm without the formation of ice crystals in specimens with a thickness of up to 200 – 300 µm (Moor 1987; Gilkey and Staehelin 1986; Dahl and Staehelin 1989; Studer et al. 1989; Monaghan et al. 1998).

So far, only one study reports the use of cryofixation for ultrastructural examinations in the Chara rhizoid (Kiss and Staehelin 1993). However, this study is far from being a systematic analysis of the cellular ultrastructure since a limited number of electron micrographs shows only some cellular details. In addition, the authors reported difficulties in handling the rhizoid

samples for cryofixation and severe mechanical damages. It is therefore difficult to assess the overall quality of ultrastructural preservation.

In the present study, 3D dual-axis electron tomography (Mastronarde 1997) was used for ultrastructural analyses of high-pressure frozen rhizoids. This innovative technique has been developed at the University of Colorado and has provided substantial progress in the detection and visualization of the cellular ultrastructure. The alignment and backprojection of electron microscopic image series taken at increasing tilt angles of the section about two orthogonal axes provides a set of tomographic slices (Mastronarde 1997). Thereby, the resolution level in z-direction is drastically reduced to the range of a few nanometers, which allows to study ultrastructural details at the molecular level. In addition, the tomograms provide three-dimensional information about the arrangement and distribution of cellular structures which can be modeled using specific software, such as the IMOD software package (Mastronarde 1997) that is available for free download at the IMOD home page (URL: http:// bio3d.colorado.edu/imod/). As has been shown in various studies, electron tomography and three-dimensional modeling provided completely new insights into ultrastructural and functional characteristics of cellular compartments and macromolecules (e.g. Ladinsky et al. 1999; Otegui and Staehelin 2000, 2004; Otegui et al. 2001; Seguí-Simarro et al. 2004; Austin et al. 2005; Kürner et al. 2005; Nicastro et al. 2005; Seguí-Simarro and Staehelin 2005).

The combined use of high-pressure freeze fixation for sample preparation and 3D electron tomography as imaging technique allowed a systematic re-evaluation of the ultrastructure of characean rhizoids and provided fascinating and surprising new results. The characterization of the different vesicle types and the detailed description of their distribution in the cell apex as well as the identification of an extensive subapical vacuolar reticulum clarify some crucial aspects of gravity-oriented tip growth but also raise new questions about the functional relationship of cellular compartments. As discussed below, the results gathered by high-resolution ultrastructural analyses of characean rhizoids have considerable implications for the understanding of the structural and cellular organization underlying plant tip growth since similar cell types, e.g. pollen tubes and root hairs, have so far only been investigated by conventional electron microscopy.

### 4.3.1 Ultrastructural preservation of high-pressure frozen rhizoids

High-pressure frozen rhizoids exhibited the general ultrastructural characteristics of cryofixed samples that were observed in a variety of plant specimens (Gilkey and Staehelin 1986; Dahl and Staehelin 1989; Studer et al. 1989; Kiss et al. 1990; Studer et al. 1992; Roy et al. 1997). The cytoplasm was homogeneous without being aggregated or clumped and no ice crystals were observed to perturb the cellular ultrastructure. The strongly contrasted membranes were smooth and not undulating, and the three contours of the lipid bilayer were widely detectable. Cellular organelles and membrane-encircled compartments were not found to be shrunken or swollen.

Golgi stacks exhibited strong cis to trans polarity regarding luminal width and electron density of the cisternae. Budding profiles of COP-vesicles were identified at medial and cis cisternae which are implicated in transport mechanisms within Golgi stacks and between Golgi stacks and the ER (Staehelin and Moore 1995; Robinson et al. 1998a; Nebenführ 2002; Ritzenthaler et al. 2002). The detection of newly forming cisternae at the cis side of the Golgi stacks supports the cisternal progression model of Golgi maturation (Morré 1987; Staehelin and Moore 1995).

Most prominently, the PM exhibited smooth contours and was found to be closely attached to the inner layer of the CW. In chemically fixed rhizoids, the undulating shape of the PM and detachment from the CW (Sievers 1965, 1967a, 1967b; Bartnik 1984; Bartnik and Sievers 1988; Noecker 2000) were major artifacts that hampered investigations of ultrastructural features being related to the mechanisms of cell growth at the apical membrane domain.

#### 4.3.1.1 Apical plasma membrane

In high-pressure frozen rhizoids, the apical PM was irregularly shaped and exhibited prominent invaginations into the cytoplasm and protuberances into the CW, which reflects the high rate of membrane turn-over at the rapidly expanding cell tip. The tubular invaginations were not detectable by conventional EM of thin sections but clearly identified and modeled in electron tomograms. The observations indicate that the apical PM of rhizoids may comprise distinct domains with characteristic shapes and specific functions for tip growth.

It is unlikely that the invaginations of the PM represent artifacts caused by plasmolytic effects of the cryoprotectant. Sucrose, which was used in this study, is a well established

cryoprotectant for freeze fixation that efficiently inhibits the formation of ice crystals in the cytoplasm without affecting structure and metabolism of the samples (Ding et al. 1992; Otegui et al. 2001; Zheng and Staehelin 2001; Murata et al. 2002). In rhizoids, no effect on cell growth and morphology was detected at the light microscopic level when sucrose was applied in the concentration used for high-pressure freezing. Electron microscopic observation revealed that the PM was attached to the inner layer of the CW, and in none of the samples, free space was observed between the CW and the PM which would indicate plasmolytic detachment of the membrane. Also, at the tubular invaginations the PM was attached to the CW without any gaps being detected. When rhizoid samples were processed with mannitol as cryoprotectant the overall ultrastructural preservation was slightly poorer whereas the shape of the PM was identical to the samples that were prepared with sucrose. To ultimately discover artifactual alterations that might be caused by the application of cryoprotectants the use of non-osmotically active reagents, e.g. 1-hexadecene (Studer et al. 1992; Monaghan et al. 1998; Walther and Ziegler 2002; Hess 2003) or dextran (Kiss et al. 1990; Roy et al. 1997) is alternatively recommended. However, since these substances may cause different artifacts (Kiss et al. 1990), a careful comparison of samples prepared with different cryoprotectants is necessary to rule out any fixation artifacts. The use of cryoprotectants for cryofixation of biological samples is generally recommended because these reagents not only prevent the formation of ice crystals but also ensure a good transfer of heat and pressure, and they replace air from the specimen chamber that might collapse during fixation causing mechanical damage (Gilkey and Staehelin 1986).

#### 4.3.1.2 Endoplasmic reticulum

As reported from various cryofixed samples (Walther and Ziegler 2002; Giddings 2003; Andrew L. Staehelin, University of Colorado, Boulder, USA, personal communication), the membranes of the ER exhibited very faint contrast also in high-pressure frozen rhizoids. In chemically fixed samples ER cisternae were characterized by darkly stained membranes, and the apical ER aggregate was one of the most prominent structures in the rhizoid (Bartnik 1984; Bartnik and Sievers 1988; Braun 2001). For unraveling the role of the ER aggregate for the regulation of tip growth it is essential to elucidate its structural organization by analyzing the three-dimensional arrangement of the aggregated cisternae. However, tracking and modeling of the short and winded cisternae of the ER aggregate was not feasible in high-pressure frozen rhizoid samples since membranes were undetectable and cisternae could only

be determined by the parallel rows of ribosomes at the cytoplasmic interface. For the visualization of the ER aggregate allowing subsequent 3D-remodeling of the cisternae, the freeze substitution protocol for cryofixed rhizoids needs to be modified. It is a striking observation of the present study that the samples for immuno-electron microscopy that were prepared by freeze substitution with 0.25% GA and 0.1% UA and were embedded in Lowicryl HM20 exhibited stronger contrast of the ER membranes as compared to the samples that were processed for ultrastructural studies. Similar findings are reported from yeast cells (Giddings 2003). Additional protocols that were shown to improve the visualization of membranes in cryofixed samples, e.g. substitution with 0.1% potassium permanganate in acetone (Giddings 2003) or addition of 1 to 5% water to the substitution medium (Walther and Ziegler 2002) may also be suited to enhance the membrane contrast of ER cisternae in rhizoids and to make a 3D-reconstruction of the ER aggregate possible.

#### 4.3.1.3 Actin microfilaments

The high quality of ultrastructural preservation in high-pressure frozen and freeze-substituted rhizoids is highlighted by the detection of actin in electron tomograms as well as by immuno-electron microscopy. Many studies have aimed at visualizing the actin cytoskeleton in electron microscopic samples of tip-growing cells where actin plays a major role for the regulation of polarized growth (Lancelle and Hepler 1989; Lichtscheidl et al. 1990; Ding et al. 1992; Miller et al. 1996; Roy et al. 1997; Geitmann und Emons 2000; Derksen et al. 2002). However, the actin microfilament system proved to be highly sensitive to the fixation conditions. It could not be preserved by chemical fixation and was only partly detectable in cryofixed samples (Ding et al. 1992; Lancelle and Hepler 1989; Lichtscheidl et al. 1990; Miller et al. 1996; Geitmann and Emons 2000; Derksen et al. 2002). Detailed electron microscopic analyses of cellular actin arrays which are essential for completing the knowledge of the role of the actin cytoskeleton for tip growth are still missing.

In the present study, bundles of actin microfilaments were immunolocalized in the subapical region of rhizoids. Specific labeling was observed at confined regions where actin was present at the surface of the thin sections and therefore accessible to the antibody whereas actin structures in the interior of the section could not be labeled. The immunolabeling of longitudinally oriented microfilament bundles in the subapical region of electron microscopic samples fits well to the appearance of the actin network in this cell region after fluorescence

staining (Braun and Wasteneys 1998b). In the cell apex, fluorescence labeling showed a fine network of actin microfilament bundles that focused into a prominent actin patch in the center of the Spitzenkoerper (Braun and Wasteneys 1998b; Braun et al. 2004). However, in high-pressure frozen samples of rhizoids no actin-labeling was observed in the apical cell region. Obviously, immuno-electron microscopy revealed only the relatively stable bundles of actin microfilaments in the subapical region but failed to detect the fine filaments in the apical cell region which are dynamically remodeled by the concerted action of actin-binding proteins (Braun et al. 2004; Braun and Limbach 2005c). Similar results of actin immunolabeling experiments are reported from cryofixed pollen tubes where only the thick actin bundles in the subapical region were labeled whereas the fine microfilament network in the apical region was not decorated (Lancelle and Hepler 1989; Lichtscheidl et al. 1990).

In addition to the identification of actin microfilament bundles in cryofixed characean rhizoids by immuno-electron microscopy, actin was frequently observed in electron tomograms of the cell apex, predominantly in the region of the ER aggregate. 3D-modeling of the apical actin array proved difficult since filaments were very fine and short, and could therefore not be tracked in the tomograms. Actin in the apical region of cryofixed rhizoids was not as abundant as anticipated based upon fluorescence labeling (Braun and Wasteneys 1998b), which indicates that parts of the actin array were either not visible or degraded during processing of the samples. For improving the visualization of actin microfilaments in cryofixed samples, Murata et al. (2002) propose a preparation protocol using a combination of staining with $OsO_4$ at 40° C and 5% uranyl acetate. Sine this procedure enhances at the same time the contrast of intracellular membranes (Murata et al. 2002) it may be useful for studying the structural interrelation of the ER aggregate and the actin array in the apical region of characean rhizoids. Although the present study does not comprise a complete description of the actin arrangement in the rhizoid tip, the preservation and visualization of the actin cytoskeleton has been substantially improved. Further insights into the cytoskeletal basis of the structural cellular organization are expected from additional electron microscopic studies using slightly modified protocols of freeze substitution.

### 4.3.2 Characterization and distribution of vesicles in the apex of rhizoids

In characean rhizoids and protonemata cell growth is confined to the apical cell region and mediated by the localized exocytosis of SVs, which requires high rates of vesicle and membrane turn-over. Several electron microscopic studies were aimed at specifying the different types of vesicles and their corresponding distribution in chemically fixed samples (Sievers 1965, 1967a, 1967b; Bartnik 1984; Bartnik 1990) as well as in cryofixed cells (Kiss and Staehelin; 2003) in order to elucidate mechanisms of vesicle trafficking that mediate gravity-oriented growth. Due to the limited resolution of the electron microscopic analyses in these studies, vesicles could only be classified by their size and by the electron density of the contents leading to incomplete and partly contradictory results.

Therefore, high-resolution electron tomography of high-pressure frozen samples was used for a detailed description of the vesicle types present in the Chara rhizoid and for the analysis of their subcellular distribution in the apical cell region with regard to their roles for tip growth and gravitropic reorientation. Five vesicle types were identified and characterized by vesicle size, membrane properties, electron density of the contents and protein coats. Two types of coated vesicles were determined that had not been detected in any of the previous studies, which underlines the high quality of the high-pressure frozen samples and the significance of electron tomography for ultrastructural research. Since vesicle distribution has not been analyzed in any tip-growing cell type at a similar level of resolution before, the results of this study provide considerable progress in the understanding of vesicle trafficking in tip-growing plant cells. A schematic reconstruction of vesicle distribution in the apical cytoplasm of characean rhizoids based upon the findings of electron tomographic analyses is shown in Fig. 31.

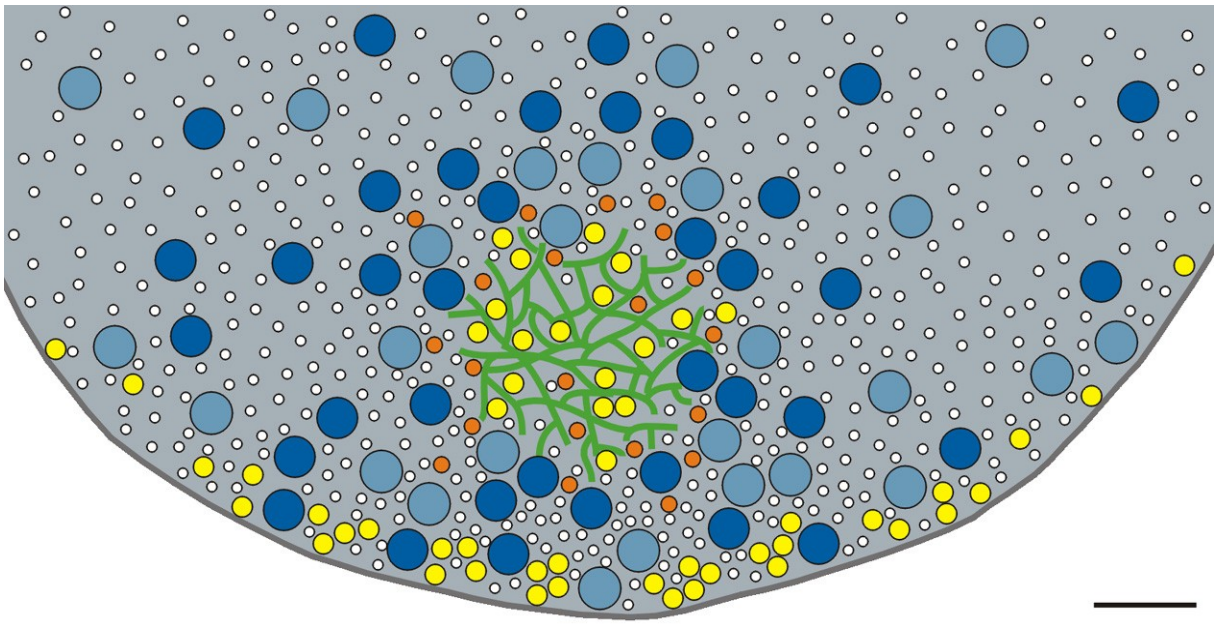

**Fig. 31** *Schematic reconstruction of the distribution of different vesicle types in the apex of rhizoids*
The model combines the results of the electron tomographic analyses of this study (see 3.3.4) and gives an overview of the distribution of all vesicle types identified in the apical cytoplasm of high-pressure frozen rhizoids. The distribution patterns are discussed in detail in the text.
Color coding: light blue: LVs, dark blue: DVs, yellow: CCVs, orange: CVs, white: MVs, green: cisternae of the ER aggregate, grey: PM. Bar: 500 nm

#### 4.3.2.1 Secretory vesicles

When analyzing the ultrastructure of high-pressure frozen rhizoids, large vesicles with a diameter of about 200 nm were the most prominent structures in the apical cell region. Based upon specific ultrastructural differences two distinct groups of large vesicles were distinguished: dark vesicles (DVs) that were characterized by electron dense contents and by a strongly stained membrane were slightly but significantly smaller than the light vesicles (LV) with less electron dense contents and a thin, faintly stained membrane. Previously, Kiss and Staehelin (1993) already discriminated two types of large vesicles in cryofixed rhizoids by the electron density of their contents. However, DVs were reported to be slightly larger than LVs, which is in contradiction to the observations of the present study. Based upon differences in the staining of large vesicles in chemically fixed samples, Bartnik et al. (1990) suggested that diverse contrast levels represent different stages of vesicles during their shuttle-like movements between the ER aggregate and the apical PM. The striking differences that were observed in the present study regarding not only electron density but also vesicle size and membrane properties, however, provide strong evidence that the large vesicles in characean rhizoids should be grouped into two different classes.

Several observations support the idea that the DVs function as SVs. The distribution of large vesicles in high-pressure frozen samples (Fig. 31) is well in accordance with the accumulation of SVs in the apical region of rhizoids that has previously been described (Sievers 1965, 1967a; Bartnik and Sievers 1988; Bartnik et al. 1990; Kiss and Staehelin 1993). In addition, esterified pectins that are designated for exocytosis have been immunolocalized to DVs with a diameter of approx. 200 nm using JIM 7 antibody (Kiss and Staehelin 1993). Most importantly, the DVs were observed in the present study to share characteristic features, i.e. electron density and membrane properties, with vesicles budding from the sites of SV formation at the trans Golgi cisternae.

The nature of LVs in the apical region of rhizoids is less clear. Based upon their size, the distribution pattern in the apical cytoplasm and positive labeling with the JIM 7 antibody (Kiss and Staehelin 1993), they should be regarded as a second type of SVs that contains material with a differing composition as compared to DVs causing the faint staining in electron microscopic samples. This interpretation is in contrast to electron microscopic observations in pollen tubes where a single type of SVs was identified (Derksen et al. 2002). The appearance of the membrane of LVs in the Chara rhizoid, however, wich is much thinner than those of other vesicle types and may represent a single layer of phospholipids rather than a complete lipid bilayer, raises the question of whether these structures are real vesicles. Lipid monolayers are known to surround lipid storage compartments that exhibit similar appearance in electron microscopic samples as the light structures in the rhizoid. In higher plants, oil bodies with a diameter in the range of 0.2 to 2 μm comprise a matrix of triacylglycerides which is encircled by a lipid monolayer (Tzen et al. 1993; Frandsen et al 2001). Interestingly, caleosin – a characteristic protein of oil bodies in higher plants (Chen et al. 1999) – has previously been detected in protein extracts of characean rhizoids (Limbach 2002). However, assuming that the large light particles that were detected in electron microscopic samples of characean rhizoids are oil bodies is speculation, and the putative role of lipid storage compartments in the Chara rhizoid is unclear. Clarification of the nature of the LVs is expected from comprehensive immunolabeling experiments. In addition, the presence of oil bodies in the Chara rhizoid can be tested by differential cell fractionation which should allow the isolation of lipid components from cytosolic extracts due to their low density.

The accumulation of large vesicles around the ER aggregate in the Spitzenkoerper center of high-pressure frozen rhizoids (Fig. 31) is in accordance with previous electron and light microscopic observations (Bartnik and Sievers 1988; Bartnik et al. 1990; Kiss and Staehelin

1993) and supports a role of the ER complex in vesicle trafficking. Although the details of this function are not well understood interactions between SVs and ER cisternae are likely to be accomplished at the periphery of the ER aggregate since large vesicles were excluded from central regions of the complex (Fig. 31; Bartnik and Sievers 1988). The vesicle accumulation in the apical cytoplasm may also be reflected by in-vivo staining with FM dyes which occasionally produced bright, ring-shaped fluorescence surrounding the ER aggregate whereas the rest of the cytoplasm was homogeneously stained.

As demonstrated in the present study, the density of SVs in the cytoplasm flanking the PM of the apical region decreases from the cell tip towards the flanks (Fig. 31), thereby reflecting the gradient in the rate of cell extension (Hejnowicz et al. 1977). However, within the cytoplasm of the outermost tip region, SVs were evenly distributed and no vesicle clusters were observed, which coincides with observations from cryofixed pollen tubes (Derksen et al. 2002). These results indicate that exocytosis in tip-growing cells is not confined to specialized membrane domains but rather accomplished over the entire membrane area of the tip.

#### 4.3.2.2 Microvesicles

Small vesicles with a diameter of 25 nm exhibit the highest vesicle density (up to 420 vesicles per $\mu m^3$) of all vesicle types identified in the apical region of high-pressure frozen rhizoids. They were found to be concentrated in the cytoplasm surrounding the ER aggregate but evenly distributed between the ER complex and the cell tip (Fig. 31). Small vesicles have been reported from previous electron microscopic studies of chemically fixed rhizoids (Sievers 1965, 1967a; Bartnik and Sievers 1988; Kiss and Staehelin 1993) and were referred to as microvesicles. However, in these studies the vesicle size was overestimated (diameter 40 – 50 nm), which is attributed to poor ultrastructural preservation of the samples and to the limited resolution of conventional electron microscopy. Sievers (1965) proposed a role of these MVs in exocytotic processes; however, clear evidence for the function of this vesicle type in the Chara rhizoid and in other tip-growing cell types is lacking. Based upon the identification of CCVs in the present study (see 4.3.2.3) it may be possible that the microvesicles represent a stage of endocytotic vesicles after disassembly of the clathrin coat.

#### 4.3.2.3 Clathrin-coated vesicles

Electron tomography of high-pressure frozen rhizoids provided unambiguous evidence that CCVs are present in the apical cell region. This vesicle type has not been identified in previous studies (Sievers 1965, 1967b; Bartnik and Sievers 1988; Kiss and Staehelin 1993) and was hardly detectable by conventional electron microscopy in the present study due to the limited resolution level of the applied imaging techniques. It is noteworthy, however, that CCVs at the PM of chemically fixed rhizoids were already shown by Sievers (1967a) but taken as microvesicles with strongly contrasted coats ('Mikrovesikel mit kontrastreichem Hof'). In the present study, the prominent coats of the CCVs were easily discovered in single slices of electron tomograms. The spherical clathrin scaffold is characterized by the regular arrangement of pentagons and hexagons that are formed by numerous clathrin triskelions, each consisting of three heavy chains and three light chains (Robinson 1996; Robinson et al. 1998a; Holstein 2002). The clathrin lattice is connected to the vesicle membrane by various adapter proteins that are responsible for the recruitment of clathrin molecules and for the interaction with membrane-bound receptor proteins (Holstein 2005).

The CCVs detected in this study have a diameter of about 30 nm with the clathrin scaffold forming a cage of ~ 90 nm in diameter, which is in accordance with the overall size of CCVs in other plant cell types that was reported to be in a range of 75 – 100 nm (Robertson and Lyttleton 1982; Tanchak et al. 1984; Emons and Traas 1986; Derksen et al. 1995; Robinson et al. 1998b; Šamaj et al. 2004). However, in most of these studies the vesicle diameters were estimated to be significantly larger than in characean rhizoids because protein coats were observed to be relatively thin. Only Robertson and Lyttleton (1982) determined values of vesicle size (diameter 26 to 51 nm) and coat thickness (21 to 31 nm) for CCVs in root hairs of white clover that were similar to those in characean rhizoids. It cannot ultimately be clarified whether CCVs in rhizoids possess thicker protein coats as compared to other plant cell types or whether the diameter of the vesicles was overestimated in previous studies due to poor ultrastructural preservation of the samples and limited resolution of conventional electron microscopy. However, the excellent quality of the high-pressure frozen samples and the improved resolution of electron tomography strongly implicate that the measurements in rhizoids are very precise and recommend the use of these techniques for re-evaluating the size of CCVs in other cell types.

As revealed by electron microscopic analyses, two populations of CCVs exist in the apical cytoplasm of characean rhizoids that are separated from each other by a broad cytoplasmic region of about 1 µm where vesicles of this type are never observed (Fig. 31). One population comprises CCVs associated with the apical PM whereas the second population was found in the region of the ER aggregate in the center of the Spitzenkoerper. An accumulation of CCVs in the apical cell region has also been reported from other tip-growing cells, e.g. pollen tubes (Robertson and Lyttleton 1982; Derksen et al. 1995; Blackbourn and Jackson 1996; Malhó et al. 2005) and root hairs (Bonnett and Newcomb 1966; Emons and Traas 1986), pointing to a common function of these vesicles for tip growth mechanisms in rapidly expanding polarized cells.

CCVs at the apical PM of rhizoids were observed to be closely associated with the membrane and were not detected at distances larger than 500 nm. Vesicle density was highest at the outermost tip and decreased towards the lateral flanks of the tube-like cells, which coincides with the distribution pattern of SVs. Several clathrin-coated buds were identified at the apical PM representing stages of CCV formation. The distribution of CCVs at the apical PM of tip-growing rhizoids is very well in accordance with the generally accepted role of these vesicles in endocytotic processes (Robinson 1996; Robinson et al. 1998a; Holstein 2002; Šamaj et al. 2005). In higher plants, CCV-mediated endocytosis is assumed to be responsible for the removal of excess membrane material that is delivered to the cell surface by SVs during tip growth (Derksen et al. 1995; Blackbourn and Jackson 1996; Emons and Traas 1986; Malhó et al. 2005), cell plate formation (Samuels et al. 1995; Otegui and Staehelin 2000; Seguí-Simarro and Staehelin 2005), and in the secretory pathway (Steer 1988). However, a detailed structural and functional description of endocytotic processes in plants is still lacking. Modeling of CCVs in electron tomograms of characean rhizoids and 3D-analysis of their distribution at the apical PM provides completely new insights into the endocytotic pathway of tip-growing cell types. The clustered distribution of CCVs strongly suggests that endocytotic membrane recycling is confined to specialized domains of the PM instead of occuring over the entire membrane area. Thereby, interference between the reversely oriented vesicle trafficking processes of exo- and endocytosis could be avoided by the local restriction of membrane internalization. In pollen tubes, the highest density of CCVs was found in a region 6 – 15 µm behind the tip, which implicates that the membrane domains of exocytosis (at the outermost cell tip) and endocytosis (in the CCV-rich region) are more clearly separated in this cell type as compared to rhizoids (Derksen et al. 1995). However, all studies reporting

an accumulation of CCVs in the apex of tip-growing cell types (Bonnett and Newcomb 1966; Robertson and Lyttleton 1982; Emons and Traas 1986; Derksen et al. 1995; Blackbourn and Jackson 1996) used conventional electron microscopy. A re-evaluation of CCV distribution by high-resolution electron microscopy in these cells could complement the new insights of the present study and help to characterize the organization and regulation of endocytosis in plant tip growth.

In-vivo staining of rhizoids with FM dyes that are widely used to visualize endocytotic events did not confirm the existence of confined endocytosis sites but instead produced homogeneous fluorescence of the apical cytoplasm. However, the putative 'hot spots' of endocytosis may be undetectable at the resolution level of fluorescence microscopy due to the small size of the CCVs and the strong background fluorescence of the cytoplasm. In addition, the suitability of FM dyes for specifically visualizing endocytotic events in plant cells is questionable (Malhó et al. 2005). FM labeling in pollen tubes did not reveal the distribution pattern of CCVs that was detected by electron microscopy (Derksen et al. 1995) but rather reflected the cone-shaped accumulation of the entirety of vesicles in the cytoplasm (Parton et al. 2001, 2003; Camacho and Malhó 2003). Similarly, the brightly fluorescing ring that was occasionally observed after FM staining of rhizoids indicates that the dyes labeled all types of vesicles and are therefore not suited for specifically visualizing endocytosis.

In high-pressure frozen samples of characean rhizoids, clusters of CCVs were sometimes associated with tubular invaginations of the apical PM and single CCVs were found to be formed at the ends of these invaginations. The diameter of the invaginations was in the same range as the diameter of the CCVs and a protein coat was occasionally detectable at the cytoplasmic surface. These observations give rise to the interpretation that sequential pinching off of CCVs from the ends of the invaginations may represent an efficient process for the retrieval of membrane material at the endocytosis sites.

Since CCVs lose their characteristic protein coat after vesicle formation, it is impossible to identify succeeding vesicle stages and to determine the total number of endocytotic vesicles by electron microscopy. Calculating the density of CCVs in electron tomograms of high-pressure frozen rhizoids relative to the total area of cytoplasm covered by the tomograms inevitably underestimates the total number of vesicles being involved in endocytosis. The density of endocytotic vesicles is more accurately estimated when the number of CCVs observed in the tomograms is referred to the volume of the 500 nm-broad cytoplasmic region where they were exclusively observed. Although the analysis of vesicle distribution in

electron tomograms provides very precise values of vesicle densities (see Table V) a calculation of growth parameters in the Chara rhizoid is omitted in this study because too many factors of the complex vesicle trafficking machinery are unknown, e.g. the time courses of vesicle formation, vesicle maturation, coat disassembly, and of exocytotic events as well as vesicle functions and intracellular targets of CCVs. Computations of endocytosis rates in tip-growing cell types based upon values of vesicle densities that were determined in elelctron microscopic samples (Emons and Traas 1986; Steer 1988; Derksen et al. 1995) are therefore always inaccurate.

In order to determine later stages and intracellular targets of CCV-mediated endocytosis in rhizoids it would be helpful to identify the contents of CCVs and to analyze, subsequently, the subcellular localization of these contents by immuolabeling experiments. However, the cargo material of CCVs in plant cells is still a matter of speculation (Holstein 2002). In protoplasts and suspension cultures of plant cells, electron-dense markers were used to track endocytotic pathways in electron microscopic studies (Tanchak 1984; Hillmer et al. 1986; Galway et al. 1993). Although it is unclear if the markers can be internalized by cells that are surrounded by a CW it may be worthwile to perform similar experiments with characean rhizoids in order to identify cellular compartments being involved in endocytosis.

It is a striking observation of the present study that a second population of CCVs localized to the region of the ER aggregate in the center of the growth-organizing Spitzenkoerper complex of rhizoids (Fig. 31). These vesicles were identified in high-pressure frozen and freeze-substituted samples by electron tomography and by immunolabeling with a clathrin-antibody. They were significantly larger than the CCVs at the apical PM but no differences were observed regarding the thickness and the structure of the clathrin coat. It is therefore unclear whether the vesicle population in the cytoplasm of the ER aggregate represents a different class of CCVs or whether the differences in vesicle size between the CCV populations are only related to different cargo and transport mechanisms.

In plant cells, CCVs have generally been implicated in either endocytotic pathways or in transport processes from Golgi stacks to vacuoles and prevacuolar compartments (Robinson 1996; Robinson et al. 2000; Holstein 2002). It is unlikely that the CCVs in the Spitzenkoerper cytoplasm represent an accumulation of endocytotic vesicles deriving from the PM since no CCVs were observed in a broad cytoplasmic region surrounding the ER aggregate. In addition, a role of this vesicle population for transport processes starting at Golgi stacks can

be ruled out because Golgi stacks are excluded from the interior of the ER aggregate and rarely observed in the apical cytoplasm (this study; Sievers et al. 1965, 1967a, 1967b; Bartnik 1984; Kiss and Staehelin 1993). Instead, the vesicle accumulation within the ER aggregate indicates that the CCVs are involved in transport processes that are closely linked to the ER cisternae. CCVs may, for instance, be responsible for inter-cisternal transport mechanisms and thereby contribute to the maintenance of specific domains within the large complex of ER cisternae. Since vesicles quickly lose their protein coat, the progression of the clathrin-dependent transport pathway could unfortunately not be identified. However, it cannot be ruled out that CCVs in the cytoplasm of the Spitzenkoerper center represent initial stages of transport processes occurring over longer distances from the ER aggregate to other cellular compartments in the rhizoid. Alternatively, the CCVs could be responsible for the sequestration of contents deriving from the ER cisternae that are released upon specific cellular signals – similar to transmitter-containing vesicles at the synapses of neurons. However, until today CCVs have never been observed to be involved in secretory processes but implicated in the reversly oriented mechanisms of membrane recycling instead (Royle and Lagnado 2003). It will be interesting to further investigate the function of CCVs in the Spitzenkoerper and to unravel their role for tip growth of characean rhizoids. Anyway, the identification of CCVs accumulating within the ER aggregate represents a turning point in the understanding of the function of CCVs in plant cells which have so far not been implicated in ER-related transport processes (Robinson 1996; Robinson et al. 2000; Holstein 2002).

When high-pressure frozen rhizoids were immunolabeled with a clathrin-specific antibody, specific vesicle-like labeling was concentrated in the vicinity of MTs giving rise to the conclusion that CCVs are present in this cell region which are transported in a MT-dependent manner. The fact that no subapical clathrin vesicles were observed in samples prepared for ultrastructural studies is attributed to the limited resolution of conventional electron microscopy that was used for analyses of the subapical region. Investigation of the apical cytoplasm of rhizoids has demonstrated that high-resolution electron tomography is required for unambiguously identifying CCVs. Alternatively, the vesicles in the subapical cytoplasm which were labeled with the clathrin antibody may represent successive stages of CCVs, and the loss of the protein coat could explain the failure in ultrastructural detection. In this case, the antibody may bind to residual clathrin being present at the surface of the vesicles. This consideration would be in accordance with the generally accepted idea that the protein coat of CCVs is rapidly disassembled upon vesicle formation and prior to the transport to their target

compartments (Ungewickell et al. 1995; Holstein et al. 1996; Robinson 1996). However, when high-pressure frozen Arabidopsis roots were imunolabeled with the clathrin antibody, the prominent structure of the clathrin scaffolds was observed to underlie vesicle-specific labeling in cells of the elongation zone (B.-H. Kang, University of Colorado, Boulder, USA, personal communication). Similarly to rhizoids, the labeled vesicles were aligned at MTs. Therefore, the observations from ultrastructural studies in characean rhizoids and Arabidopsis roots question the present idea of CCV-transport but may indicate instead that CCVs travel along MTs with fully assembled clathrin coats, and vesicle uncoating may occur shortly before fusion with the target membrane.

#### 4.3.2.4 Coated vesicles

In addition to CCVs, a second type of vesicles bearing a protein coat was identified in the apical cytoplasm of characean rhizoids by electron tomography. The coated vesicles (CVs) are characterized by an unstructured and homogeneously stained protein coat that is totally different from the clathrin scaffold of CCVs. CVs have not been detected in any of the previous studies investigating the ultrastructure of characean rhizoids or other tip-growing cell types and cannot clearly be assigned to any of the common vesicles types found in plant cells (Robinson et al. 1998a, Ritzenthaler et al. 2002). Thus, it can only be speculated about the nature of the coat-forming proteins and on the cellular functions of CVs.

Although the differences in size are not big, CVs are significantly larger than MVs and smaller than CCVs. The high electron density of the vesicle contents contrasts with the poor staining of material inside MVs but similar to the electron density of the CCV contents. A structural or functional connection of CVs and MVs is therefore unlikely. But still, it cannot be ruled out that CVs may be related to the transport processes mediated by CCVs, e.g. by representing successive vesicle stages which are characterized by an increased level of condensation of the vesicle contents. CVs share some similarities with COP-coated vesicles but cannot definitely be assigned to one of these classes of coated vesicles. CVs that were observed in rhizoids are smaller than COP II vesicles of higher plants and possess a thicker protein coat, whereas COP I vesicles would be expected to contain material with higher electron density as was found inside the CVs (B.-H. Kang, University of Colorado, Boulder, USA, personal communication).

Since the nature of CVs in the Chara rhizoid remains unclear, it is reasonable to regard the CVs as a distinct class of vesicles with specific functions. The accumulation of CVs at the periphery of the apical ER aggregate corresponds to the distribution pattern of SVs and MVs and underlines the important role of the ER complex for vesicle trafficking. The observation that CVs were the only vesicles apart from CCVs that were abundant in central regions of the ER aggregate indicates that CVs may be involved in transport processes which are closely linked to the ER, e.g. intercisternal transport.

### 4.3.3 Vacuolar reticulum

When analyzing the ultrastructure of high-pressure frozen characean rhizoids, a prominent membrane-encircled compartment that has not been described in any of the previous electron microscopic studies of chemically fixed or cryofixed samples was discovered (Sievers 1965; 1967a, 1967b; Bartnik 1984; Kiss und Staehelin 1993; Noecker 2000). The failure in detection after chemical fixation was most likely caused by artifactual vesiculation of the compartment giving rise to the misinterpretation of the vesiculated segments as large vesicles. A similar effect was observed in chemically fixed fungal hyphae (Orlovich and Ashford 1993; Ashford 1998).

The polymorphic membrane system identified in cryofixed rhizoids consists of numerous spherical, vesicle-like segments that are interconnected and form an extensive network with considerable dimensions extending throughout the entire subapical cell region. The compartment exhibits striking similarities to the vacuolar reticulum of fungal hyphae (Shepherd et al. 1993; Allaway et al. 1997; Ashford 1998; Cole et al. 1998) which are, just like characean rhizoids, polarized and tip-growing cells. The ultrastructural characteristics of the reticulate network, i.e. cellular arrangement, membrane structure, and electron density of the lumen are consistent in both cell types. In rhizoids, however, the segments are more uniform in diameter and more often aligned in straight rows.

An important argument for defining the membrane compartment in fungal hyphae as a vacuolar reticulum was the specific labeling with fluorescence dyes that are reported to accumulate in vacuoles (Shepherd et al. 1993; Allaway et al. 1997; Cole et al. 1998). In-vivo fluorescence staining demonstrated highly dynamic remodeling and peristaltic movement of the vacuolar reticulum in this cell type (Shepherd et al. 1993; Cole et al. 1998; Hyde et al. 1999). When living rhizoids were labeled with the vacuole dye DFFDA, a fine, dynamic

network was identified that extended throughout the entire subapical region and, thereby, was in accordance with the intracellular distribution of the vacuolar reticulum that was observed by electron microscopy. However, the fluorescent network exhibited no spherical segments, which does not reflect the structural arrangement in the electron microscopic samples and differs from the fluorescence pattern of DFFDA-staining in fungal hyphae (Shepherd et al. 1993; Cole et al. 1998; Hyde et al. 1999). The pattern of fluorescence in rhizoids resembled more the reticulate arrangement of the ER as is observed in a variety of plant cell types (Staehelin 1997; Satiat-Jeunemaitre et al. 1999). It has, however, clearly been demonstrated by electron microscopy that the ER in the subapical zone of characean rhizoids forms longitudinally oriented stacks of cisternae rather than a network arrangement (Fig. 19, 20; Bartnik 1984; Noecker 2000). In addition, DFFDA is unlikely to label cisternae of the ER because the dye has been reported to accumulate selectively in vacuoles (Cole et al. 1998; Wilson et al. 1998), and no colocalization of fluorescence was found when fungal hyphae were stained with DFFDA and ER-tracker (Cole et al. 2000). If DFFDA labeled the ER in rhizoids, one would expect bright fluorescence of the densely packed cisternae of the ER aggregate in the apical region, which was, however, not observed. Instead, the dye accumulated subsequently in the basal vacuole. These observations provide strong evidence that DFFDA labeled indeed the vacuolar reticulum that was identified in electron microscopic samples of rhizoids. The differences in the shape of the vacuolar reticulum between electron microscopy and fluorescence staining may be attributed to the fact that electron micrographs represent static snapshots of a highly dynamic compartment. The spherical segments may be undetectable by fluorescence microscopy in rhizoids due to the limited spatiotemporal resolution whereas the larger segments of the vacuolar reticulum in fungal hyphae (Shepherd et al. 1993) may be discovered more easily.

In-vivo staining with BCECF, a fluorescence dye that is used as indicator for intracellular pH and was shown to accumulate in vacuoles of root hairs producing DFFDA-like staining pattern (Brauer et al. 1995), proved not to be suited for labeling of the vacuolar reticulum in rhizoids. The dye did not accumulate in any compartment but instead produced homogeneous fluorescence of the entire cytoplasm.

It is a striking observation of the electron microscopic studies of high-pressure frozen rhizoids that the vacuolar reticulum was found to be closely associated with MTs. The distance between the membranes of the segments and MTs was in the range of 10 nm and even less, which would be sufficient for molecular interaction to occur. Similarly, the segments of the

reticulum were always accompanied by MTs in electron microscopic samples of fungal hyphae, and MT-disrupting drugs, e.g. oryzalin, were shown to strongly affect the structural and dynamic properties of the reticulum in living samples whereas actin-disrupting drugs had no effect (Hyde et al. 1999). These observations support the idea that the morphology and the motility of the vacuolar reticulum depend on MTs. Since actin filaments were not detectable in the subapical regions of rhizoids (this study) and hyphae (Hyde et al. 1999), however, it cannot be ruled out that actin microfilaments may also be associated with segments of the vacuolar reticulum and contribute to the regulation of morphological and dynamic properties. Fine, ring-like structures which were occasionally observed to encircle tubular connections of the vacuolar reticulum in rhizoids may represent aggregates of dynamin molecules that could be responsible for mediating peristaltic motility of the compartment that is reported from fungal hyphae (Shepherd et al. 1993). However, additional work including fluorescence microscopy and electron microscopic ultrastructural analyses of inhibitor-treated cells is required to unravel the dynamic properties of the vacuolar reticulum in characean rhizoids.

Although the membrane network of interconnected spherical segments in the Chara rhizoid has been clearly identified as a vacuolar reticulum based upon the striking similarities with the corresponding compartment in fungal hyphae, the cellular functions remain unclear. In hyphae, several roles of the vacuolar reticulum are discussed including material transport and endosomal function (Shepherd et al. 1993; Allaway et al. 1997; Ashford 1998; Cole et al. 1998).

First of all, the specialized vacuolar network was suggested to constitute a transport pathway for intracellular bulk flow of material (Shepherd et al. 1993; Ashford 1998; Cole et al. 1998). According to this theory, cargo that was delivered to the vacuolar reticulum would be transported in the lumen of the compartment by peristaltic movement of the surrounding membrane. Thereby, intracellular transport would be significantly accelerated compared to diffusion without requiring translocation of membrane material or membrane recycling. This transport pathway would of course be less specific than vesicular transport since all contents would be transported in the same direction. Nonetheless, delivery of the cargo to specific target domains of the reticulum could be accomplished by receptor-mediated sorting processes that are similar to those directing molecules into vesicles. In characean rhizoids, bulk flow of material in the lumen of the vacuolar reticulum may represent a simple but efficient pathway for long-distance transport in the subapical region. By providing an

alternative to vesicle transport, the vacuolar reticulum may contribute to the variability of individually regulated intracellular transport processes. Extended tubular vacuoles that share some structural and functional similarities with the vacuolar reticulum have also been identified in tip-growing pollen tubes and were disussed to be involved in transport mechanisms (Derksen et al. 2002; Hicks et al. 2004).

The role of the vacuolar reticulum as an endosomal compartment has been discussed in great detail for fungal hyphae (Ashford 1998). Accordingly, the vacuolar membrane system was regarded as the equivalent to endosomal-lysosomal networks described in animal cells based upon similarities in structure and motility. In the present study, striking consistencies were observed in the ultrastructure of the vacuolar reticulum and of MVBs regarding the appearance of the membranes, the electron density of the lumen and the existence of internal, vesicle-like particles. MVBs that are labeled by endocytotic (Hillmer et al. 1986, Galway et al. 1993) and vacuolar markers (Record and Griffing 1988; Tse et al. 2004) are generally considered to represent a prevacuolar compartment that is involved in the endocytotic pathway of plant cells (Ashford 1998; Robinson et al. 1998b; Robinson et al. 2000; Seguí-Simarro and Staehelin 2005). Based upon the ultrastructural similarities with MVBs, the present study supports an endosomal function of the vacuolar reticulum although in-vivo staining with FM dyes which are widely used to study endocytosis did not label the vacuolar reticulum in rhizoids (this study) and fungal hyphae (Cole et al. 1998). However, as discussed above, the specificity of FM dyes for labeling of endocytotic compartments is questionable and results of FM staining should therefore be regarded with caution in rhizoids.

Interestingly, Noecker (2000) identified epitopes of arabinogalactan-proteoglycans (AGPs) in the lumen of large, vesicle-like structures in the subapical cytoplasm of rhizoids. Based upon the electron microscopic observations from the present study it becomes clear that these structures that were misinterpreted by Noecker as MVBs, represent segments of the vacuolar reticulum which was vesiculated during preparation. Since AGPs are CW components that underlie a high turn-over rate and are internalized by endocytosis, their presence in the lumen of the vacuolar reticulum supports the idea that this compartment is involved in endocytosis. It will be interesting to see if additional contents of endocytotic compartments can be identified in the reticulate membrane compartment. Comprehensive immunolabeling experiments with various antibodies raised against a wide range of proteins are required for clarifying whether the vacuolar reticulum in characean rhizoids is an endosomal or an intracellular transport compartment or a combination of both.

## 4.4 High-pressure freeze fixation and freeze substitution for immuno-electron microscopy

Immuno-electron microscopy offers the opportunity to analyze the subcellular localization of proteins as well as the structural and functional interrelation of cellular compartments at a high level of resolution. It is, therefore, excellently suited for characterizing in great detail the molecular and structural features of characean rhizoids and protonemata which are related to gravity sensing and gravity-oriented tip growth. In the past, the application of immuno-electron microscopy proved challenging due to the difficulties in preparing decent electron microscopic samples. When chemical fixation was used, artefactual alteration of the protein conformation often interfered with the specific binding of antibodies to the corresponding protein epitopes. The development of cryofixation techniques has greatly improved the quality of samples for immuno-electron microscopy. Since all cell components are immobilized fast and simultaneously during cryofixation and epitopes are not affected during freeze substitution with low amounts of chemical reagents, the samples exhibit excellent preservation of both, ultrastructure and protein conformation (Ichikawa et al. 1989; Monaghan et al. 1998; Giddings 2003). Recent immunolabeling experiments using cryofixed samples have enhanced the knowledge about cellular processes in various cell types (e.g. Otegui and Staehelin 2000, 2004; Otegui et al. 2001, 2002). Until today, however, little is known about the subcellular distribution and structural arrangement of proteins that regulate the mechanisms of tip growth in polarized cells (Geitmann and Emons 2000; Hepler et al. 2001; Braun and Limbach 2005a). Studies using immunogold labeling in chemically fixed (Noecker 2000) and cryofixed samples (Kiss and Staehlin 1993) of characean rhizoids are rare and predominantly focused on the distribution of CW components but did not provide information about the localization of cytoplasmic proteins.

In the present study, a protocol was developed for the preparation of rhizoid samples for immuno-electron microscopy that is based upon high-pressure freeze fixation and freeze substitution. This technique significantly improved the ultrastructural preservation and the conservation of protein conformation as evidenced by the specific immunogold localization of actin microfilament bundles and CCVs (see 4.3.1.3 and 4.3.2.3). Since immunolabeling of actin microfilaments proved difficult in various cell types due to the sensitivity of actin epitopes towards chemical fixation and cryofixation (Schopfer and Hepler 1991; Ding et al. 1992; Geitmann and Emons 2000), information about the subcellular actin arrangement which

is crucial for the regulation of tip growth mechanisms is still scarce (Hepler et al. 2001). The successful labeling of actin microfilaments in the characean rhizoid underlines the high quality of the samples and promises a detailed description of the actin architecture in a tip-growing cell in the near future.

For freeze substitution of high-pressure frozen rhizoids marginal amounts of glutaraldehyde and uranyl acetate were used and osmium tetroxide and tannic acid were completely omitted causing low overall contrast of the samples. The poor staining hampered handling of the samples during freeze substitution and sectioning and made the identification of cellular compartments difficult. Enhanced contrast of the samples would help to avoid mechanical damage of the rhizoids at the outermost tip and would facilitate the interpretation of labeling patterns that could be assigned more clearly to cellular structures and compartments. It should therefore be tested if low concentrations of osmium tetroxide can be added to the substitution medium without affecting the specific binding of antibodies to the protein epitopes. In this study, Lowicryl HM20 was used as embedding resin which has been reported in several studies to exhibit the best properties for immuno-electron microscopy and concomitant ultrastructural studies of all resins tested (Ichikawa et al. 1989; Monaghan et al. 1997; Giddings 2003). However, due to health risks when working with the highly toxic Lowicryl it is recommended to test alternative resins for their applicability to immunogold labeling experiments.

The newly developed protocol for the preparation of rhizoid samples for immuno-electron microscopy not only provides interesting results regarding the actin arrangement and the mechanisms of CCV transport but also establishes a basis for further studies aiming at the functional characterization of cellular proteins and compartments. It will be helpful for elucidating the role of actin, actin-binding proteins and calcium channels in the tip growth machinery and for determining the cellular functions of the different vesicle types and of the vacuolar reticulum in characean rhizoids. In addition, this technique has the potential to upgrade the understanding of the mechanisms of gravity sensing and gravity-oriented growth significantly by providing the precise subcellular localization of gravireceptor molecules and of additional components of the gravitropic signaling pathway, e.g. the glucosyltransferase which was found to be differentially expressed in rhizoids upon gravistimulation.

# 5 SUMMARY

In the present study, molecular, cellular, and functional aspects of gravity sensing and gravity-oriented tip growth were studied in characean rhizoids and protonemata using innovative experimental tools, e.g. gene expression analysis and high-resolution electron microscopy. The results provide new insights into ultrastructural characteristics of polarized plant cells and into mechanisms of gene regulation and receptor activation in gravity sensing.

The optimization of protocols for the isolation of mRNA from rhizoids and protonemata lead to the discovery and characterization of several gene products. Two characean genes were sequenced at full length and identified as 60S ribosomal proteins of the L14 and L27 family, repectively. The proteins encoded by these housekeeping genes are crucial components of the protein synthesis machinery of ribosomes. The partial sequencing of a myosin from characean rhizoids represents the initial step of a molecular analysis of the various protein isoforms and their manifold cellular functions in tip-growing plant cell types. Differential display analysis of gene expression in gravistimulated and in unstimulated rhizoids provided several partial sequences of genes the expression levels of which were significantly altered upon gravistimulation. These genes are implicated in the gravitropic signaling pathway. One of the genes that was up-regulated in gravistimulated cells was characterized at full length and identified to encode a glucosyltransferase. This enzyme, which is involved in the synthesis of cell wall components, is likely to represent a target of gravitropic signaling in characean rhizoids, and regulation of gene expression may cause changes in CW properties during the gravitropic curvature response.

Experiments under microgravity conditions provided by parabolic flights of the A300 Zero-G aircraft and of sounding rockets were performed to investigate specific aspects of the early processes of gravity sensing. For the first time in a gravity-sensing plant cell type the molecular forces restricting statolith sedimentation and the functional mechanism of gravireceptor activation were determined in rhizoids and protonemata. Centrifugal forces were applied to vertically growing rhizoids and protonemata during the microgravity phase of the MAXUS-5 sounding rocket flight. Lateral acceleration levels of 0.14*g*, but not 0.05*g,* resulted in a displacement of statoliths and forced individual statoliths to settle onto the subapical PM where they initiated the gravitropic response. Since actin controls the positioning of statoliths and restricts statolith sedimentation in these cells, it can be calculated that lateral actomyosin forces in a range of $2 \times 10^{-14}$ N act on statoliths to keep them in place.

These forces represent the threshold value that has to be exceeded by any lateral acceleration stimulus for statolith sedimentation and gravisensing to occur. When rhizoids were gravistimulated during parabolic plane flights, the curvature angles of the flight samples, whose sedimented statoliths became weightless for 22 s during the 31 microgravity phases, were not different from those of in-flight controls. However, in ground control experiments, curvature responses were drastically reduced when the contact of statoliths with the plasma membrane was intermittently interrupted by inverting gravistimulated cells for less than 10 s. It can be concluded that graviperception in characean rhizoids requires contact of statoliths with membrane-bound receptor molecules rather than pressure or tension exerted by the weight of statoliths.

After the functional mechanism of gravirecptor activation has been clarified, the protocols for high-pressure freeze fixation and 3D dual-axis electron tomography of characean rhizoids that were established in this study provide powerful experimental applications to analyze the structural principles underlying gravity sensing and tip growth. The clustered distribution of clathrin-coated vesicles (CCVs) at the apical plasma membrane strongly implicates that endocytotic processes mediating the retrieval of excess membrane material are not accomplished over the entire membrane area but are confined to distinct ‘endocytosis sites’. The function of a second population of CCVs whose distribution was restricted to the cytoplasm within the central region of the Spitzenkoerper is less clear. However, since vesicles are closely associated with the apical endoplasmic reticulum (ER) aggregate, it is assumed that CCVs mediate transport processes proceeding from the ER – a function that has not been assigned to CCVs in plant cells so far. In the subapical region of rhizoids a prominent compartment was identified by fluorescence labeling and electron microscopy consisting of spherical segments that are interconnected and form an extensive network. The vacuolar reticulum may either mediate long-distance transport of material in the lumen of the compartment or represent an endosomal compartment that could be a target of endocytotic CCVs.

The results presented in this study substantially contribute to the understanding of the mechanisms of endocytosis and intracellular transport in polarized plant cells. The progress that has been made in unraveling early processes of gravity sensing in characean rhizoids and protonemata underlines the significance of single-celled model systems for investigating how plants use gravity as a guide for orientation.

# 6 REFERENCES

## 6.1 Literature


**Alberts B, Bray D, Lewis J, Raff M, Roberts K, Watson JD** (1995) Molekularbiologie der Zelle, Ed 3. VCH, Weinheim

**Allaway WG, Ashford AE, Heath IB, Hardham AR** (1997) Vacuolar reticulum in oomycete hyphal tips: an additional component of the $Ca^{2+}$ regulatory system? Fung Genet Biol 22: 209 – 220

**Aloni R, Langhans M, Aloni E, Ullrich CI** (2004) Role of cytokinin in the regulation of root gravitropism. Planta 220: 177 – 182

**Ashford AE** (1998) Dynamic pleiomorphic vacuole systems: are they endosomes and transport compartments in fungal hyphae? Adv Bot Res 28: 119 – 159

**Austin JR, Seguí-Simarro JM, Staehelin LA** (2005) Quantitative analysis of changes in spatial distribution and plus-end geometry of microtubules involved in plant-cell cytokinesis. J Cell Sci 118: 3895 – 3903

**Bartnik E** (1984) Die Rolle des endoplasmatischen Retikulums beim Spitzenwachstum von Chara-Rhizoiden. Diploma thesis, Botanical Institute, University of Bonn, Germany

**Bartnik E, Sievers A** (1988) In vivo observations of a spherical aggregate of endoplasmic reticulum and of Golgi vesicles in the tip of fast-growing Chara rhizoids. Planta 176: 1 – 9

**Bartnik E, Hejnowicz Z, Sievers A** (1990) Shuttle-like movements of Golgi vesicles in the tip of growing Chara rhizoids. Protoplasma 159: 1 – 8

**Björkman T** (1988) Perception of gravity by plants. Adv Bot Res 15: 1 – 41

**Blackbourn HD, Jackson AP** (1996) Plant clathrin heavy chain: sequence analysis and restricted localisation in growing pollen tubes. J Cell Sci 109: 777 – 787

**Blancaflor EB** (2002) The cytoskeleton and gravitropism in higher plants. J Plant Growth Regul 21: 120 – 136

**Blancaflor EB, Hasenstein KH** (1997) The organization of the actin cytoskeleton in vertical and graviresponding primary roots of maize. Plant Physiol 113: 1447 – 1455

**Blancaflor EB, Masson PH** (2003) Plant gravitropism. Unraveling the ups and downs of a complex process. Plant Physiol 133: 1677 – 1690

**Blancaflor EB, Fasano JM, Gilroy S** (1998) Mapping the role of cap cells in root gravitropism. Plant Physiol 116: 213 – 222

**Blilou I, Xu J, Wildwater M, Willemsen V, Paponov I, Friml J, Heidstra R, Aida M, Palme K, Scheres B** (2005) The PIN auxin efflux facilitator network controls growth and patterning in Arabidopsis roots. Nature 433: 39 – 44

**Bonnett HT, Newcomb EH** (1966) Coated vesicles and other cytoplasmic components of growing root hairs of radish. Protoplasma 62: 59 – 75

**Boonsirichai K, Guan C, Chen, R, Masson PH** (2002) Root gravitropism: an experimental tool to investigate basic cellular and molecular processes underlying mechanosensing and signal transmission in plants. Annu Rev Plant Physiol Plant Mol Biol 53: 421 – 447

**Bouton S, Leboeuf E, Mouille G, Leydecker MT, Talbotec J, Granier F, Lahaye M, Höfte H, Truong HN** (2002) QUASIMODO1 encodes a putative membrane-bound glycosyltransferase required for normal pectin synthesis and cell adhesion in Arabidopsis. Plant Cell 14: 2577 – 2590

**Brandt S, Kehr J, Walz C, Imlau A, Willmitzer L, Fisahn J** (1999) A rapid method for detection of plant gene transcripts from single epidermal, mesophyll and companion cells of intact leaves. Plant J 20: 245 – 250

**Brandt S, Kloska S, Altmann T, Kehr J** (2002) Using array hybridization to monitor gene expression at the single cell level. J Exp Bot 53: 2315 – 2323

**Brauer D, Otto J, Tu S-I** (1995) Selective accumulation of the fluorescent pH indicator, BCECF, in vacuoles of maize root-hair cells. J Plant Physiol 145: 57 – 61

**Braun M** (1994) Cytoskelett und Gravitropismus des Chara-Rhizoids. PhD thesis, Botanical Institute, University of Bonn

**Braun M** (1996a) Anomalous gravitropic response of Chara rhizoids during enhanced accelerations. Planta 199: 443 – 450

**Braun M** (1996b) Immunolocalization of myosin in rhizoids of *Chara globularis* Thuill. Protoplasma 191: 1 – 8

**Braun M** (1997) Gravitropism in tip-growing cells. Planta 203: S11 – S19

**Braun M** (2001) Association of spectrin-like proteins with the actin-organized aggregate of endoplasmic reticulum in the Spitzenkörper of gravitropically tip-growing plant cells. Plant Physiol 125: 1611 – 1620

**Braun M** (2002) Gravity perception requires statoliths settled on specific plasma-membrane areas in characean rhizoids and protonemata. Protoplasma 219: 150 – 159

**Braun M, Limbach C** (2005a) Rhizoids and protonemata of characean algae – unicellular model systems for research on polarized growth and plant gravity sensing. Protoplasma (in press)

**Braun M, Limbach C** (2005b) Actin-based gravity-sensing mechanisms in unicellular plant model systems. Proceedings of the 17th ESA Symposium on European Rocket and Balloon Programmes and Related Research, Sandefjord, Norway, ESA SP-590: 41 – 45

**Braun M, Limbach C** (2005c) Gravisensing in single-celled systems – update on characean rhizoids and protonemata. Advances in Space Research 36: 1156 – 1161

**Braun M, Richter P** (1999) Relocalization of the calcium gradient and a dihydropyridine receptor is involved in upward bending by bulging of Chara protonemata, but not in downward bending by bowing of Chara rhizoids. Planta 209: 414 – 423

**Braun M, Sievers A** (1993) Centrifugation causes adaptation of microfilaments: studies on the transport of statoliths in gravity sensing Chara rhizoids. Protoplasma 174: 50 – 61

**Braun M, Sievers A** (1994) Role of the microtubule cytoskeleton in gravisensing Chara rhizoids. Eur J Cell Biol 63: 289 – 298

**Braun M, Wasteneys GO** (1998a) Reorganization of the actin and microtubule cytoskeleton throughout blue-light-induced differentiation of characean protonemata into multicellular thalli. Protoplasma 202: 38 – 53

**Braun M, Wasteneys GO** (1998b) Distribution and dynamics of the cytoskeleton in graviresponding protonemata and rhizoids of characean algae: exclusion of microtubules and a convergence of actin filaments in the apex suggest an actin-mediated gravitropism. Planta 205: 39 – 50

**Braun M, Buchen B, Sievers A** (2002) Actomyosin-mediated statolith positioning in gravisensing plant cells studied in microgravity. J Plant Growth Regul 21: 137 – 145

**Braun M, Hauslage J, Czogalla A, Limbach C** (2004) Tip-localized actin polymerization and remodeling, reflected by the localization of ADF, profilin and villin, are fundamental for gravitropic tip growth in characean rhizoids. Planta 219: 379 – 388

**Brown AH, Chapman DK, Johnsson A, Heathcote D** (1995) Gravitropic responses of the Avena coleoptile in space and on clinostats. I. Gravitropic response thresholds. Physiol Plant 95: 27 – 33

**Buchen B, Braun M, Hejnowicz Z, Sievers A** (1993) Statoliths pull on microfilaments. Experiments under microgravity. Protoplasma 172: 38 – 42

**Cai W, Braun M, Sievers A** (1997) Displacement of statoliths in Chara rhizoids during horizontal rotation on clinostats. Acta Biol Exp Sinica 30: 147 – 155

**Camacho L, Malho R** (2003) Endo-exocytosis in the pollen tube apex is differentially regulated by $Ca^{2+}$ and GTPases. J Exp Bot 54: 83 – 92

**Charbit E, Legavre T, Lardet L, Bourgeois E, Ferrière N, Carron MP** (2004) Identification of differentially expressed cDNA sequences and histological characteristics of *Hevea brasiliensis* calli in relation to their embryogenic and regenerative capacities. Plant Cell Rep 22: 539 – 548

**Chen JCF, Tsai CCY, Tzen JTC** (1999) Cloning and secondary structure analysis of caleosin, a unique calcium-binding protein in oil bodies of plant seeds. Plant Cell Physiol 40: 1079 – 1086

**Cole L, Davies D, Hyde GJ, Ashford AE** (2000) ER-tracker dye and BODIPY-brefeldin A differentiate the endoplasmic reticulum and Golgi bodies from the tubular-vacuole system in living hyphae of *Pisolithus tinctorius*. J Microsc 197: 239 – 248

**Cole L, Orlovich DA, Ashford AE** (1998) Structure, function, and motility of vacuoles in filamentous fungi. Fung Genet Biol 24: 86 – 100

**Dahl R, Staehelin LA** (1989) High-pressure freezing for the preservation of biological structure: theory and practice. J Electron Microsc Tech 13: 165 – 174

**Derksen J, Knuiman B, Hoedemaekers K, Guyon A, Bonhomme S, Pierson ES** (2002) Growth and cellular organization of Arabidopsis pollen tubes in vitro. Sex Plant Reprod 15: 133 – 139

**Derksen J, Rutten T, Lichtscheidl IK, de Win AHN, Pierson ES, Rongen G** (1995) Quantitative analysis of the distribution of organelles in tobacco pollen tubes: implications for exocytosis and endocytosis. Protoplasma 188: 267 – 276

**Ding B, Turgeon R, Parthasarathy MV** (1992) Effect of high-pressure freezing on plant microfilament bundles. J Microsc 165: 367 – 376

**Driss-Ecole D, Jeune B, Prouteau M, Julianus P, Perbal G** (2000) Lentil root statoliths reach a stable state in microgravity. Planta 211: 396 – 405

**Egelund J, Skjøt M, Geshi N, Ulskov P, Petersen BL** (2004) A complementary bioinformatics approach to identify potential plant cell wall glycosyltransferase-encoding genes. Plant Physiol 136: 2609 – 2620

**Emons AMC, Traas JA** (1986) Coated pits and coated vesicles on the plasma membrane of plant cells. Eur J Cell Biol 41: 57 – 64

**Forsberg C** (1965) Nutritional studies of Chara in axenic cultures. Physiol Plant 18: 275 – 290

**Frandsen GI, Mundy J, Tzen JTC** (2001) Oil bodies and their associated proteins, oleosin and caleosin. Physiol Plant 112: 301 – 307

**Friedman H, Vos JW, Hepler PK, Meir S, Halevy AH, Philosoph-Hadas S** (2003) The role of actin filaments in the gravitropic response of snapdragon flowering shoots. Planta 216: 1034 – 1042

**Fujihira K, Kurata T, Watahiki MK, Karahara I, Yamamoto KT** (2000) An agravitropic mutant of Arabidopsis, endodermal-amyloplast less 1, that lacks amyloplasts in hypocotyl endodermal cell layer. Plant Cell Physiol 41:1193 – 1199

**Fukaki H, Fujisawa H, Tasaka M** (1996) SGR1, SGR2, and SGR3: Novel genetic loci involved in shoot gravitropism in Arabidopsis thaliana. Plant Physiol 110: 945 – 955

**Fukaki H, Wysocka-Diller J, Kato T, Fujisawa H, Benfey PN, Tasaka M** (1998) Genetic evidence that the endodermis is essential for shoot gravitropism in *Arabidopsis thaliana*. Plant J 14: 425 – 430

**Gallagher JA, Koroleva OA, Tomos DA, Farrar JF, Pollock CJ** (2001) Single cell analysis technique for comparison of specific mRNA abundance in plant cells. J Plant Physiol 158: 1089 – 1092

**Galway ME, Rennie PJ, Fowke LC** (1993) Ultrastructure of the endocytotic pathway in glutaraldehyde-fixed and high-pressure frozen/freeze-substituted protoplasts of white spruce (*Picea glauca*). J Cell Sci 106: 847 – 858

**Gasteiger E, Gattiker A, Hoogland C, Ivanyi I, Appel RD, Bairoch A** (2003) ExPASy: the proteomics server for in-depth protein knowledge and analysis. Nucleic Acids Res 31: 3784 – 3788

**Geitmann A, Emons AM** (2000) The cytoskeleton in plant and fungal cell tip growth. J Microsc 198: 218 – 245

**Giddings TH** (2003) Freeze-substitution protocols for improved visualization of membranes in high-pressure frozen samples. J Microsc 212: 53 – 61

**Gilbert PF** (1972) Reconstruction of a three-dimensional structure from projections and its application to electron-microscopy. II. Direct methods. Proc R Soc London B Biol Sci 182: 89 – 102

**Gilkey JC, Staehelin LA** (1986) Advances in ultrarapid freezing for the preservation of cellular structure. J Electron Microsc Tech 3: 177 – 210

**Haberlandt G** (1900) Über die Perzeption des geotropischen Reizes. Ber Dtsch Bot Ges 18: 261 – 272

**Häder D-P, Rosum A, Schäfer J, Hemmersbach R** (1995) Gravitaxis in the flagellate *Euglena gracilis* is controlled by an active gravireceptor. J Plant Physiol 146: 474 – 480

**Hauslage J** (2005) Funktionelle Charakterisierung der Gravirezeptoraktivierung in Chara-Rhizoiden. Diploma thesis, IMBIO, University of Bonn, Germany

**Hazen SP, Scott-Craig JS, Walton JD** (2002) Cellulose synthase-like genes of rice. Plant Physiol 128: 336 – 340

**Hejnowicz Z, Sievers A** (1981) Regulation of the position of statoliths in Chara rhizoids. Protoplasma 108: 117 – 137

**Hejnowicz Z, Heinemann B, Sievers A** (1977) Tip growth: patterns of growth rate and stress in the Chara rhizoid. Z Pflanzenphysiol 81: 409 – 424

**Hemmersbach R, Voormanns R, Briegleb W, Rieder N, Häder D-P** (1996) Influence of acceleration on the spatial orientation of Loxodes and Paramecium. J Biotechnol 47: 271 – 278

**Hepler PK, Vidali L, Cheung AY** (2001) Polarized cell growth in higher plants. Ann Rev Cell Dev Biol 17: 159 – 187

**Hess MW** (2003) Of plants and other pets: practical aspects of freeze-substitution and resin embedding. J Microsc 212: 44 – 52

**Hicks GR, Rojo E, Hong S, Carter DG, Raikhel NV** (2004) Germinating pollen has tubular vacuoles, displays highly dynamic vacuole biogenesis, and requires VACUOLESS1 for proper function. Plant Physiol 134: 1227 – 1239

**Hillmer S, Depta H, Robinson DG** (1986) Confirmation of endocytosis in higher plant protoplasts using lectin-gold conjugates. Eur J Cell Biol 41: 142 – 149

**Hodick D** (1993) The protonema of *Chara fragilis* Desv.: regenerative formation, photomorphogenesis, and gravitropism. Botanica Acta 106: 388 – 393

**Hodick D** (1994) Negative gravitropism in Chara protonemata: A model integrating the opposite gravitropic responses of protonemata and rhizoids. Planta 195: 43 – 49

**Hodick D, Sievers A** (1998) Hypergravity can reduce but not enhance the gravitropic response of *Chara globularis* protonemata. Protoplasma 204: 145 – 154

**Hodick D, Buchen B, Sievers A** (1998) Statolith positioning by microfilaments in Chara rhizoids and protonemata. Adv Space Res 21: 1183 – 1189

**Holstein SHE** (2002) Clathrin and plant endocytosis. Traffic 3: 614 – 620

**Holstein SHE** (2005) Molecular dissection of the clathrin-endocytosis machinery in plants. In: J Šamaj et al. (eds) Plant endocytosis. Springer-Verlag, Berlin, Heidelberg, pp 83 – 101

**Holstein SHE, Ungewickell H, Ungewickell E** (1996) Mechanism of clathrin basket dissociation: separate functions of protein domains of the DnaJ homologue auxilin. J Cell Biol 135: 925 – 937

**Hoson T, Kamisaka S, Masuda Y, Yamashita M, Buchen B** (1997) Evaluation of the three-dimensional clinostat as a simulator of weightlessness. Planta 203: S187 – S197

**Hou G, Kramer VL, Wang Y-S, Chen R, Perbal G, Gilroy S** (2004) The promotion of gravitropism in Arabidopsis roots upon actin disruption is coupled with the extended alkalinization of the columella cytoplasm and a persistent lateral auxin gradient. Plant J 39: 113 – 125

**Hou G, Mohamalawari DR, Blancaflor EB** (2003) Enhanced gravitropism of roots with a disrupted cap actin cytoskeleton. Plant Physiol 113: 1360 – 1373

**Hyde GJ, Davies D, Perasso L, Cole L, Ashford AE** (1999) Microtubules, but not actin microfilaments, regulate vacuole motility and morphology in hyphae of *Pisolithus tinctorius*. Cell Motil Cytoskeleton 42: 114 – 124

**Ichikawa M, Sasaki K, Ichikawa A** (1989) Optimal preparatory procedures of cryofixation for immunocytochemistry. J Electron Microsc Tech 12: 88 – 94

**Jones MA, Grierson CS** (2003) A simple method for obtaining cell-specific cDNA from small numbers of growing root-hair cells *in Arabidopsis thaliana*. J Exp Bot 54: 1373 – 1378

**Juniper BE, Gorves S, Landau-Schachar B, Audus LJ** (1966) Root cap and perception of gravity. Nature 209: 93 – 94

**Karol KG, McCourt RM, Cimino MT, Delwiche CF** (2001) The closest living relatives of land plants. Science 294: 2351 – 2353

**Karrer EE, Lincoln JE, Hogenhout S, Bennett AB, Bostock RM, Martineau B, Lucas WJ, Gilchrist DG, Alexander D** (1995) In situ isolation of mRNA from individual plant cells: Creation of cell-specific cDNA libraries. Proc Natl Acad Sci USA 92: 3814 – 3818

**Kashiyama T, Kimura N, Mimura T, Yamamoto K** (2000) Cloning and characterization of a myosin from characean algae, the fastest motor protein in the world. J Biochem 127: 1065 – 1070

**Kimbrough JM, Salinas-Mondragon R, Boss WF, Brown CS, Winter Sederoff H** (2004) The fast and transient transcriptional network of gravity and mechanical stimulation in the Arabidopsis root apex. Plant Physiol 136: 2790 – 2805

**Kiss JZ** (2000) Mechanisms of the early phases of plant gravitropism. Crit Rev Plant Sci 19: 551 – 573

**Kiss JZ, Staehelin LA** (1993) Structural polarity in the Chara rhizoid: a reevaluation. Am J Bot 80: 273 – 282

**Kiss JZ, Wright JB, Caspar T** (1996) Gravitropism in roots of intermediate-starch mutants of Arabidopsis. Physiol Plant 97: 237 – 244

**Kiss JZ, Giddings TH, Staehelin LA, Sack FD** (1990) Comparison of the ultrastructure of conventionally fixed and high pressure frozen/freeze substituted root tips of Nicotiana and Arabidopsis. Protoplasma 157: 64 – 74

**Kremer JR, Mastronarde DN, McIntosh JR** (1996) Computer visualization of three-dimensional image data using IMOD. J Struct Biol 116: 71 – 76

**Kürner J, Frangakis AS, Baumeister W** (2005) Cryo-electron tomography reveals the cytoskeletal structure of *Spiroplasma melliferum*. Science 307: 436 – 438

**Kuznetsov OA, Hasenstein KH** (1996) Magnetophoretic induction of root curvature. Planta 198: 87 – 94

**Kuznetsov OA, Hasenstein KH** (1997) Magnetophoretic induction of curvature in coleoptiles and hypocotyls. J Exp Bot 48: 1951 – 1957

**Kuznetsov OA, Schwuchow J, Sack FD, Hasenstein KH** (1999) Curvature induced by amyloplast magnetophoresis in protonemata of the moss *Ceratodon purpureus*. Plant Physiol 119: 645 – 650

**Ladinsky MS, Mastronarde DN, McIntosh JR, Howell KE, Staehelin LA** (1999) Golgi structure in three dimensions: functional insights from the normal rat kidney cell. J Cell Biol 144: 1135 – 1149

**Lancelle SA, Hepler PK** (1989) Immunogold labeling of actin on sections of freeze-substituted plant cells. Protoplasma 150: 72 – 74

**Laval V, Koroleva OA, Murphy E, Lu C, Milner JJ, Hooks MA, Tomos AD** (2002) Distribution of actin gene isoforms in the Arabidopsis leaf measured in microsamples from intact individual cells. Planta 215: 287 – 292

**Leitz G, Schnepf E, Greulich KO** (1995) Micromanipulation of statoliths in gravity-sensing Chara rhizoids by optical tweezers. Planta 197: 278 – 288

**Lewis LA, McCourt RM** (2004) Green algae and the origin of land plants. Am J Bot: 91: 1535 – 1556

**Liang P, Pardee AB** (1992) Differential display of eukaryotic messenger RNA by means of the polymerase chain reaction. Science 257: 967 – 971

**Lichtscheidl IK, Lancelle SA, Hepler PK** (1990) Actin-endoplasmic reticulum complexes in Drosera. Their structural relationship with the plasmalemma, nucleus, and organelles in cells prepared by high pressure freezing. Protoplasma 155: 116 – 126

**Lievens S, Goormachtig S, Holsters M** (2001) A critical evaluation of differential display as a tool to identify genes involved in legume nodulation: looking back and looking forward. Nucleic Acids Res 29: 3459 – 3468

**Limbach C** (2002) Regulation des gravitropen Spitzenwachstums: Ultrastruktur-Untersuchungen nach Hochdruck-Einfrierfixierung, monomere GTPasen der Rho-Familie und Aktin-assoziierte Proteine. Diploma thesis, Botanical Institute, University of Bonn, Germany

**Limbach C, Hauslage J, Schäfer C, Braun M** (2005) How to activate a plant gravireceptor. Early mechanisms of gravity sensing studied in characean rhizoids during parabolic flights. Plant Physiol 139: 1030 – 1040

**Lovy-Wheeler A, Wilsen KL, Baskin TI, Hepler PK** (2005) Enhanced fixation reveals the apical cortical fringe of actin filaments as a consistent feature of the pollen tube. Planta 221: 95 – 104

**MacCleery SA, Kiss JZ** (1999) Plastid sedimentation kinetics in roots of wild-type and starch-deficient mutants of Arabidopsis. Plant Physiol 120: 183 – 192

**Malhó R, Castanho Coelho P, Pierson E, Derksen J** (2005) Endocytosis and membrane recycling in pollen tubes. In: J Šamaj et al. (eds) Plant endocytosis. Springer-Verlag, Berlin, Heidelberg, pp 277 – 291

**Mastronarde DN** (1997) Dual-axis tomography: an approach with alignment methods that preserve resolution. J Struct Biol 120: 343 – 352

**Matz MV, Lukyanov SA** (1998) Different strategies of differential display: areas of application. Nucleic Acids Res 26: 5537 – 5543

**McCourt RM, Casanova MT, Karol KG, Feist M** (1999) Monophyly of genera and species of Characeae based on rbcL sequences, with special reference to australian and european *Lychnothamnus barbatus* (Characeae: Charophyceae). Aust J Bot 47: 361 – 369

**Miller DD, Lancelle SA, Hepler PK** (1996) Actin microfilaments do not form a dense meshwork in *Lilium longiflorum* pollen tube tips. Protoplasma 195: 123 – 132

**Monaghan P, Perusinghe N, Müller M** (1998) High-pressure freezing for immunocytochemistry. J Microsc 192: 248 – 258

**Moor H** (1987) Theory and practice of high pressure freezing. In: RA Steinbrecht, K Zierold (eds) Cryotechniques in biological electron microscopy. Springer-Verlag, Berlin

**Morita MT, Tasaka M** (2004) Gravity sensing and signaling. Curr Opin Plant Biol 7: 712 – 718

**Morré DJ** (1987) The Golgi apparatus. Int Rev Cytol 17: 211 – 253

**Murata T, Karahara I, Kozuka T, Giddings TH, Staehelin LA, Mineyuki Y** (2002) Improved method for visualizing coated pits, microfilaments, and microtubules in cryofixed and freeze-substituted plant cells. J Electron Microsc 51: 133 – 136

**Nebenführ A** (2002) Vesicle traffic in the endomembrane system: a tale of COPs, Rabs and SNAREs. Curr Opin Plant Biol 5: 507 – 512

**Němec B** (1900) Ueber die Art der Wahrnehmung des Schwerkraftreizes bei den Pflanzen. Ber Dtsch Bot Ges 18: 241 – 245

**Nicastro D, McIntosh JR, Baumeister W** (2005) 3D structure of eukaryotic flagella in a quiescent state revealed by cryo-electron tomography. Proc Natl Acad Sci USA 102: 15889 – 15894

**Nick P, Godbole R, Wang QY** (1997) Probing rice gravitropism with cytoskeletal drugs and cytoskeletal mutants. Biol Bull 192: 141 – 143

**Nicot N, Hausman JF, Hoffmann L, Evers D** (2005) Housekeeping gene selection for real-time RT-PCR normalization in potato during biotic and abiotic stress. J Exp Bot 56: 2907 – 2914

**Noecker H** (2000) Untersuchungen zur polaren Exozytose von Pektinen und Arabinogalactan-Proteoglycanen (AGPS) bei Chara Rhizoiden. Diploma thesis, Botanical Institute, University of Bonn, Germany

**Orfila C, Oxenbøll Sørensen S, Harholt J, Geshi N, Crombie H, Truong H-N, Reid JSG, Knox JP, Scheller HV** (2005) QUASIMODO1 is expressed in vascular tissue of *Arabidopsis thaliana* inflorescence stems and affects homogalacturonan and xylan biosynthesis. Planta 222: 613 – 622

**Orlovich DA, Ashford AE** (1993) Polyphosphate granules are an artefact of specimen preparation in the ectomycorrhizal fungus *Pisolithus tinctorius*. Protoplasma 173: 91 – 105

**Otegui M, Staehelin LA** (2000) Syncytial-type cell plates: a novel kind of cell plate involved in endosperm cellularization of Arabidopsis. Plant Cell 12: 933 – 947

**Otegui MS, Staehelin LA** (2004) Electron tomographic analysis of post-meiotic cytokinesis during pollen development in *Arabidopsis thaliana*. Planta 218: 501 – 515

**Otegui MS, Capp R, Staehelin LA** (2002) Developing seeds of Arabidopsis store different minerals in two types of vacuoles and in the endoplasmic reticulum. Plant Cell 14: 1311 – 1327

**Otegui MS, Mastronarde DN, Kang BH, Bednarek SY, Staehelin LA** (2001) Three-dimensional analysis of syncytial-type cell plates during endosperm cellularization visualized by high resolution electron tomography. Plant Cell 13: 2033 – 2051

**Ottenschläger I, Wolff P, Wolverton C, Bhalerao RP, Sandberg G, Ishikawa H, Evans M, Palme K** (2003) Gravity-regulated differential auxin transport from columella to lateral root cap cells. Proc Natl Acad Sci USA 100: 2987 – 2991

**Parton RM, Fischer-Parton S, Trewavas AJ, Watahiki MK** (2003) Pollen tubes exhibit regular periodic membrane trafficking events in the absence of apical extension. J Cell Sci 116: 2707 – 2719

**Parton RM, Fischer-Parton S, Watahiki MK, Trewavas AJ** (2001) Dynamics of the apical vesicle accumulation and the rate of growth are related in individual pollen tubes. J Cell Sci 114: 2685 – 2695

**Perbal G, Driss-Ecole D** (2003) Mechanotransduction in gravisensing cells. Trends Plant Sci 8: 498 – 504

**Perbal G, Lefrance A, Jeune B, Driss-Ecole D** (2004) Mechanotransduction in root gravity sensing cells. Physiol Plant 120: 303 – 311

**Rabouille C, Klumperman J** (2005) The maturing role of COPI vesicles in intra-Golgi transport. Nature Rev Mol Cell Biol 6: 812 – 817

**Record RD, Griffing LR** (1988) Convergence of the endocytic and lysosomal pathways in soybean protoplasts. Planta 176: 425 – 432

**Reddy ASN, Day IS** (2001) Analysis of the myosins encoded in the recently completed *Arabidopsis thaliana* genome sequence. Genome Biology 2: research 0024.1 – 0024.17

**Richmond TA, Sommerville CR** (2000) The cellulose synthase-like superfamily. Plant Physiol 124: 495 – 498

**Ritzenthaler C, Nebenführ A, Movafeghi A, Stussi-Garaud C, Behnia L, Pimpl P, Staehelin LA, Robinson DG** (2002) Reevaluation of the effects of brefeldin A on plant cells using tobacco Bright Yellow 2 cells expressing Golgi-targeted green fluorescent protein and COPI antisera. Plant Cell 14: 237 – 261

**Robertson JG, Lyttleton P** (1982) Coated and smooth vesicles in the biogenesis of cell walls, plasma membranes, infection threads and peribacteroid membranes in root hairs and nodules of white clover. J Cell Sci 58: 63 – 78

**Robinson DG** (1996) Clathrin-mediated trafficking. Trends Plant Sci 1: 349 – 355

**Robinson DG, Bäumer M, Hinz G, Hohl I** (1998b) Vesicle transfer of storage proteins to the vacuoles: the role of the Golgi apparatus and multivesicular bodies. J Plant Physiol 152: 659 – 667

**Robinson DG, Hinz G, Holstein SE** (1998a) The molecular characterization of transport vesicles. Plant Mol Biol 38: 49 – 76

**Robinson DG, Rogers JC, Hinz G** (2000) Post-Golgi, prevacuolar compartments. Annu Plant Rev 5: 270 – 298

**Roy S, Eckard KJ, Lancelle S, Hepler PK, Lord EM** (1997) High-pressure freezing improves the ultrastructural preservation of in vivo grown lily pollen tubes. Protoplasma 200: 87 – 98

**Royle SJ, Lagnado L** (2003) Endocytosis at the synaptic terminal. J Physiol 553: 345 – 355

**Rozen S, Skaletsky HJ** (2000) Primer3 on the WWW for general users and for biologist programmers. In: S Krawetz, S Misener (eds) Bioinformatics Methods and Protocols: Methods in Molecular Biology. Humana Press, Totowa, pp 365 – 386

**Sack FD** (1997) Plastids and gravitropic sensing. Planta 203: S63 – S68

**Sack FD, Suyemoto MM, Leopold AC** (1984) Kinetics of amyloplast sedimentation in gravistimulated maize coleoptiles. Planta 161: 459 – 464

**Sack FD, Suyemoto MM, Leopold AC** (1985) Amyloplast sedimentation kinetics in gravistimulated maize roots. Planta 165: 295 – 300

**Sack FD, Suyemoto MM, Leopold AC** (1986) Amyloplast sedimentation and organelle saltation in living corn columella cells. Am J Bot 73: 1692 – 1698

**Saito C, Morita MT, Kato T, Tasaka M** (2005) Amyloplasts and vacuolar membrane dynamics in the living graviperceptive cell of the Arabidopsis inflorescence stem. Plant Cell 17: 548 – 558

**Šamaj J, Baluška F, Menzel D** (eds) (2005) Plant endocytosis. In: Plant Cell Monographs, Vol. 1. Springer-Verlag, Berlin, Heidelberg

**Šamaj J, Baluška F, Voigt B, Schlicht M, Volkmann D, Menzel D** (2004) Endocytosis, actin cytoskeleton and signaling. Plant Physiol 135: 1150 – 1161

**Samuels AL, Giddings TH, Staehelin LA** (1995) Cytokinesis in tobacco BY-2 and root tip cells: a new model of cell plate formation in higher plants. J Cell Biol 130: 1345 – 1357

**Satiat-Jeunemaitre B, Boevink P, Hawes C** (1999) Membrane trafficking in higher plant cells: GFP and antibodies, partners for probing the secretory pathway. Biochimie 81: 597 – 605

**Saxena IM, Brown RM** (1995) Identification of a second cellulose synthase gene (acsAII) in *Acetobacter xylinum*. J Bacteriol 177: 5276 – 5283

**Saxena IM, Brown RM, Fevre M, Geremia RA, Henrissat B** (1995) Multidomain architecture of β-glycosyl transferases: implications for mechanism of action. J Bacteriol 177: 1419 – 1424

**Scheible WR, Pauly M** (2004) Glycosyltransferases and cell wall biosynthesis: novel players and insights. Curr Opin Plant Biol 7: 285 – 295

**Schopfer CA, Hepler PK** (1991) Distribution of membranes and the cytoskeleton during cell plate formation in pollen mother cells of Tradescantia. J Cell Sci 100: 717 – 728

**Schröter K, Läuchli A, Sievers A** (1975) Mikroanalytische Identifikation von Bariumsulfat-Kristallen in den Statolithen der Rhizoide von *Chara fragilis* Desv. Planta 122: 213 – 225

**Seguí-Simarro JM, Staehelin LA** (2005) Cell cycle-dependent changes in Golgi stacks, vacuoles, clathrin-coated vesicles and multivesicular bodies in meristematic cells of *Arabidopsis thaliana*: A quantitative and spatial analysis. Planta DOI 10.1007/s00425-005-0082-2

**Seguí-Simarro JM, Austin JR, White EA, Staehelin LA** (2004) Electron tomographic analysis of somatic cell plate formation in meristematic cells of Arabidopsis preserved by high-pressure freezing. Plant Cell 16: 836 – 856

**Shepherd VA, Orlovich DA, Ashford AE** (1993) A dynamic continuum of pleiomorphic tubules and vacuoles in growing hyphae of a fungus. J Cell Sci 104: 495 – 507

**Sievers A** (1965) Elektronenmikroskopische Untersuchungen zur geotropischen Reaktion: I. Über Besonderheiten im Feinbau der Rhizoide von *Chara foetida*. Zeitschr Pflanzenphysiol 53: 193 – 213

**Sievers A** (1967a) Elektronenmikroskopische Untersuchungen zur geotropischen Reaktion. II. Die polare Organisation des normal wachsenden Rhizoids von *Chara foetida*. Protoplasma 64: 225 – 253

**Sievers A** (1967b) Elektronenmikroskopische Untersuchungen zur geotropischen Reaktion. III. Die transversale Polarisierung der Rhizoidspitze von *Chara foetida* nach 5 bis 10 Minuten Horizontallage. Zeitschr Pflanzenphysiol 57: 462 – 473

**Sievers A, Braun M, Monshausen GB** (2002) Root cap: structure and function. In: Y Waisel et al. (eds) Plant roots - the hidden half, Ed 3. Marcel Dekker, New York, pp 33 – 47

**Sievers A, Buchen B, Hodick D** (1996) Gravity sensing in tip-growing cells. Trends Plant Sci 1: 273 – 279

**Sievers A, Buchen B, Volkmann D, Hejnowicz Z** (1991b) Role of the cytoskeleton in gravity perception. In: CW Lloyd (ed) The cytoskeletal basis for plant growth and form. Academic Press, London, pp 169 – 182

**Sievers A, Heinemann B, Rodriguez-Garcia MI** (1979) Nachweis des subapikalen differentiellen Flankenwachstums im Chara-Rhizoid während der Graviresponse. Zeitschr Pflanzenphysiol 91: 435 – 442

**Sievers A, Kramer-Fischer M, Braun M, Buchen B** (1991a) The polar organization of the growing Chara rhizoid and the transport of statoliths are actin-dependent. Bot Acta 104: 103 – 109

**Sievers A, Kruse S, Kuo-Huang L-L, Wendt M** (1989) Statoliths and microfilaments in plant cells. Planta 179: 275 – 278

**Staehelin LA** (1997) The plant ER: a dynamic organelle composed of a large number of discrete functional domains. Plant J 11: 1151 – 1165

**Staehelin LA, Moore I** (1995) The plant Golgi apparatus: structure, functional organization and trafficking mechanisms. Annu Rev Plant Physiol Plant Mol Biol 46: 261 – 288

**Staehelin LA, Giddings TH, Kiss JZ, Sack FD** (1990) Macromolecular differentiation of Golgi stacks in root tips of Arabidopsis and Nicotiana seedlings as visualized in high pressure frozen and freeze-substituted samples. Protoplasma 157: 75 – 91

**Steer MW** (1988) Plasma membrane turnover in plant cells. J Exp Bot 39: 987 – 996

**Studer D, Michel M, Müller M** (1989) High pressure freezing comes of age. Scanning Microsc Suppl 3: 253 – 269

**Studer D, Hennecke H, Müller M** (1992) High-pressure freezing of soybean nodules leads to an improved preservation of ultrastructure. Planta 188: 155 – 163

**Tanchak MA, Griffing LR, Merse BG, Fowke LC** (1984) Endocytosis of cationized ferritin by coated vesicles of soybean protoplasts. Planta 162: 481 – 486

**Theisen R** (2005) Gravitrope Genexpression in *Helianthus annuus*. PhD thesis, IMBIO, University of Bonn, Germany

**Tse YC, Mo B, Hillmer S, Zhao M, Lo SW, Robinson DG, Jiang L** (2004) Identification of multivesicular bodies as prevacuolar compartments in *Nicotiana tabacum* BY-2 cells. Plant Cell 16: 672 – 693

**Tsugeki R, Fedoroff NV** (1999) Genetic ablation of root cap cells in Arabidopsis. Proc Natl Acad Sci USA 96: 12941 – 12946

**Turmel M, Otis C, Lemieux C** (2003) The mitochondrial genome of *Chara vulgaris*: insights into the mitochondrial DNA architecture of the last common ancestor of green algae and land plants. Plant Cell 15: 1888 – 1903

**Tzen JTC, Cao Y-Z, Laurent P, Ratnayake C, Huang AHC** (1993) Lipids, proteins, and structure of seed oil bodies from diverse species. Plant Physiol 101: 267 – 276

**Ungewickell E, Ungewickell H, Holstein SHE, Lindner R, Prasad K, Barouch W, Martin B, Greene LE, Eisenberg E** (1995) Role of auxilin in uncoating clathrin-coated vesicles. Nature 378: 632 – 635

**Volkmann D, Baluska F, Lichtscheidl I, Driss-Ecole D, Perbal G** (1999) Statoliths motions in gravity-perceiving plant cells: Does actomyosin counteract gravity? FASEB J 13: S143 – S147

**Volkmann D, Buchen B, Hejnowicz Z, Tewinkel M, Sievers A** (1991) Oriented movement of statoliths studied in a reduced gravitational field during parabolic flights of rockets. Planta 185: 153 – 161

**Walther P, Ziegler A** (2002) Freeze substitution of high-pressure frozen samples: the visibility of biological membranes is improved when the substitution medium contains water. J Microsc 208: 3 – 10

**Wang-Cahill F, Kiss JZ** (1995) The statolith compartment in Chara rhizoids contains carbohydrate and protein. Am J Bot 82: 220 – 229

**Weise SE, Kiss JZ** (1999) Gravitropism of inflorescence stems in starch-deficient mutants of Arabidopsis. Int J Plant Sci 160: 521 – 527

**Weise SE, Kuznetsov OA, Hasenstein KH, Kiss JZ** (2000) Curvature in Arabidopsis inflorescence stems is limited to the region of amyloplast displacement. Plant Cell Physiol 41: 702 – 709

**Wilson GH, Grolig F, Kosegarten H** (1998) Differential pH restoration after ammonia-elicited vacuolar alkalisation in rice and maize root hairs as measured by fluorescence ratio. Planta 206: 154 – 161

**Yamamoto K, Kiss JZ** (2002) Disruption of the actin cytoskeleton results in the promotion of gravitropism in inflorescence stems and hypocotyls of Arabidopsis. Plant Physiol 128: 669 – 681

**Yamamoto K, Hamada S, Kashiyama T** (1999) Myosins from plants. Cell Mol Life Sci 56: 227 – 232

**Yamazaki M, Saito K** (2002) Differential display analysis of gene expression in plants. Cell Mol Life Sci 59: 1246 – 1255

**Yoder TL, Zheng H-Q, Todd P, Staehelin LA** (2001) Amyloplast sedimentation dynamics in maize columella cells support a new model for the gravity-sensing apparatus of roots. Plant Physiol 125: 1045 – 1060

**Zheng HQ, Staehelin LA** (2001) Nodal endoplasmic reticulum, a specialized form of endoplasmic reticulum found in gravity-sensing root tip columella cells. Plant Physiol 125: 252 – 265

## 6.2 Web sources

BLAST at the web page of the NCBI. URL: http://www.ncbi.nlm.nih.gov/BLAST

ClustalW at the web page of the European Bioinformatics Institute. URL: http://www.ebi.ac.uk/clustalw/index.html

ExPASy server of the Swiss Institute of Bioinformatics. URL: http://www.expasy.ch/

IMOD home hage. URL: http://bio3d.colorado.edu/imod/

NCBI databases. URL: http://www.ncbi.nlm.nih.gov

Primer3 provided by the Whitehead Institute for Biomedical Research. URL: http://frodo.wi.mit.edu/cgi-bin/primer3/primer3_www.cgi

# 7 APPENDIX

**Table VI** *Primers*

All primers that were used in the present study were purchased from MWG unless otherwise stated. Stock solutions with primer concentrations of 12 µM (random primers), 80 µM (T17mod) or 100 µM (all other primers) were prepared with sterile water or nuclease-free water (for RNA applications) and stored at –20° C. Concentrations for use are indicated for each application under 2.7. Oligonucleotide sequences are listed according to the IUB one letter code.

| Name | Sequence | Modification[a] |
|---|---|---|
| **Oligo dT-anchor primer** | | |
| T17mod | $T_{(17)}V$ | 5' 6-FAM–CGGGCCTCTTCGCTATT |
| **Random primers** | | |
| B04mod[b] | GGACTGGAGT | 5' GCCCGGAGAAGCGAT– |
| B05mod[b] | TGCGCCCTTC | 5' GCCCGGAGAAGCGAT– |
| B07mod[b] | GGTGACGCAG | 5' GCCCGGAGAAGCGAT– |
| B09mod[b] | TGGGGGACTC | |
| B16mod[b] | TTTGCCCGGA | 5' TAGCTCACTCATTAGG– |
| **Sequencing primers** | | |
| M13F | GTAAAACGACGGCCAG | |
| M13R | CAGGAAACAGCTATGAC | |
| **Gene-specific primers** | | |
| B05-273FAMfor | TCTATTGATAGCCGTTTCTTTCGTC | 5' 6-FAM– |
| B05-273rev | TGTGAAAACCAAAACCGTTTCTC | |
| B05-273for02 | TCTCAGCCAAAGGACCTGTCAC | |
| B16-292FAMfor | TTTGCCCGGAATCTGACTATTG | 5' 6-FAM– |
| B16-292rev | TCAAATTTCCAAATCGGAGAGG | |
| cgmyo01for[c] | AGAGCTGAGAACGAGACACTC | |
| cgmyo02for[c] | GACGGAGCCTGTGATTACAAC | |
| cgmyo03for[c] | CTCAACTAGAGCAGGAACGATG | |
| cgmyo01rev[c] | GCTCTCACTCCGAATATGTTGG | |
| **RACE primers** | | |
| RACEmyo_GSP1 | GCTCTCACTCCGAATATGTTG | |
| RACEmyo_GSP2 | GCTGGGCATCTGGATAGGTTGTA | |
| RACEmyo_GSP3 | GCTTGATTCGCTGCACATCTGGATAG | |
| RACEB05-273_GSP1 | ACTGGTAGCTCGAAAACATC | |
| RACEB05-273_GSP2 | AGCGACACAGCAGCAACTGATAC | |
| RACEB05-273_GSP3 | CGCGACGAAAGAAACGGCTATCAA | |
| RACEB16-292_GSP1 | AGCGTCCATCTCCAATC | |
| RACEB16-292_GSP2 | CGATTCCCACCAAAACATACCT | |

| | |
|---|---|
| RACEB16-292_GSP3 | AACCCGAACACCGTCCTGGATAAAC |
| RACEMyo_GSP1# | GGCCTTTGCCTGAGCTAA |
| RACEMyo_GSP2# | TGCCTCACGCTCCTTCGCCAAT |
| RACEMyo_GSP3# | CGCTCCTTCGCCAATAACACCTTCA |
| RACEB16_GSP1# | CCATTCTCTCGTCTTGCTTGA |
| RACEB16_GSP2# | TCACTTGACATCACCCCGACCAAT |
| RACEB16_GSP3# | TTCGTGTGAGGATAACGGGTCAA |
| RACEB16_GSP1* | GCAACATCCTGAAGAAAGAC |
| RACEB16_GSP2* | GGAACGTGTAGGTGACCCAGAT |
| RACEB16_GSP3* | GTAGGTGACCCAGATCGGGATGTTC |
| RACEB16_GSP1X | CATCTTCCCAGCCATAGAC |
| RACEB16_GSP2X | GATTGAACAACCCACCGAGGAAGA |
| RACEB16_GSP3X | CAACCCACCGAGGAAGATAGCGTAA |
| B07_GSP1 | TCCTGTCTTGAACCTCTC |
| B07_GSP2 | CGAGGATCTTCTTCACCTCCTTTC |
| B07_GSP3 | TCACCTCCTTTCTGGTCTCCACCTT |
| B16-275_GSP1 | GTAGACCTCCAAATGACATC |
| B16-275_GSP2 | ATGACATCTCCGGGCAAACCTA |
| B16-275_GSP3 | ACATCTCCGGGCAAACCTAATGAGT |
| Myo_GSP1 | GACCTCTTCGTATCCAGAAT |
| Myo_GSP2 | CCGCAGGGACACTTTTGTCTTG |
| Myo_GSP3 | TGACGGCCCTTGAGGTTGCATTTC |
| B16-275X_GSP1 | CCTGTCCATCACCAACTC |
| B16-275X_GSP2 | AGAGTCCACCCAAACCCATGTC |
| B16-275X_GSP3 | CACCCAAACCCATGTCCATTGAGTC |
| B07-481_GSP1 | GGCACTTGGCACATAGTT |
| B07-481_GSP2 | CCACCTCAAAACCTGCAGCACAC |
| B07-481_GSP3_3 | AGCACACGACCCCAGCATTTCAG |

[a] 6-FAM (6-carboxyfluorescein)

[b] Purchased from Carl Roth

[c] Purchased from Operon Biotechnologies (Huntsville, USA)

**Table VII** *Best matches from BLASTX alignment of the nucleotide sequence of B16-292*

Proteins are listed with their corresponding gene bank accession number and the organism from which they were isolated. The level of homology with the translated nucleotide sequence of B16-292 is indicated by the e-value of each alignment.

| Acc. no. | Protein | Species | e-value |
|---|---|---|---|
| NP_194887.1 | glycosyl transferase family 2 protein | *Arabidopsis thaliana* | 4e–122 |
| AAD23884.1 | putative glucosyltransferase | *Arabidopsis thaliana* | 9e–121 |
| BAB01433.1 | glucosyltransferase-like protein | *Arabidopsis thaliana* | 1e–119 |
| CAB88664.1 | putative glucosyltransferase | *Cicer arietinum* | 6e–119 |
| XP_475689.1 | putative glucosyltransferase | *Oryza sativa* | 2e–117 |
| NP_187389.1 | glycosyl transferase family 2 protein | *Arabidopsis thaliana* | 1e–116 |
| BAD34098.1 | CSLC2 | *Oryza sativa* | 1e–116 |
| XP_476455.1 | putative CSLC9 (cellulose synthase-like) | *Oryza sativa* | 7e–116 |
| AAL38526.1 | CSLC9 | *Oryza sativa* | 7e–116 |
| AAT85054.1 | putative glycosyl transferase | *Oryza sativa* | 9e–116 |

**Table VIII** *Best matches from BLASTX alignment of the nucleotide sequence of B05-273*

Proteins are listed with their corresponding gene bank accession number and the organism from which they were isolated. The level of homology with the translated nucleotide sequence of B05-273 is indicated by the e-value of each alignment.

| Acc. no. | Protein | Species | e-value |
|---|---|---|---|
| BAA83469.1 | Csf-1 | *Cucumis sativus* | 2e–43 |
| AAB97098.1 | hydroxyproline rich glycoprotein PsHRGP1 | *Pisum sativum* | 8e–42 |
| XP_466813.1 | putative hydroxyproline-rich glycoprotein | *Oryza sativa* | 2e–41 |
| P55844 | Probable 60S ribosomal protein L14 (Hydroxyproline-rich glycoprotein HRGP1) | *Pisum sativum* | 3e–41 |
| XP_473172.1 | OSJNBb0070J16.13 | *Oryza sativa* | 9e–41 |
| ABA40467.1 | glycoprotein-like protein | *Solanum tuberosum* | 9e–41 |
| BAD22765.1 | glycoprotein | *Bromus inermis* | 1e–40 |
| AAD25645.1 | 60S ribosomal protein L14 | *Arabidopsis thaliana* | 3e–39 |
| CAB79564.1 | ribosomal protein L14-like protein | *Arabidopsis thaliana* | 3e–38 |
| CAC36099.1 | putative ribosomal protein L14 | *Takifugu rubripes* | 1e–30 |

**Table IX** *Best matches from BLASTX alignment of the nucleotide sequence of B07-492*

Proteins are listed with their corresponding gene bank accession number and the organism from which they were isolated. The level of homology with the translated nucleotide sequence of B07-492 is indicated by the e-value of each alignment.

| Acc. no.r | Protein | Species | e-value |
|---|---|---|---|
| AAA86952.1 | ribosomal protein L27 homolog | *Pisum sativum* | 1e–47 |
| CAA48289.1 | ribosomal protein L27 | *Pyrobotrys stellata* | 2e–47 |
| CAA50035.1 | ribosomal protein L27 | *Pisum sativum* | 4e–47 |
| AAA86951.1 | ribosomal protein L27 homolog | *Pisum sativum* | 3e–46 |
| BAA96367.1 | ribosomal protein L27 | *Panax ginseng* | 4e–45 |
| NP_193236.1 | 60S ribosomal protein L27 | *Arabidopsis thaliana* | 1e–44 |
| AAN15737.1 | putative ribosomal protein L27 | *Arabidopsis thaliana* | 3e–44 |
| AAM63601.1 | ribosomal protein L27, putative | *Arabidopsis thaliana* | 4e–44 |
| XP_464969.1 | putative 60S ribosomal protein L27 | *Arabidopsis thaliana* | 2e–41 |
| AAQ54645.1 | 60S ribosomal protein RL27 | *Oikopleura dioica* | 2e–41 |

# Publikationen

**Limbach C**, Hauslage J, Schäfer C, Braun M (2005) How to activate a plant gravireceptor. Early mechanisms of gravity sensing studied in characean rhizoids during parabolic flights. Plant Physiology 139: 1030 – 1040

Braun M, **Limbach C** (2005) Rhizoids and protonemata of characean algae – unicellular model systems for research on polarized growth and plant gravity sensing. Protoplasma (in press)

Braun M, **Limbach C** (2005) Gravisensing in single-celled systems – update on characean rhizoids and protonemata. Advances in Space Research 36: 1156 – 1161

Braun M, **Limbach C** (2005) Actin-based gravity-sensing mechanisms in unicellular plant model systems. Proceedings of the 17th ESA Symposium on European Rocket and Balloon Programmes and Related Research, Sandefjord, Norway, ESA SP-590: 41 – 45

Braun M, Hauslage J, Czogalla A, **Limbach C** (2004) Tip-localized actin polymerization and remodeling, reflected by the localization of ADF, profilin and villin, are fundamental for gravitropic tip growth in characean rhizoids. Planta 219: 379 – 388

Braun M, Hauslage J, **Limbach C** (2003) Actin is an essential component of gravitropic signalling pathways. Proceedings of the 16th ESA Symposium on European Rocket and Balloon Programmes and Related Research, St. Gallen, Switzerland, ESA SP-530: 259 – 262

## Tagungsbeiträge

5. Gravimeeting, 09. – 10. December 2005, Erlangen: Hochauflösende Computertomographie und 3D-Modellierung zellulärer Strukturen in gefrierfixierten Chara-Rhizoiden (Vortrag)

XVII International Botanical Congress, 17. – 23. July 2005, Wien: How to activate a plant gravireceptor (Vortrag)

20th Annual Meeting of the American Society for Gravitational and Space Biology (ASGSB), 09. – 12. November 2004, New York: How to activate a plant gravireceptor – early mechanisms of plant gravity sensing (Poster)

13th Meeting of the Group of European Charophytologists, 11. – 13. Oktober 2003, Iffeldorf: Cytoskeleton-mediated gravitropic tip growth in characean rhizoids and protonemata (Vortrag, Poster)

# Erklärung

Ich versichere hiermit, dass ich die vorliegende Arbeit in allen Teilen selbst und ohne jede unerlaubte Hilfe angefertigt habe. Diese oder eine ähnliche Arbeit ist noch keiner anderen Stelle als Dissertation eingereicht worden. Die Arbeit ist an der nachstehend aufgeführten Stelle auszugsweise veröffentlicht worden:

> Limbach C, Hauslage J, Schäfer C, Braun M (2005) How to activate a plant gravireceptor. Early mechanisms of gravity sensing studied in characean rhizoids during parabolic flights. Plant Physiology 139: 1030 – 1040.

Ich habe früher noch keinen Promotionsversuch unternommen.

Bonn, den

# Danksagung

Ich danke Herrn Priv.-Doz Dr. Markus Braun, dass ich über viele Jahre in seiner Arbeitsgruppe mitwirken und dabei interessante und spannende Fragestellungen bearbeiten durfte. Besonders dankbar bin ich dafür, dass er auf meine Fähigkeiten vertraut und mir Verantwortung bei Parabelflugkampagnen und wissenschaftlichen Tagungen übertragen hat. Durch das selbstständige und eigenverantwortliche Arbeiten unter seiner Betreuung habe ich viele wertvolle Erfahrungen gesammelt.

Herrn Prof. Dr. Dieter Volkmann danke ich für die Übernahme des Koreferates und für die Unterstützung während meines Promotionsstudiums, die ich sehr zu schätzen weiß.

Mein herzlicher Dank gilt Herrn Prof. Dr. Andrew L. Staehelin und seinen Mitarbeitern Dr. Monica Schönwaelder, Zachery Gergely, Dr. Byung-Ho Kang, Dr. Jotham Austin II und Dr. Bryon Donohoe (University of Colorado, Boulder, USA), die mich durch die großzügige Bereitstellung der Geräte und durch ihren großen perönlichen Einsatz bei der Durchführung der Hochdruck-Einfrierfixierung und der elektronenmikroskopischen Computertomografie unterstützt haben. Ich habe die Zeit bei ihnen in Boulder sehr genossen. Ich danke Frau Prof. Dr. Heide Schnabl, dass ich die molekularbiologischen Arbeiten in ihrem Labor durchführen konnte und ihren Mitarbeitern Dr. Ralf Theisen und Bettina Kriegs für ihre fachliche Unterstützung. Herrn Prof. Dr. Diedrik Menzel gilt mein Dank für die Bereitstellung der Elektronenmikroskope und des konfokalen Laserscan-Mikroskopes. Ich möchte mich außerdem bei vielen Kollegen bedanken, die durch ihre Hilfsbereitschaft zum Gelingen dieser Arbeit beigetragen haben.

Den Partnern der Parabelflugkampagnen (DLR, ESA, SSC (Swedish Space Corporation), EADS ST, Kayser-Threde, Novespace) danke ich für ihre stets professionelle und angenehme Zusammenarbeit.

Für finanzielle Unterstützung danke ich dem Cusanuswerk, dem DLR (BMBF-Projekte 50WB9998 und 50WB0515) und Frau Prof. Dr. Dorothea Bartels.

Herzlich bedanken möchte ich mich bei Britta Piel und Dr. Monica Schönwaelder für kritisches Lesen und bei Markus Schütz (A & E-Plan GmbH, Meckenheim) für das Ausdrucken meiner Arbeit.

Den aktuellen und ehemaligen Kollegen in der Arbeitsgruppe Gravitationsbiologie Prof. Dr. Andreas Sievers, Priv.-Doz Dr. Markus Braun, Dr. Brigitte Buchen, Dr. Gabriele Monshausen, Andreas Kutscheidt, Melanie Hecht, Simone Masberg, Jens Hauslage, Claudia Schäfer und Nicole Greuel gilt mein Dank für die hervorragende Zusammenarbeit, die herzliche Arbeitsatmosphäre und für die unvergesslichen Parabelflugkampagnen in Bordeaux und Kiruna. Ich werde euch vermissen!

Ich möchte mich bei allen meinen Freunden herzlich bedanken, die mir mit Rat und Tat zur Seite gestanden haben und die dafür verantwortlich sind, dass ich auch ein Leben abseits der Biologie genießen kann.

Ganz besonders danke ich meiner Familie und Christiane für ihr Verständnis, ihre Geduld und ihre bedingungslose Unterstützung.